

**The spontaneous and stimulus evoked  
neural dynamics of the superior colliculus  
in anesthetized ferrets**

Dissertation

Zur Erlangung der Würde des Doktors der Naturwissenschaften im  
Fachbereich Humanwissenschaften der Universität Osnabrück

vorgelegt von

Iain Stitt,  
aus Melbourne

Hamburg,  
April, 2014

# Abstract

---

The study of brain dynamics has traditionally focused study on well-established cortico-cortical, thalamo-cortical, and hippocampo-cortical pathways in the brain, neglecting other brain structures. The superior colliculus (SC) is a highly conserved midbrain structure that displays vast intrinsic, local and global patterns of anatomical connectivity, and therefore presents itself as an interesting alternative structure to study the fundamental principles of neural dynamics. Here, we report for the first time the analysis of both stimulus evoked and spontaneously generated SC neural dynamics across three spatial scales: dynamics intrinsic to the SC, local dynamical interaction with the neighboring inferior colliculus (IC), and large-scale dynamical interaction with the cortex. Within the SC, visual evoked neural dynamics was best characterized by the presence of temporally precise gamma oscillations in retinorecipient superficial SC layers following flash and grating stimuli. Local interareal dynamics in the midbrain were defined by the presence of subthreshold visually evoked activity in the IC that was driven by visual inputs from the SC. Finally, spontaneously generated SC activity is strongly governed by the state of cortical networks, with SC activity locked to prominent slow cortical and spindle oscillations. Collectively, this work provides evidence that nature of neural activity in the SC is strongly governed by both bottom-up sensory and top-down cortical inputs.

# Acknowledgements

I would like to thank the following people; without them this work would have been impossible.

Prof. Dr. Andreas K. Engel, for supporting me the last 5 years and allowing me the freedom to pursue my own research goals (with greater or lesser success).

Dr. rer. nat. Gerhard Engler, for making my initial transition to Hamburg so easy, and for supporting me through the first years of my PhD.

Dr. rer. nat. Edgar Galindo-Leon, for his intellectual support and mentorship.

Dr. rer. nat. Florian Pieper, for his profound technical knowledge.

Dorit Bystron, for helping me conduct all of my experiments and providing a constant source of positivity in hard times.

Dr. rer. nat. Constantin von Nicolai and Rudiger Land for giving me the initial push in the right direction.

Dr. rer. nat. Gernot Supp, for his friendship and the many stimulating scientific discussions we had over the years.

Karl-Jonas Hollensteiner, for listening to my crazy ideas.

My cycling and football mates, who have made my time in Hamburg so thoroughly enjoyable.

Allende Cornejo, for her unwavering love and support, and for making my life away from the lab so fulfilling.

The following work was prepared as a compilation of independent research manuscripts. Therefore, *Chapters 2, 3 & 4* each contain individual *Introduction, Materials and Methods, Results, Discussion* and *References* sections.

## Contents

<b>CHAPTER 1: INTRODUCTION.....</b>	<b>1</b>
REFERENCES .....	5
<b>CHAPTER 2: LAMINAR PROFILE OF VISUAL RESPONSES .....</b>	<b>7</b>
ABSTRACT.....	8
INTRODUCTION.....	9
MATERIALS AND METHODS .....	11
<i>Surgical Preparation.....</i>	<i>11</i>
<i>Histology.....</i>	<i>12</i>
<i>Stimuli.....</i>	<i>12</i>
<i>Data acquisition and preprocessing.....</i>	<i>13</i>
<i>Data Analysis.....</i>	<i>14</i>
RESULTS.....	17
<i>Anatomical correlates of flash-evoked visual field responses.....</i>	<i>17</i>
<i>Layer dependent spike responses to flash and grating stimuli.....</i>	<i>19</i>
<i>MUA receptive field properties .....</i>	<i>21</i>
<i>Flash evoked gamma oscillations.....</i>	<i>23</i>
<i>Drifting grating evoked gamma oscillations.....</i>	<i>26</i>
<i>Oscillations across SC layers .....</i>	<i>28</i>
<i>Spike field coherence.....</i>	<i>31</i>
<i>Inter-shank spike cross-correlation.....</i>	<i>33</i>
DISCUSSION .....	37
<i>Visual responses display laminar specificity.....</i>	<i>37</i>
<i>Stimulus-locked gamma oscillatory activity.....</i>	<i>39</i>
<i>Possible sources of oscillatory activity .....</i>	<i>41</i>
<i>Effects of isoflurane anesthesia on evoked SC oscillations .....</i>	<i>45</i>
<i>Functional significance of entrained gamma oscillations.....</i>	<i>46</i>
<b>CHAPTER 3: AUDIOVISUAL INTERACTION IN THE MIDBRAIN.....</b>	<b>53</b>
ABSTRACT.....	54
INTRODUCTION.....	55
MATERIALS AND METHODS .....	57
<i>Surgery .....</i>	<i>57</i>
<i>Electrophysiology .....</i>	<i>57</i>
<i>Sensory Stimulation.....</i>	<i>58</i>
<i>Data Analysis.....</i>	<i>58</i>
RESULTS.....	61
<i>Physiological reconstruction of recording position in the SC and IC.....</i>	<i>61</i>
<i>Flash and click evoked responses in the SC .....</i>	<i>62</i>

## Contents

<i>Flash and click evoked responses in the IC</i> .....	63
<i>Flash stimuli preferentially modulate LFP phase and not power in the IC</i> .....	65
<i>Visually evoked LFP phase modulations are intrinsic to the IC</i> .....	67
<i>The temporal order of flash and click evoked responses in the midbrain</i> .....	69
<i>Visual receptive field similarity predicts strength of functional connectivity between the SC and IC</i> .....	71
DISCUSSION .....	72
<i>Non-auditory activity in the inferior colliculus</i> .....	72
<i>Functional connectivity in the midbrain</i> .....	74
<i>Sensory evoked LFP phase modulation as a mechanism for multisensory interaction</i> .....	75
REFERENCES .....	77
<b>CHAPTER 4: DYNAMICS OF CORTICOTECTAL FUNCTIONAL CONNECTIVITY</b> .....	<b>80</b>
ABSTRACT .....	81
INTRODUCTION .....	82
MATERIALS AND METHODS .....	84
<i>Surgery</i> .....	84
<i>Custom <math>\mu</math>ECoG design</i> .....	84
<i>Electrophysiology</i> .....	85
<i>Data Analysis</i> .....	86
RESULTS .....	88
<i>High frequency fluctuations in extracellular fields are correlated between SC and cortex</i> .....	88
<i>Spiking activity in the SC is timelocked to the occurrence of high frequency activity in the <math>\mu</math>ECoG</i> .....	90
<i>Correlated corticotectal activity rides on top of the cortical slow oscillation</i> .....	92
<i>Ketamine enhances correlated corticotectal activity</i> .....	95
DISCUSSION .....	97
<i>The spatiotemporal dynamics of spontaneous high frequency activity reveal functional corticotectal connectivity</i> .....	97
<i>SC activity couples to cortical slow and spindle oscillations</i> .....	99
REFERENCES .....	102
<b>CHAPTER 5: DISCUSSION</b> .....	<b>105</b>
<i>The analysis of neural dynamics reveals functional properties of SC networks</i> .....	105
<i>Concluding remarks</i> .....	107
<i>Future direction</i> .....	107

# Chapter 1

---

## Introduction

One of the fundamental goals of neuroscience is to study the link between brain structure and function. While over the last 100 years there has been great advances in the understanding of the structure of the brain - from the molecular composition of neurons to large-scale connectivity in whole human brains - the functional correlates of structural brain architecture remain poorly understood. Unlike more classical approaches that typically consider individual neurons or circuits in isolation, the rapidly emerging field of systems neuroscience represents an attempt to study neural function through the dynamical interaction of different brain components. It is generally thought that only through the study of the brains dynamics can we gain a full understanding of the relationship between brain structure and function (Engel et al., 2013). Until now, studies of neural dynamics have focused on three prominent pathways in the brain: cortex-cortex, thalamus-cortex, and hippocampus-cortex communication. While the focus on these pathways is understandable, there has been little study of the dynamics of other brain structures. As I will discuss below, the superior colliculus (SC) of the midbrain presents itself as interesting alternative structure to study brain dynamics at both local and a global scale.

The SC is a highly conserved structure that appears as two bumps forming the dorsal surface of the midbrain (May, 2006). The primary function of the SC is to direct the sensory structures of the head towards the location of novel external stimuli (Gandhi and Katnani, 2011). To perform this function, the SC integrates information from several sensory streams to produce output motor commands. Reflecting this sensorimotor transformational capability, the SC is divided into several anatomically and functionally distinct sensory and motor layers (May, 2006). More generally, the SC is subdivided into superficial layers that are primarily visual sensitive, and deep layers that respond to visual, auditory, somatosensory and vestibular stimulation and additionally provide the source of motor outputs that initiate orienting eye and head movements (Stein and Meredith, 1993). Reflecting such multimodality, the SC displays vast anatomical connectivity with other brain regions, with bottom-up sensory inputs from the retina (Berson, 1988), spinal cord (Edwards et al., 1979), and neighboring midbrain structures converging with top-down inputs from a wide range of cortical areas (Harting et al., 1992; Manger et al., 2010). Aside from such external inputs, the SC displays a large degree of connectivity both within and across different layers (Doubell et al., 2003; Isa and Hall, 2009). Presumably these patterns of intrinsic, local, and global connectivity act in unison to facilitate the sensorimotor function of the SC, however the precise physiological correlates of this connectivity remain unclear.

The visual system is the predominant sensory modality in the SC, with spatial maps from other modalities aligned to retinal coordinates in superficial layers (Stein and Meredith, 1993). Across the various layers of the SC, the responsiveness of SC neurons to visual stimuli is presumably determined through the interplay between bottom-up inputs from the retina, top-down inputs from the cortex, and intrinsic SC network dynamics. Since retinal inputs are more prominent in superficial layers and cortical inputs more prominent in deeper layers, we were interested in how the interaction of bottom-up, top-down, and intrinsic sources of input shape visually evoked activity across all layers of the SC. Therefore, in *Chapter 2* of this

thesis my aim was to uncover the physiological signatures of the laminar organization of visual pathways in the SC. To achieve this, I analyzed the dynamics of visually evoked neural activity recorded simultaneously from all SC layers.

Auditory inputs to the deep SC arise from the external nucleus and nucleus brachium of the neighboring inferior colliculus (IC) (Jiang et al., 1997). In addition to receiving inputs from the IC, both superficial and deep SC layers project back to the IC (Doubell et al., 2000), indicating that these adjacent structures are reciprocally connected in what could be described as an audiovisual sensory loop. While the projection from IC-to-SC could be considered as a bottom-up auditory sensory input, the precise nature of the SC-to-IC projections remains unclear. After stumbling across a very specific form of visually evoked activity in the IC, my interest in this reciprocal audiovisual connectivity in the midbrain exploded. Therefore in *Chapter 3*, I systematically investigate the physiological consequences of this reciprocal connectivity by analyzing the dynamics of both stimulus evoked and spontaneous neural activity that was recorded simultaneously from both the SC and IC.

After investigating both the physiological correlates of intrinsic and local connectivity in the SC in *Chapters 2 & 3*, I turned my attention towards the cortex, which arguably provides the most diverse source of inputs to the SC (Manger et al., 2010). In the absence of sensory input or motor output, the cortex displays complex spatiotemporal patterns of activity (Arieli et al., 1996; Kenet et al., 2003). The dynamics of such activity are thought to reflect the underlying functional architecture of cortical neural networks (Fukushima et al., 2012). Although the SC is highly responsive to bottom-up sensory inputs spanning several modalities, it remains unclear how spontaneously generated SC neural activity is related to the dynamics of SC-projecting cortical networks. Therefore in *Chapter 4*, I investigate the relationship between SC neural activity and the large-scale dynamics of spontaneously generated cortical activity.

The work presented in *Chapters 2, 3 & 4* of this thesis provide varying and complimentary perspectives on the nature of neural dynamics in the SC. In each chapter, I attempt to link SC structure and function through identifying and studying different fundamental mechanisms of dynamical brain interaction. The mechanisms identified here are generally consistent with those described in other brain areas, and reflect the role of the SC as an interface for the interaction of bottom-up sensory, and top-down cortical inputs. By extension, this work suggests that the basic principles of functional neuronal interaction may be universally applied throughout the brain. I therefore speculate that through the study of neural dynamics, we can gain a fuller understanding of the functional correlates of structural brain organization.

## References

- Arieli a, Sterkin a, Grinvald a, Aertsen a (1996) Dynamics of ongoing activity: explanation of the large variability in evoked cortical responses. *Science* 273:1868–1871.
- Berson DM (1988) Convergence of retinal W-cell and corticotectal input to cells of the cat superior colliculus. *J Neurophysiol* 60:1861–1873.
- Doubell TP, Baron J, Skaliora I, King a J (2000) Topographical projection from the superior colliculus to the nucleus of the brachium of the inferior colliculus in the ferret: convergence of visual and auditory information. *Eur J Neurosci* 12:4290–4308.
- Doubell TP, Skaliora I, Baron J, King AJ (2003) Functional connectivity between the superficial and deeper layers of the superior colliculus: an anatomical substrate for sensorimotor integration. *J Neurosci* 23:6596–6607.
- Edwards SB, Ginsburgh CL, Henkel CK, Stein BE (1979) Sources of subcortical projections to the superior colliculus in the cat. *J Comp Neurol* 184:309–329.
- Engel AK, Gerloff C, Hilgetag CC, Nolte G (2013) Intrinsic coupling modes: multiscale interactions in ongoing brain activity. *Neuron* 80:867–886.
- Fukushima M, Saunders RC, Leopold D a, Mishkin M, Averbek BB (2012) Spontaneous high-gamma band activity reflects functional organization of auditory cortex in the awake macaque. *Neuron* 74:899–910.
- Gandhi NJ, Katnani H a (2011) Motor functions of the superior colliculus. *Annu Rev Neurosci* 34:205–231.
- Harting JK, Updyke B V, Van Lieshout DP (1992) Corticotectal projections in the cat: anterograde transport studies of twenty-five cortical areas. *J Comp Neurol* 324:379–414.
- Isa T, Hall WC (2009) Exploring the superior colliculus in vitro. *J Neurophysiol* 102:2581–2593.
- Jiang ZD, Moore DR, King a J (1997) Sources of subcortical projections to the superior colliculus in the ferret. *Brain Res* 755:279–292.
- Kenet T, Bibitchkov D, Tsodyks M, Grinvald A, Arieli A (2003) Spontaneously emerging cortical representations of visual attributes. *Nature* 425:954–956.
- King a J, Schnupp JW, Thompson ID (1998) Signals from the superficial layers of the superior colliculus enable the development of the auditory space map in the deeper layers. *J Neurosci* 18:9394–9408.
- Manger PR, Restrepo CE, Innocenti GM (2010) The superior colliculus of the ferret: cortical afferents and efferent connections to dorsal thalamus. *Brain Res* 1353:74–85.
- May PJ (2006) The mammalian superior colliculus: laminar structure and connections. *Prog Brain Res* 151:321–378.

Populin LC, Yin TCT (2002) Bimodal interactions in the superior colliculus of the behaving cat. *J Neurosci* 22:2826–2834.

Stein BE, Meredith MA (1993) *The merging of the senses*. The MIT Press.

## **Chapter 2**

---

### **The laminar profile of visual response properties in ferret superior colliculus**

## **Abstract**

In the superior colliculus (SC) visual afferent inputs from various sources converge in a highly organized way such that all layers form topographically aligned representations of contralateral external space. Despite this anatomical organization, it remains unclear how the layer specific termination of different visual input pathways is reflected in the nature of visual response properties and their distribution across layers. To uncover the physiological correlates underlying the laminar organization of the SC, we recorded multi-unit and local field potential activity simultaneously from all layers with dual-shank multi-channel linear probes. We found that the location of spatial receptive fields was strongly conserved across all visual responsive layers. There was a tendency for receptive field size to increase with depth in the SC, with superficial receptive fields significantly smaller than deep receptive fields. Additionally, superficial layers responded significantly faster than deeper layers to flash stimulation. In some recordings, flash-evoked responses were characterized by the presence of gamma oscillatory activity (40-60Hz) in multi-unit and field potential signals, which was strongest in retinorecipient layers. While SC neurons tended to respond only weakly to full-field drifting gratings, we observed very similar oscillatory responses to the offset of grating stimuli, suggesting gamma oscillations are produced following light offset. Oscillatory spiking activity was highly correlated between horizontally distributed neurons within these layers, with oscillations temporally locked to the stimulus. Together, visual response properties provide physiological evidence reflecting the laminar-specific termination of visual afferent pathways in the SC, most notably characterized by the oscillatory entrainment of superficial neurons.

## Introduction

The mammalian superior colliculus (SC) is a highly conserved midbrain structure that responds to novel external events and initiates orienting movements (Stein & Meredith, 1993). The SC is organized into several anatomically and functionally defined layers, reflecting its role in sensorimotor transformations. Superficial layers are purely visually-sensitive, whereas intermediate and deeper layers receive multisensory inputs, and contain premotor neurons that initiate orienting movements (May, 2006). Together, all SC layers form topographically aligned visual, auditory, somatosensory and movement field maps of contralateral external space, with the juxtaposition of sensory and motor layers allowing the rapid transformation of sensory signals into orienting motor commands.

The visual system is the predominant sensory modality in the SC, with sensory and motor maps spatially aligned to retinal coordinates (Stein, Wallace, & Stanford, 1999). The sources of afferent pathways innervating superficial and deep layers reflect the functional dichotomy within the SC, with superficial layers being innervated predominantly by retinal and early visual cortical projections, and deeper layers receiving higher visual and motor cortical projections (Zhang & Hoffmann, 1993) Zhang and Hoffmann, 1993; Manger et al., 2010). In addition to extensive horizontal connections within individual layers, superficial neurons form axon collaterals that terminate in deep layers, forming a direct superficial-to-deep connection in the SC (Grantyn et al., 1984; Hall and Lee, 1993; Hall and Lee, 1997; Isa et al., 1998). Visual responses in the SC are therefore a product of the interplay between bottom-up inputs from the retina, top-down inputs from the cortex, and intrinsic network dynamics within the SC. Due to the differential anatomical connectivity between different SC layers, this interplay is presumably shifted from retinally dominant inputs in more superficial layers to cortically dominant inputs in deeper layers. We therefore hypothesize that the physiological characteristics of visual responses in the SC vary in a depth dependent manner, reflecting the laminar organization of bottom-up and top-down visual afferent pathways to the

SC. Since both retinal and cortical sources of visual afferent inputs to SC neurons display synchronous oscillatory activity in response to visual stimulation, we speculate that neural response dynamics varies according to the source of visual afferent inputs.

Therefore the goal of the present study was to uncover the key physiological correlates reflecting the laminar organization of visual afferent pathways to the SC in the anesthetized ferret. To achieve this, multi-unit activity (MUA) and local field potentials (LFP) were recorded simultaneously from all SC layers with dual-shank multi-channel linear probes, allowing for the depth-wise assessment of visual response properties and stimulus driven neuronal correlations. We present here a complete study of basic visual response properties across all SC layers in the anaesthetized ferret. Our findings strongly reflect the laminar organization of the SC and the laminar-specific termination profile of retinal and cortical visual afferent pathways. In addition, the layer specific presence of visually evoked synchronous gamma oscillations in retinorecipient SC layers suggests that oscillatory activity may be driven by bottom-up retinal inputs under anesthesia.

## Materials and Methods

Seven adult female ferrets (*Mustela putorius*) were used in this study. All experiments were carried out at the University Medical Center Hamburg-Eppendorf, and performed according to the European Community guidelines for the care and use of animals in scientific experiments (Council of the European Communities Directive 86/609/EEC, 1986), and according to the guidelines of the German Animal Protection Law.

### *Surgical Preparation*

Animals were initially anaesthetized with an intramuscular injection of a combination of ketamine hydrochloride (Gräub, 15mg/kg), medetomidine hydrochloride (Janssen-Cilag, 0.08mg/kg) and atropine sulfate (0.15mg/kg). A tracheotomy was then performed to control the breathing of the animal artificially (Harvard Inspira ASV pump), and supply the anesthesia (isoflurane 0.5-1% in a mixture of 1:1 nitrous oxide and oxygen) for the duration of the experiment. Expired CO<sub>2</sub> was monitored and kept within the range of 3 - 4% of the end tidal volume. To prevent dehydration, a cannula was inserted into the femoral vein, delivering a continuous infusion of 0.9% NaCl, 0.5% NaHCO<sub>2</sub>. Eye movements were prevented by supplying pancuronium bromide (6µg/kg/h) in the infusion solution. Body temperature was maintained at ~38°C with an electric heating blanket, and heart rate was monitored with an ECG. After tracheotomy, animals were placed in a stereotactic frame, and a craniotomy was performed from 1-6 mm posterior to the interaural axis, and 4 mm lateral from the midline. The dura was removed to expose the underlying cortex. To prevent exsiccation of cortex, a chamber was built around the craniotomy with dental acrylic and the cortical surface covered with either NaCl or silicon oil. Phenylephrine (Boehringer-Ingelheim) was applied to the contralateral eye to dilate the pupil and retract the nictating membrane before covering the eye with a contact lens. Finally, the ipsilateral eye was occluded to ensure monocular stimulation.

### *Histology*

To reconstruct the depth of recording positions in the SC, in some experiments probes were coated with DiI (Invitrogen) before insertion. Following completion of electrophysiological experiments, the ferret was perfused transcardially with 4% paraformaldehyde (PFA). The brain was carefully removed and postfixed in 4% PFA, 30% sugar solution. Coronal sections (50 $\mu$ m thickness) from the entire SC were prepared with a Leica Jung HN 40 microtome. For sections containing DiI, fluorescent images were captured with a Zeiss Axioskop 40 microscope. These slices were then stained in ammonium silver nitrate solution, revealing the density of myelinated axons (Pistorio et al., 2006).

### *Stimuli*

Visual stimuli consisted of full-field flashes and drifting gratings. Flashes were presented with an LED controlled by a Tektronix AFG 3022 function generator with an inter-stimulus interval that ranged from 0.66-1.66 s between experiments. The LED was projected into an optic cable, which was placed 10 cm from the contralateral eye. From this position, light projected through the optic cable illuminated the entire eye. A total of 500 repetitions were presented per block. Since SC neurons respond well to moving stimuli, random direction small drifting gratings (3 $^{\circ}$ ) were used for spatial mapping of receptive fields. Drifting gratings were presented for 300 ms on a 60x60 cm rear projected screen 57 cm in front of the animal. Stimuli appeared randomly at 400 different positions (20x20 stimulation grid) in the ferret's visual field during each stimulus block, which was repeated 10 times for each mapping recording. In addition, full-field drifting gratings were presented for 1 second. To avoid adaptation to certain stimulus features, gratings were presented with various spatial and temporal frequency combinations and 8 equally spaced directions (0 $^{\circ}$ , 45 $^{\circ}$ , ..., 315 $^{\circ}$ ). To maintain constant luminance during presentation, drifting gratings were presented on a gray

background. Drifting grating stimuli were generated using Psychophysics Toolbox (Brainard, 1997).

#### *Data acquisition and preprocessing*

Recordings were performed using a 2x16 dual-shank linear silicon probe with an inter-contact distance of 100  $\mu\text{m}$  and inter-shank distance of 500  $\mu\text{m}$  (Neuronexus, contact size 413  $\mu\text{m}^2$ ). Data were acquired with a digital Lynx system (Neuralynx Tucson, AZ, USA). The probe was lowered into the brain following stereotactic coordinates while the contralateral eye was stimulated with an LED flash. The surface of the SC was identified by the presence of robust spiking in lower probe contacts in response to flash stimulation. To ensure recording from as many SC layers as possible, probes were advanced so that the uppermost visual responses were approximately 400  $\mu\text{m}$  below the most superficial recording contact. When a suitable recording position was obtained, the cortex and chamber were covered with low-temperature melting agar (Merck). Data were sampled online at 32.5 kHz, with the raw signal split and band-pass filtered at 1-500 Hz for LFPs and 600-6000 Hz for MUA, respectively. LFP signals were downsampled to a sample rate of 2.7kHz. All offline data preprocessing data analysis were performed using Matlab (Mathworks). After recordings, the LFP signal was further band-pass filtered between 5 and 150 Hz (transition 3.5-5 and 150-151.5, filter order 1200) both forward and backward to avoid phase shifting. Line noise (50 Hz) and its first harmonic were removed using a notch filter. Finally, the LFP signal was downsampled to 1 kHz. MUA was detected with a positive and negative threshold (Quiroga et al., 2004). To remove artifacts, spikes that were detected on more than 3 contacts simultaneously were discarded (same sample).

*Data Analysis*

*Current source density (CSD).* CSD analysis was used to identify physiological markers inferring the relative depth of recording electrodes within the SC to enable the reliable alignment of recording positions across penetrations and animals. CSD profiles were generated using methods previously described by Nicholson and Freeman (1975). The second spatial derivative across the 16 LFP traces on each shank was calculated, resulting in 14 data series representing the direction of net transmembrane current flow at each contact. CSD profiles were calculated on a trial-by-trial basis, and then averaged over all trials. To improve visualization, CSD profiles were interpolated linearly along the spatial axis. Color plots were generated from CSD profiles in which the x-axis represents time, y-axis depth and color the net transmembrane current flow at each location. Red corresponds to current sinks, or net inward transmembrane currents, and blue corresponds to current sources, net outward transmembrane currents. The inflection depth (ID), or depth representing the transition between current source and current sink, was readily identifiable across all penetrations using CSD analysis. Therefore, ID was used as a marker to realign all recording penetrations to enable a systematic depth-wise analysis of visual response properties across all SC penetrations.

*Visual response timing statistics.* Peristimulus time histograms (PSTH) were generated by counting spikes in 5ms bins over all trials, and calculating the average instantaneous firing rate for each time bin up to 600 ms after stimulation. For response latency measures, PSTHs were corrected for pre-stimulus baseline activity. All bins not exceeding the pre-stimulus mean firing rate plus two standard deviations were discarded, with only significant time bins remaining ( $p < 0.05$ ). At each visual responsive contact, MUA response latency was defined as the first significant time bin after stimulation.

*Receptive field mapping.* To quantify receptive field size and position, we calculated the average spiking response to stimuli presented at each of the 20x20 grid positions. A threshold was defined at 50% of the firing rate of the most responsive grid position to separate

responsive and unresponsive grid sub-fields. Receptive fields were defined as the main cluster of all responsive grid sub-fields. The center of receptive fields was defined as the centroid of the receptive field cluster. Finally, receptive field diameter was defined as the mean of the width and height of the cluster.

*Spectral properties.* To estimate the strength of oscillations in discrete spike data we used the method outlined by Mureşan and coworkers (2008). This method provides a quantitative measure, the oscillation score, which is computed by spectral analysis of autocorrelation histograms (ACH,  $\pm 100$  ms). Briefly, the oscillation score expresses the ratio between the power of the peak oscillating frequency and the average power of the entire spectrum. To determine the strength of synchronous oscillations between horizontally distributed neurons, cross-correlation histograms (CCH) were computed between ID aligned contacts on each shank in the 500 ms following stimulation. To quantify the strength of oscillations temporally locked to the stimulus, shift predictor histograms (SP) were obtained by computing CCHs with trials on one contact shifted by +1. Fast Fourier transforms (FFT) were computed on cross-correlation and shift predictor histograms to determine the proportion of synchronous gamma oscillations caused by shared temporal locking to the stimulus. For LFP spectral analysis, spectral estimates were calculated from preprocessed field potentials on a trial-by-trial basis using the FieldTrip Toolbox for MATLAB (Oostenveld et al., 2011). Spectral estimates were obtained for 20 linearly spaced frequencies between 5 and 100 Hz with a 50 ms sliding window incrementing in 5 ms steps. Trials were rejected from analysis if any data points were outside the range of 10 standard deviations of the entire LFP recording. The time-varying raw power was calculated by taking the absolute value of the square of complex spectra. Spectrograms were expressed as a percentage increase in power relative to the pre-stimulus period (200-25 ms before stimulus onset).

*Spike-phase locking.* To estimate the spike LFP-phase relationship at different frequencies, spike phase-locking values (PLV) were calculated using spikes recorded from the same contact (Lachaux et al., 1999). The instantaneous phase of the LFP at each frequency

was defined as the phase angle between the complex and the real component of the short-time Fourier transform. PLVs were calculated with a sliding window 100 ms in length, and 90 ms overlap (incrementing 10 ms). To avoid potential bias introduced by firing rate modulations, the number of spikes used to calculate PLVs remained constant over time for each recording contact, and was defined by the lowest average firing rate from all 100 ms time windows. PLVs were calculated from randomly drawn spikes in each time window 1000 times to estimate the mean spike PLV for each time point and frequency.

## Results

The depth-dependent visual response properties described here were analyzed based on recordings of MUA and LFP activity from 28 SC penetrations (56 probe shanks) in 7 ferrets using dual-shank multichannel silicon probes. From these penetrations we were able to identify 500 visually responsive MUAs across all depths.

### *Anatomical correlates of flash-evoked visual field responses*

To reconstruct probe position in the SC, we used CSD analysis in parallel with histological reconstruction of recording penetrations. In 3 SC penetrations, we recorded neural activity with fluorescent DiI coated probes, enabling us to reconstruct the probe trajectory and infer the anatomical location of recording contacts. Figure 1A displays an example recording, with DiI fluorescence overlaid onto a myelin stain of the same coronal section. The path of both probe shanks can be seen traversing the various SC layers as fluorescent streaks, with the medial and lateral shanks terminating 1280  $\mu\text{m}$  and 980  $\mu\text{m}$  from the SC surface, respectively. The border between the two largest superficial SC layers, the granular *stratum griseum superficiale* (SGS), and the fiber dense *stratum opticum* (SO), can be seen as a transition from light to dark staining approximately 200  $\mu\text{m}$  below the SC surface. Figure 1B and C display event-related potentials (ERP) and CSD from the medial shank in response to flash stimulation. ERPs at all depths display two components, an early component after approximately 30 ms, and a late component occurring after approximately 70 ms. Progressing from superficial to deep recording contacts, both ERP components transform into largely positive deflecting potentials, the amplitude of which is attenuated in the deepest layers. ERPs across all recording penetrations displayed a similar depth profile, characterized by the emergence of large positive deflecting potentials at a certain depth. CSD analysis was used to visualize depth-related changes in LFP responses to flash stimulation. CSD profiles in all SC

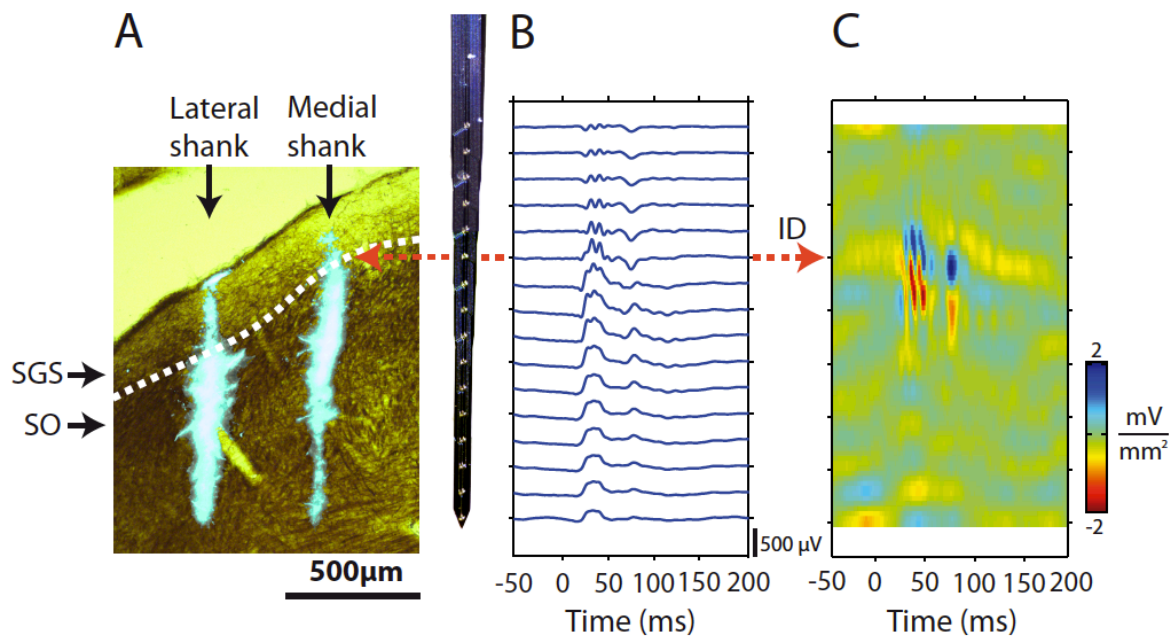


**Figure 1.** Inferring probe position through CSD analysis. In some recordings, probes were coated with DiI before insertion to enable reconstruction of the recording position using fluorescence microscopy. **A**, Example penetration with DiI fluorescence overlaid onto a myelin stain of the same section. The path of both medial and lateral shanks can be seen as two fluorescent tracts terminating at 1280 μm and 980 μm below the SC surface, respectively. A dotted white line represents the border between the two main superficial layers. To the right of the section is a scaled image of a recording probe positioned to the same depth as the lowest fluorescence. **B** and **C**, ERP and CSD profiles of the medial shank in **A**, in response to a 2 ms LED flash presented to the contralateral eye. The inflection depth is visible in the CSD plot as a transition from current source (blue) to current sink (red), and corresponds approximately to the border between the SGS and SO.

penetrations were characterized by the presence of a current source immediately above a current sink. The transition between current source and sink, or inflection depth (ID), represents the location with no net current flow. In this example, the ID corresponds approximately to the border between the SGS and SO. Interestingly, later ERP components display a similar source/sink organization, reflecting the depth of ERP polarity reversal, with the late component ID being located ~100 μm deeper. The anatomically inferred location of the ID in this example was typical for all cases in which DiI was used to reconstruct probe position. Since CSD profiles were very similar across all penetrations, we used the ID as a reference to realign all recording positions post-hoc, allowing us to perform a systematic

analysis of visual response properties across SC layers. Figure 2A depicts the population averaged CSD profile following alignment ( $n = 51$ ), with current source and sink above and below the ID, respectively.

### *Layer dependent spike responses to flash and grating stimuli*

Following alignment of recording penetrations to the ID, we evaluated basic visual response characteristics of SC MUA to flash and drifting grating stimulation. In particular, we focused on average CSD profiles, visual response signal to noise ratio (SNR) and response latency of MUA activity. The average CSD profile following flash stimulation (Figure 2A) was more similar to the average CSD following drifting grating offset (Figure 2G) than drifting grating onset (Figure 2G). Spiking SNR was defined as the relative increase in firing relative to the pre-stimulus period. Figure 2B displays the average spike SNR across SC depth for flash stimuli following alignment of penetrations. Similarly, Figures 2E and H display the average spike SNR depth profile for the onset and offset of drifting grating stimuli respectively. The most superficial visual responsive contacts displayed generally short responses to flash stimuli. Contacts from 100  $\mu\text{m}$  above to 200  $\mu\text{m}$  below the ID, representing the presumed lower SGS and SO layers, produced the largest amplitude spiking responses to flashes and tended to maintain a period of high excitability for several hundred milliseconds following stimulation. Flash-evoked responses in deeper layers were typically noisier, characterized by a lower amplitude onset response, and in some cases were followed by a period of excitability lasting up to 600 ms post-stimulus. Similar to flash-evoked responses, neurons located around the ID displayed the largest amplitude responses to drifting grating stimulus onset and offset. Additionally, neurons in these layers maintained a higher firing rate throughout the sustained period of grating stimulation. Responses in deeper SC layers typically consisted of lower amplitude responses to stimulus onset and offset, with firing rates attenuating to baseline levels throughout the sustained period of stimulation.

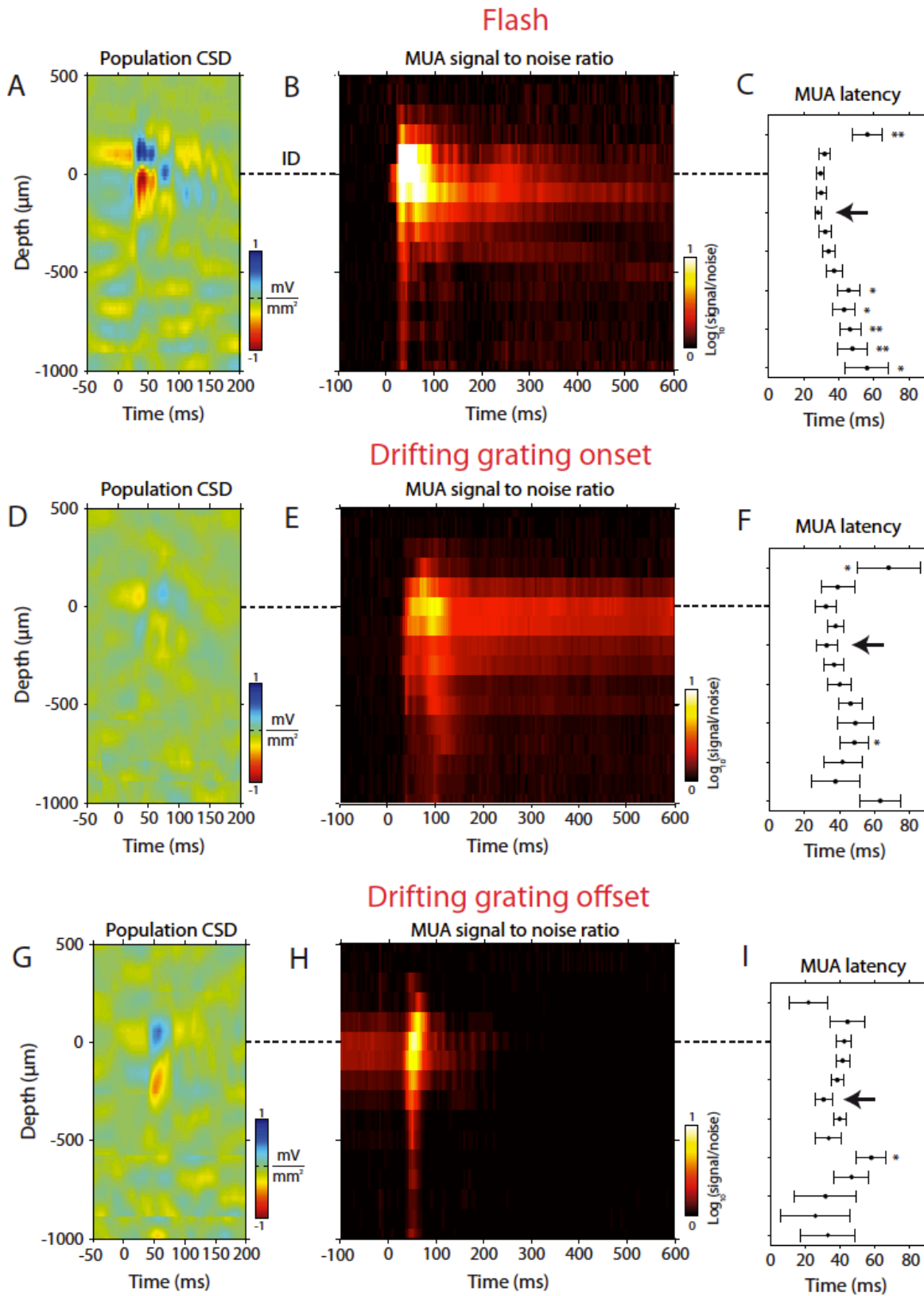


**Figure 2.** Average depth aligned responses to flash and drifting grating stimulation for all penetrations. **A**, Average CSD profile for flash stimulation following alignment of all recordings to the location of the ID (depth 0  $\mu\text{m}$ ). **B**, Distribution of MUA signal/noise ratio across depth. Hot colors indicate a larger increase in firing rate relative to the pre-stimulus period. **C**, Population average visual response latency aligned for depth. **D**, **E**, and **F** display the same information as in plots **A**, **B**, and **C** but for drifting grating stimulus onset. Similarly, **H**, **I** and **J** display CSD, spike SNR and response latency for drifting grating stimulus offset. Error bars indicate standard error. Significance in each plot was measured with respect to the shortest response (arrow),  $p < 0.01$  \*,  $p < 0.001$  \*\*.

Response latencies obtained from flashes and grating stimuli onset exhibited significant depth profiles (ANOVA,  $p < 0.0001$ ), with the earliest responses occurring in the presumed SO region ( $28 \pm 3$  ms flash, and  $33 \pm 6$  ms grating, SEM),  $\sim 200$   $\mu\text{m}$  below the ID. Response latencies for flashes, as well as grating stimuli onset and offset are shown adjacent to spike SNR depth profiles in Figure 2. For flash stimuli, latencies both above and below the fastest responses were significantly longer. Progressing to deeper layers, response latencies became gradually longer such that in the deepest visual responsive layers, latencies were significantly longer ( $56 \pm 12$  ms flash,  $\sim 1000$   $\mu\text{m}$  below ID,  $p < 0.01$ ). Visual responses  $200$   $\mu\text{m}$  above the ID were generally weak or not present, leading to difficulty quantifying response latency for both flash and grating stimuli ( $56 \pm 8.5$  ms  $p < 0.01$  flash,  $68 \pm 18$  ms  $p < 0.05$  grating). The latency of offset responses to grating stimuli did not display a significant depth profile.

#### *MUA receptive field properties*

In 4 experiments, MUA spatial receptive fields (RF) were assessed for all visually-responsive SC layers. Figure 3A depicts spiking RF maps for contacts on both medial and lateral probe shanks for an example recording. On both shanks, neurons respond with higher firing rates to defined stimulus locations in space, visible as hot regions in mapping plots. In this penetration, the most superficial spatial receptive fields occur  $100$   $\mu\text{m}$  above the inflection depth (arrows), which is  $100$   $\mu\text{m}$  deeper on the lateral shank, reflecting the natural mediolateral curvature of the SC layers.

Along each shank, RFs cluster around the same location in the visual field, and tend to progressively increase in size with depth, an observation that was consistent across all mapping recordings. To quantify these observations across all penetrations, we calculated the

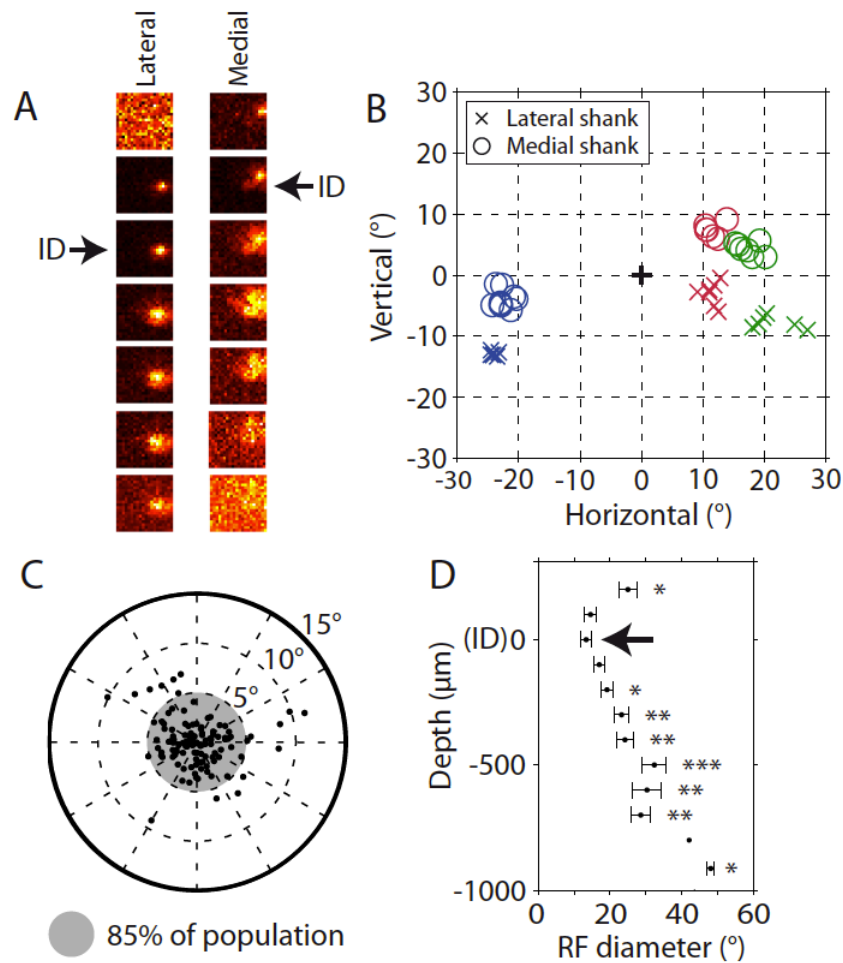


**Figure 3.** Spatial receptive field mapping of SC neurons across depth. **A**, MUA receptive field maps from both shanks of an example recording. In each plot, hot colors indicate regions in the visual field that respond with higher firing rates. Color axes are scaled for the maximum and minimum firing rate at each contact. Arrows indicate the location of the inflection depth for each shank. **B**, Location of receptive field centroids for 3 example penetrations (different colors) with medial centroids plotted as triangles and lateral shanks circles. The cross indicates the center of the visual field. **C**, All RF centroids plotted with the shank-mean centroid as the origin. Blue shaded region represents the 85% limit for all centroids. **D**, Cross-penetration average spatial RF diameter across depth. Error bars indicate standard error. Significance was measured with respect to the smallest RF diameter (arrow),  $p < 0.05$  \*,  $p < 0.01$  \*\*,  $p < 0.001$  \*\*\*.

RF centroid and diameter for all visual responsive units. Figure 3B displays the location of receptive field centroids in the ferret's visual field for 3 representative example recordings (both shanks shown). In each example, RF centroids on each shank cluster around the same

location in space. Two penetrations taken from the left hemisphere (red and green) have RFs in the contralateral right visual field. Similarly, recording from the right hemisphere (blue) have RFs in the left visual field. Within each penetration, centroids between shanks appear at a similar horizontal location, with medial RFs appearing higher in visual space than lateral responses, reflecting the topographic organization of the SC. To visualize the variance of RF centroids across all penetrations, we plotted RF centroids with the shank mean as the origin (Figure 3C). The vast majority (85%) of RF centroids lie within  $5^\circ$  of the shank mean, indicating that spatial RFs maintain topographic alignment across all visual responsive layers.

RF diameters on each shank were aligned to the location of the ID measured from flash stimulation for depth-wise analysis across all penetrations. Receptive fields were significantly different across SC layers ( $p < 0.0001$ , ANOVA). Figure 3D depicts the average spatial receptive field diameter across the depth of the SC. As suggested by the example in Fig. 3A, the smallest receptive fields were located at, and just superior to the ID ( $13 \pm 1.4^\circ$  at  $0 \mu\text{m}$ , and  $14 \pm 1.7^\circ$  at  $+100 \mu\text{m}$ ). Progressing from this point through to deeper layers, RF diameters gradually increased such that at depths  $200 \mu\text{m}$  below the ID RFs are significantly larger ( $300 \mu\text{m}$   $23 \pm 2.1^\circ$   $p < 0.01$ ,  $600 \mu\text{m}$   $30 \pm 4.1^\circ$   $p > 0.01$ ).

### *Flash evoked gamma oscillations*

We observed a large degree of variability in the profile of spiking responses to flash stimulation, both within individual penetrations and across recording sessions. In general, responses could be characterized into two groups: those displaying periodic temporal structure (oscillatory), and those without periodic temporal structure (non-oscillatory). Figure 4 displays raster plots, PSTHs and total power spectrograms from presumed SGS, SO and *stratum griseum intermediale* (SGI) regions in two penetrations that exemplify the types of responses observed. The most superficial visual responses were very similar across all

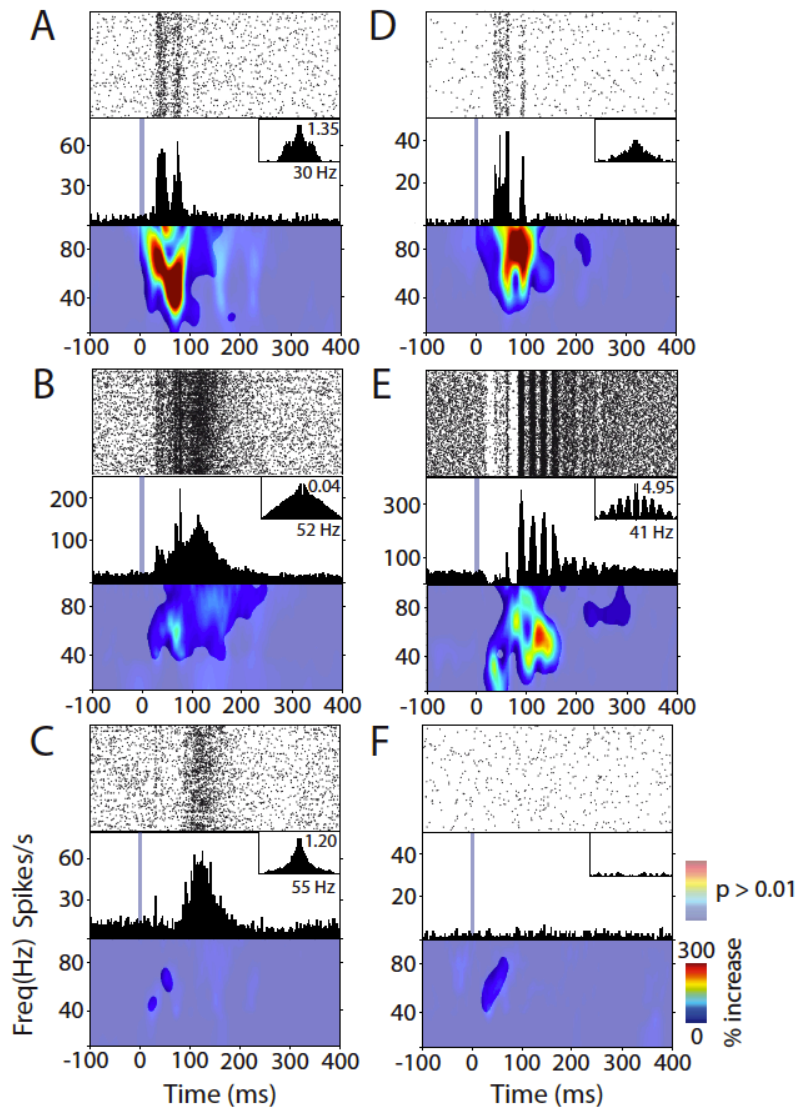


**Figure 4.** Diversity of MUA and LFP responses to flash stimulation. *A*, *B*, and *C*, Raster plots, PSTHs and LFP spectrograms from presumed SGS, SO and SGI regions along a single SC penetration. *D*, *E*, and *F*, Display similar plots to *A*, *B*, and *C*, however data were taken from a recording performed in another animal. Spectrograms are displayed as a percentage increase in total power relative to the pre-stimulus period, with a transparency mask representing time/frequency points that were significantly different from baseline activity ( $p < 0.01$ ). Autocorrelation histograms ( $\pm 100$  ms) taken from spikes occurring 0-500ms after stimulation are plotted as insets in the PSTH. For recording contacts that display a sufficiently high oscillation confidence score ( $> 0.7$ ), oscillation scores and frequency are given. The grey line in the PSTH indicates the presentation of the LED flash stimulus (duration 2 ms).

penetrations and typically consisted of short, high frequency bursts of spiking activity, represented as power increases in high frequency spectral components. In contrast, spiking

responses immediately below the ID tended to be larger in amplitude and longer in duration. The most striking difference between the two penetrations shown in Figure 4 lies in the temporal structure of spiking responses from presumed SO neurons, with Figure 4E displaying strong stimulus-locked oscillatory spiking activity. Flash-evoked oscillatory activity is characterized by the existence of several equally spaced peaks in the PSTH and an increase in gamma power in LFP spectrograms. In contrast, the similarly large magnitude spiking response observed in Figure 4C displays no oscillatory temporal structure, and a comparatively low power increase in high frequency spectral components. Oscillatory responses in most cases initiated after approximately 100ms, following an initial high frequency burst of spiking activity. The presence or absence of flash-evoked oscillatory activity in these layers displayed considerable variability between penetrations, both within the same animal and across animals. Deeper contacts tended to respond much weaker to flash stimuli, with small bursts of activity lasting several hundred milliseconds that rarely displayed evidence of stimulus-locked oscillatory patterning. Although the occurrence of flash-evoked oscillatory responses in the SC was variable across penetrations and animals, oscillatory responses were present in at least one penetration in all animals used in this study (summary in Table 1).

To measure oscillatory responses more quantitatively, we computed the oscillation score (Mureşan et al., 2008) for each visual responsive contact. For the examples in Figure 4, ACHs are plotted as insets in each PSTH. Oscillation scores and peak frequencies are given if the confidence of the oscillations score exceeded 0.7. The example shown in Figure 4E displays a highly structured ACH, with several large amplitude side peaks, with an oscillation score of 4.95 and a spectral peak at 48 Hz. Responses 200  $\mu\text{m}$  above or below this recording display little or no oscillatory response profile, suggesting that flash evoked oscillatory firing is a spatially confined phenomenon. For comparison, the example in Figure 4B, also recorded from the presumed SO region, displays an ACH reflective of bursting activity and an oscillation score of 0.03.

*Drifting grating evoked gamma oscillations*

Full-field flash stimuli represent a spatially homogeneous and highly transient stimulus. Therefore, to probe layer dependent visual response properties for more spatially complex and sustained stimuli, we presented full-field drifting gratings with a variety of spatial and temporal frequency patterns. Figure 5 displays raster plots, PSTHs and total power LFP spectrograms in response to drifting gratings for the same recording sites as displayed in Figure 4. In general, spiking and LFP responses were larger for flash stimuli compared to drifting gratings, with responses to gratings typically consisting of bursts of spiking activity following stimulus onset and offset, and comparably low sustained firing rates throughout the presentation of the stimulus. For each example in Figure 5, ACHs are plotted for sustained and offset responses. Similarly, oscillation scores and peak frequencies are given if the confidence of the oscillations score exceeded 0.7. Perhaps most strikingly, the recording contact that displayed strong stimulus gamma oscillatory activity (Figure 4E) to flash stimulation displays very little onset and sustained responses to drifting gratings. Instead, following stimulus offset, neurons engage in very strong oscillatory activity, represented by several post-stimulus peaks in the PSTH and a large power increase in the gamma frequency range. In this example, the offset response to grating stimulation displayed a striking resemblance to the highly stimulus locked gamma oscillatory response observed after flash stimulation. In general, cases that displayed strong flash-evoked gamma activity also tended to display similar activity to the offset of the drifting grating stimulus.

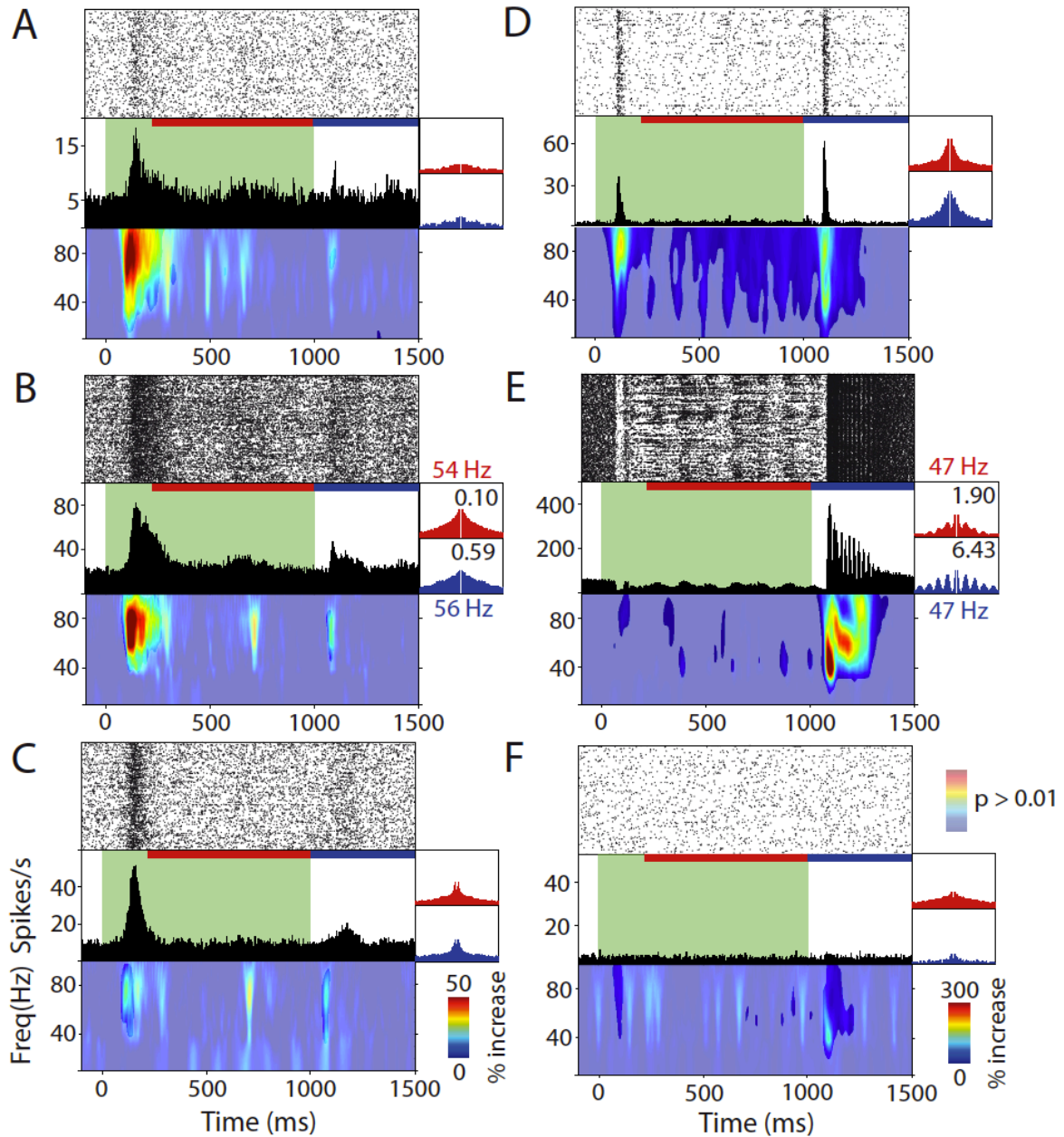


**Figure 5.** MUA and LFP responses to drifting grating stimuli. *A*, *B*, and *C*, Raster plots, PSTHs and LFP spectrograms from the same recording sites displayed in Figure 3 (*A*, *B*, *C*). *D*, *E*, and *F*, display similar plots with data taken from the same penetration as in Figure 3 (*D*, *E*, *F*). Spectrograms are displayed as a percentage increase in total power relative to the pre-stimulus period, with a transparency mask representing time/frequency points that were significantly different from baseline activity ( $p < 0.01$ ). Autocorrelation histograms ( $\pm 100$  ms) taken from spikes occurring 200-1000 ms (red line) are plotted in red, while autocorrelation histograms taken from spikes occurring 1000-1500 (blue line) after stimulation are plotted in blue. For recording contacts that display a sufficiently high oscillation confidence score ( $> 0.7$ ), oscillation scores and frequency are given. The green region in the PSTH indicates the duration of the drifting grating stimulus.

*Oscillations across SC layers*

As suggested by previous examples, we observed the strongest spiking oscillatory activity close to the ID, in the presumed SO region. To confirm this observation quantitatively across all penetrations in all animals, we calculated the percentage of recordings that display certain oscillation scores at each depth for flash (Fig. 6A,  $n = 52$  probe shanks) and grating stimuli (Fig. 6B,C,  $n = 27$  probe shanks). For flash stimuli, the greatest number and largest magnitude of gamma oscillatory responses fell into the region directly at, and below the inflection depth. In this region 16% of recording contacts displayed an oscillation score above 3, with some cases as high as 9. We observed no significant difference in the peak oscillating frequency across the various layers (data not shown, ANOVA,  $p = 0.35$ ). We observed uniformly weak oscillatory responses across all visual responsive layers during the sustained period of grating stimulation, with no responses exceeding an oscillation score of 2. In contrast, oscillation scores calculated from offset responses displayed depth dependence similar to flash-evoked responses, with strong oscillations detected at and below the level of the inflection depth.

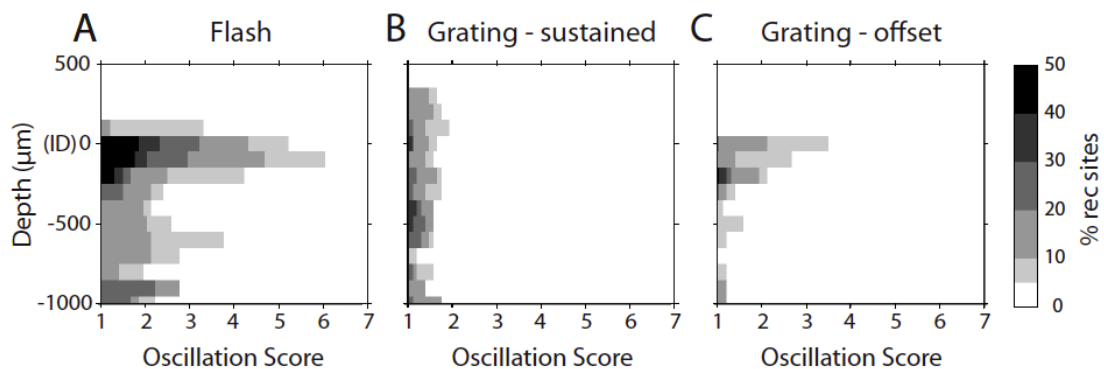


**Figure 6.** MUA oscillation score across SC depth. **A**, Relative occurrence of gamma oscillations score values following flash stimuli for each recording depth in the SC. **B**, Relative occurrence of gamma oscillations score values throughout sustained grating stimuli (200-1000 ms) stimuli across SC depth. **C**, Relative occurrence of gamma oscillations score values following grating stimuli offset (1000-1500 ms) stimuli across SC depth. Values are shown in all plots as percentage of recording sites exhibiting oscillations scores and were calculated following alignment of all penetrations in all animals to the ID. Depth 0 $\mu$ m corresponds to the ID as determined by CSD analysis.

**Table 1.** Incidence of oscillatory penetrations across all animals

Animal #	Number of responsive probe shanks	Number of ‘oscillating’ probe shanks
1	8	4
2	5	3
3	6	1
4	7	2
5	8	3
6	6	4
7	12	6

\* Oscillatory probe shanks were counted if the oscillation score in the gamma frequency range exceeded 2 on any contact.

To determine if flash and drifting grating evoked gamma oscillatory activity observed in spiking activity was reflected in the LFP, we measured the occurrence of post-stimulus time points that displayed significant power increases ( $p < 0.01$ ) relative to the pre-stimulus baseline period. Figure 7 displays a depth-wise representation of the percentage of recording sites across all animals displaying significant power increases for alpha (8-12 Hz), beta (16-24 Hz) and gamma frequencies (30-60 Hz) for each post-stimulus time point. For flash stimuli, a large percentage of recording sites display significant power increases in the first 100ms following stimulation for all tested frequency bands. These responses in the alpha and beta frequencies reflect the time course of evoked potential produced through such a transient visual stimulus. Although all layers display a high occurrence of significant power increases in the gamma frequency in the first 100 ms, the prolonged response (100-200 ms) is characterized by power increases specifically in layers surrounding the ID. Within these layers, 40% of recording sites displayed significant gamma power increases during the later time period. In contrast, less than 10% of deep layer contacts displayed significant power increases. We observed fewer transient responses in the lower frequency bands for the onset

and offset of drifting grating stimuli compared to flash stimuli. As suggested previously by spiking data, we observed a strong occurrence of significant gamma power increases following the offset of grating stimuli that was focused around the ID. Although 36% of recording sites at the ID also displayed a significant gamma power increase in the sustained period of grating stimulation, offset responses were significantly larger than sustained responses in a pairwise comparison (signtest,  $p = 0.013$ ).

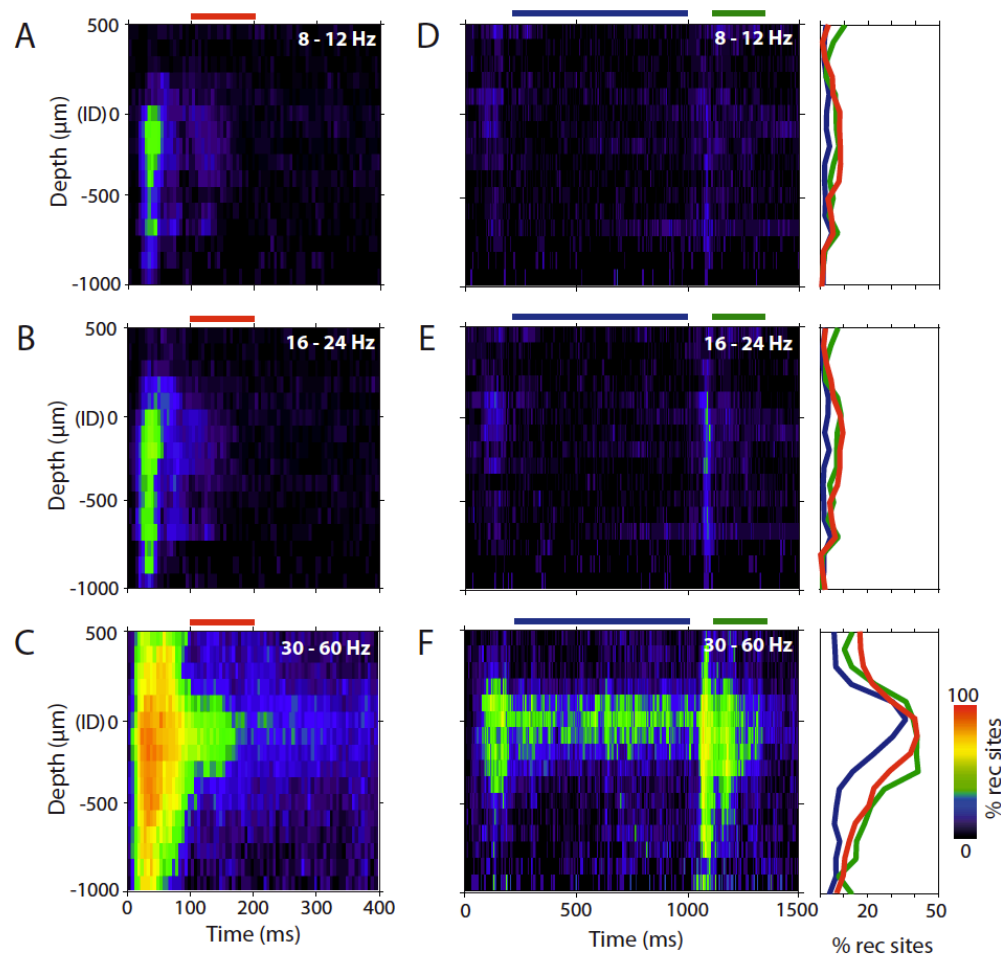


**Figure 7.** LFP oscillations across SC layers. *A*, *B*, and *C* illustrate the percentage of recording sites displaying significant power increases in alpha (*A*), beta (*B*) and gamma (*C*) frequency bands across depth following flash stimulation. Likewise, *D*, *E*, and *F* illustrate the percentage of recording sites displaying significant power increases in alpha (*D*), beta (*E*) and gamma (*F*) frequency bands across depth for drifting grating stimuli. Percentages were calculated across all penetrations from all animals following alignment to the ID. To the right of *D*, *E*, and *F* are plots representing the percentage of recordings displaying significant power increases during each of the indicated time-windows (flash, 100-200 ms – red; sustained grating, 200-1000 ms – blue; grating offset, 1100-1350 ms - green).

*Spike field coherence*

Since the strongest gamma activity in spikes and fields co-localize in the region around the inflection depth, we were interested in the interplay between spikes and fields. To determine the dependence of spike timing on the LFP phase, we calculated the time-resolved phase-locking value (PLV) following flash stimulation. Spike-phase locking was calculated with a 100 ms sliding window for frequency bands up to 100 Hz. Figure 8 displays the PSTHs and PLV spectrograms for example recordings from the presumed SO region for flash and drifting grating stimuli. Similar to previous examples, PSTHs contain several peaks indicating a time-locked oscillatory response to flash and grating stimulation. In the corresponding PLV spectrograms, oscillatory responses are characterized by band-limited increases in spike-phase locking in the gamma frequency range temporally coinciding with oscillatory spiking activity. Therefore in these cases, spike timing is locked to the phase of fields in the gamma frequency. In general, most recordings displaying flash and grating-evoked gamma spiking activity also displayed strong spike-phase locking around the oscillating frequency. Figure 8C and D display the time-resolved average spike PLV in the gamma frequency range for all SC layers for flash and drifting grating stimuli, respectively. In lower superficial and the upper SGI SC layers, flash and grating-offset evoked spiking activity displays strong spike-phase locking at the oscillating frequency of fields, suggesting that neurons are highly entrained to the dynamic fluctuation of local population transmembrane potentials. To determine if oscillating neurons were entrained to local LFP rhythms across all recording contacts, we computed the correlation coefficient between PLVs and oscillation scores. Since we observed the strongest oscillatory responses from 100  $\mu\text{m}$  above, to 300  $\mu\text{m}$  below the ID, we computed correlation coefficients for these layers and all other layers separately (as illustrated in Figure 9A). Correlation coefficients and corresponding p-values are summarized in Table 2. For flash evoked responses, contacts located around the ID displayed a highly significant correlation between oscillation score and PLV ( $R = 0.57$ ,  $p < 0.001$ ), with other contacts displaying no correlation ( $R = -0.07$ ,  $p > 0.5$ ). These layers displayed a similar significant correlation for the

offset to grating stimulation. Interestingly, although other layers did not display strong oscillation scores and PLVs, these values displayed significant correlations for both sustained and offset responses.

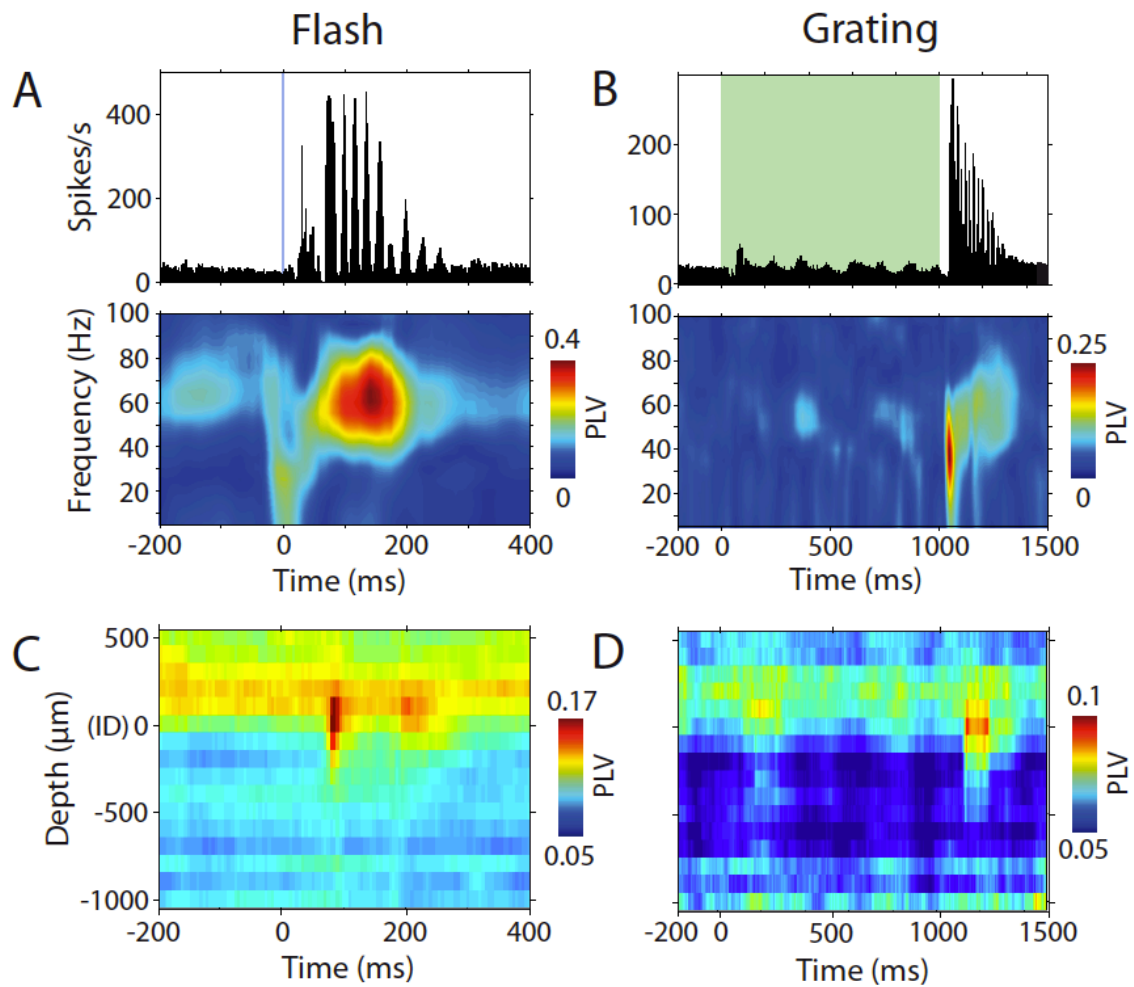


**Figure 8.** Spike-phase locking. **A**, PSTH and PLV spectrogram for an example flash recording. **B**, PSTH and PLV spectrogram for an example drifting grating recording. Plots **C** and **D** display the average spike PLV across all aligned penetrations in the gamma frequency range for each SC depth for flash and grating stimuli, respectively. The grey line and the green box in **A** and **B** indicate the time of flash and drifting grating stimuli, respectively.

**Table 2.** Correlation coefficient and p-values for PLV and oscillation score.

	R	p
Sustained*	0.17	> 0.2
Sustained	0.63	< 0.001
Offset*	0.6	< 0.001
Offset	0.72	< 0.001
Flash*	0.57	< 0.001
Flash	-0.07	> 0.5

\* represents upper SGI, SO and lower SGS layers

#### *Inter-shank spike cross-correlation*

In penetrations displaying gamma oscillatory activity, we often observed oscillations on both shanks at corresponding depths within the SC. To determine how flash and grating evoked gamma oscillations interacted horizontally within SC layers, we investigated the cross-correlation of spiking activity between probe shanks. Cross correlation histograms were computed between contacts at the same relative depth, as determined by the ID on each shank (Fig. 9B). To elucidate the nature of coherent oscillations in more detail, we also computed shift predictor (SP) histograms, or CCHs with the trials on one contact shifted by +1. The resultant SP provides an estimate of spike correlation due to co-modulation of firing rates and shared temporal locking to the stimulus. Figure 9C displays cross correlation and shift predictor histograms computed between two contacts from the presumed SO region separated laterally by 500 $\mu$ m. Following flash stimulation, both of these recording sites displayed an increase in spiking activity characterized by prolonged stimulus-locked oscillations. Accordingly, the CCH calculated during the post-stimulus period displays a highly modulated structure, with a central peak and several side peaks that decay in amplitude for larger time

shifts. Side peaks are separated by between 16-25 ms, indicating an oscillating frequency in the gamma range (40-60 Hz). In this example, the shift predictor shares a very similar structure to the raw CCH, indicating correlated spiking activity remains after shifting trials. To obtain a quantitative measure of the relative strength of gamma oscillations between cross-correlation and shift predictor histograms, we computed the power of each histogram in the gamma frequency. Figure 9D shows the raw CCH gamma power plotted against SP gamma power for all visual responsive contact pairs. Contacts are separated into two groups according to the relative depth in the SC, as illustrated in Figure 9A and 9B. Contacts distributed further from the ID had comparatively low gamma power values for both CCH and SP, with no significant correlation present ( $R = 0.23$ ,  $p > 0.1$ ). In contrast, we observed a very strong correlation for contacts close to the ID ( $R = 0.98$ ,  $p < 0.0001$ ), indicating little discrepancy of gamma power between CCHs computed with shifted trials and aligned trials. Therefore, coherent oscillatory spiking activity observed horizontally within these layers is highly entrained to the flash stimulus, displaying little variability between consecutive trials. We repeated this analysis for the sustained and offset periods of drifting grating stimuli, with correlation coefficients and p-values summarized in Table 3. Similar to flash evoked responses, neurons located close to the ID displayed a highly significant correlation between CCH and SP gamma power following drifting grating stimulus offset ( $R = 0.97$ ,  $p < 0.0001$ ), with other layers displaying no correlation. The gamma power of CCHs computed between horizontally distributed neurons for flash and drifting grating stimuli are shown for all penetrations in Figure 9E. CCH gamma power is shown for both sustained and offset periods of drifting grating stimulation. The strongest gamma oscillations were observed within the presumed SO layers following flash and grating stimulus offset. In contrast, there was no depth dependence of CCH gamma power throughout the sustained period of grating stimulation.

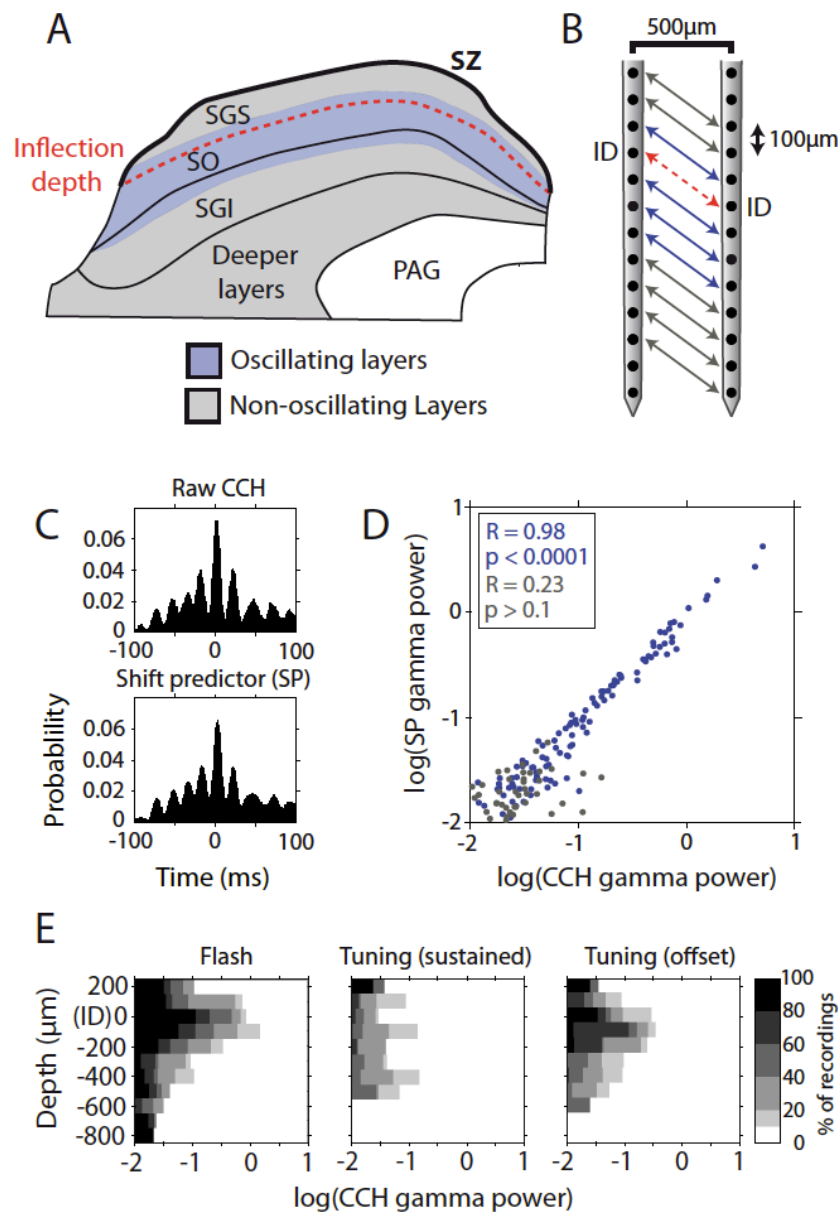


**Figure 9.** Flash-evoked inter-shank spike correlation. **A**, Diagram outlining the occurrence of evoked oscillatory activity across SC layers. The dotted red line indicates the anatomically inferred location of the inflection depth. **B**, Illustration how spike cross-correlation was computed between aligned contacts on both shanks. **C**, Raw CCH and shift predictor histograms calculated from two units displaying flash-evoked oscillatory activity at the same relative depth located on adjacent shanks. **D**, Gamma power of CCHs plotted against the gamma power of shift predictor histograms for flash stimuli. Blue points represent contacts located close to the ID, with all other contacts plotted in gray. Correlation coefficients for each group are given with confidence scores. **E**, Percentage of recording sites at each depth that displayed  $\log(\text{CCH gamma power})$  values between -2 and 1. Abbreviations: SZ, Stratum zonale. SGS, Stratum griseum superficiale. SO, Stratum opticum. SGI, Stratum griseum intermediale. PAG, Periaqueductal gray.

**Table 3.** Correlation coefficient and p-values for CCH and SP gamma power.

	R	p
Sustained*	0.36	< 0.01
Sustained	0.03	> 0.8
Offset*	0.97	< 0.001
Offset	0.30	> 0.1
Flash*	0.98	< 0.001
Flash	0.23	> 0.1

\* represents upper SGI, SO and lower SGS layers

## Discussion

We report here a systematic study of the depth profile of visual response properties recorded simultaneously across the various layers of the ferret SC. Specifically, we investigated depth-activation profiles, response timing, spatial receptive field properties and oscillatory activity by analyzing MUA and LFP responses to flash and drifting grating stimuli. In general, LFP and MUA responses displayed consistent depth profiles across all penetrations, most notably characterized by CSD depth profiles. In the SO and lower SGS regions, responses occurred with short latencies, with deeper layers responding with significantly longer latencies. The strongest visual responses were observed in superficial SC layers. Spatial receptive fields maintained topographic alignment across all visual responsive layers, with RFs centering on the same spatial location along each dorsoventral penetration. We observed the smallest MUA RFs in superficial layers, with deep layers displaying significantly larger RFs. In addition, some recording penetrations were characterized by strong stimulus locked gamma oscillatory activity in spikes and fields that was limited to the lower SGS, SO and upper SGI layers. Stimulus-locked oscillations were evoked by flash stimulation and drifting grating stimulus offset and displayed strong spike-phase locking in the gamma frequency range. Gamma oscillations were also widely distributed laterally within layers, with spike correlations displaying strong temporal locking to the flash and grating stimulus offset.

### *Visual responses display laminar specificity*

We found strong depth dependence for all measured visual response properties to flash stimulation. Perhaps most consistently, we observed a characteristic CSD depth profile, with current sources and sinks, or net inward and outward transmembrane currents, reflecting the approximate location of the anatomical border between the two main superficial SC layers, the SGS and SO. A previous report in awake rabbits reported the location of the inflection depth more superficially in the upper SGS (Bereshpolova et al., 2006). However, the relative

size of various SC layers, and the SGS in particular, is known to differ between species (Hilbig et al., 2000).

Reflecting the layer-specific termination of retinal afferents, we observed shortest latency responses in superficial layers, where fast projecting Y-type and slow projecting W-type retinal ganglions cells (RGC) directly innervate the SO and SGS layers, respectively (Freeman and Singer, 1983; Berson, 1988a, 1988b; Berson and Stein, 1995; Waleszczyk et al., 2004). In the cat, superficial collicular layers additionally receive direct inputs from early visuotopically organized cortical areas such as cytoarchitectonic areas 17, 18, 19 and to a lesser extent area 21a (Harting et al., 1992). In contrast to superficial collicular layers, in both cats (Berson, 1988) and ferrets (Zhang and Hoffmann, 1993), there is virtually no direct retinal input to the deep layers. Furthermore, unlike superficial layers, direct cortical inputs to deep collicular layers in both cats (Harting et al., 1992) and ferrets (Manger et al., 2010) originate from the 'higher-order' visuotopically organized cortical areas. Consistent with this, in the cat at least, reversible inactivation of early visual cortical areas results in reduction of the magnitude of responses to visual stimuli and changes in receptive field properties of collicular neurons located in the superficial layers (e.g. Ogasawara et al., 1984; Hashemi-Nezhad et al., 2003). On the other hand, selective reversible inactivation of 'higher-order' visuotopically organized cortical areas hardly affects the responses of collicular cells located in the superficial layers, but the magnitude of responses to visual stimuli and receptive field properties of collicular neurons located in the deep layers are strongly affected (Ogasawara et al., 1984). Although we report here the first systematic depth-profile analysis of visual response latencies in the SC, the range of latencies we observed across layers were consistent with previous work in the rat (Thomas et al., 2004; Dommett et al., 2005), cat (Altman and Malis, 1962; Berman and Cynader, 1975) and macaque monkey (Wurtz and Goldberg, 1972; Bell et al., 2006; Li and Basso, 2008). In addition to short latency responses, we also consistently observed the most robust spiking responses in superficial layers, potentially reflecting a dominance of retinal inputs in the anaesthetized preparation.

Despite SC layers receiving visual afferent inputs from distributed sources, previous tracing studies in the cat have shown that retinal and cortical terminals align along the dorsoventral axis of the SC, such that all layers form overlaid representations of contralateral visual space (Feldon and Kruger, 1970; Berson, 1988a, 1988b). Reflecting this organization of visual inputs, we observed strong alignment of spatial receptive fields along each shank. In addition, the relative shift of spatial receptive fields between probe shanks, with medial shank neurons responding to locations higher in the visual field, reflects the known topographical organization of the ferret SC (Quevedo et al., 1996). Although receptive fields were aligned along each shank, we observed strong depth dependence in RF size such that retinorecipient superficial layers displayed significantly smaller RFs than deeper layers. Previous studies in the cat (Brecht et al., 1999) and macaque monkey (Humphrey, 1968; Cynader and Berman, 1972) have also noted the tendency for receptive field size to increase with depth. However, this study represents the first systematic analysis of receptive field properties resolved with the laminar anatomy of the SC. Potentially accounting for the larger RFs observed in deeper layers is the relatively large radius of dendritic trees in SGI neurons (Isa and Hall, 2009). Indeed, previous *in vitro* studies in rats (Isa et al., 1998; Helms et al., 2004) and tree shrews (Lee et al., 1997) have shown that stimulation of both directly overlying and off-axis superficial layer neurons results in monosynaptic excitatory postsynaptic potentials in deeper SGI neurons. Therefore, the convergence of superficial-to-deep, or cortico-tectal projections on the large dendritic trees of deep layer neurons could account for the larger spatial visual RFs in these layers.

#### *Stimulus-locked gamma oscillatory activity*

We observed strong synchronous gamma oscillatory activity in spikes and field potentials limited to the lower SGS, SO, and upper SGI regions after flash stimulation and the offset of drifting gratings. Quantitative measures of oscillations strength, including oscillation score, phase-locking values, CCH and SP gamma power suggest that oscillations evoked by flash

and grating stimuli offset are produced by similar mechanisms. Synchronous gamma oscillations have previously been observed in widespread brain regions, and have been implicated in active processing of sensory information, attention, and cognitive processes, leading to the suggestion that such oscillations constitute a flexible communication mechanism between distributed neuronal ensembles (Gray et al., 1989; Engel et al., 1991, 2001; Fries, 2009). In the cat SC, Brecht and coworkers (1999, 2001) observed synchronous oscillations between distributed neurons in the alpha (8-12 Hz), beta (12-30 Hz) and gamma (40-60 Hz) frequency ranges, with the probability of synchronization depending on the congruency of visual stimuli and the overlap of receptive fields. Similarly, in the avian homologue to the mammalian SC, the optic tectum, gamma oscillations have also been implicated in coding spatial location of salient multimodal stimuli (Neuenschwander et al., 1996; Sridharan et al., 2011; Goddard et al., 2012). Although it is difficult to generalize across all recording sites in this study, in comparison to previous studies we found relatively weak visual responses for the presentation of drifting grating stimuli. Instead, responses to drifting gratings were typically characterized by strong responses to the transient onset and offset of stimuli, with offset responses in some layers displaying strong gamma oscillatory activity. A potential explanation for the lack of strong visual responses, and subsequent synchronous oscillations during the sustained presentation of drifting gratings may be the use of full-field stimuli in this study. One model for saccade selection in the SC predicts that short-range excitation and long-range inhibition between horizontally distributed neuronal ensembles interact such that one focal point within the SC is activated in a ‘winner-take-all’ scenario, while other regions are suppressed (Van Opstal and Van Gisbergen, 1989). This model predicts that full-field stimuli would activate a large number of long-range horizontal inhibitory pathways, possibly accounting for the weak responses to grating stimuli observed in this study. Indeed, Rizzolatti and coworkers (1974) showed that responses to moving stimuli in the cat SC were significantly reduced when other moving stimuli were simultaneously presented far from the unit discharge area. In an additional study on ferret SC

slices *in vitro*, Meredith and Ramoa (1998) confirmed the existence of horizontally oriented inhibitory effects that were produced by long-range excitatory projections onto local inhibitory interneurons. In accordance with this finding, Lee and Hall (2006) showed in the rat SC that monosynaptic horizontal inhibitory inputs are mostly local, suggesting that long-range inhibitory effects activated during full-field visual stimulation are mediated through multiple synapses. Previous studies describing SC synchrony and oscillations typically utilized more spatially focused stimuli such as drifting bars or natural stimuli, resulting in more focal activation patterns within the SC and a diminished influence of long-range horizontal inhibitory pathways.

Gamma activity described here also display several key characteristics in contrast to previous studies. Most notably, we observed a very strong temporal locking of oscillations to the offset of stimuli. Typically, the timing of spikes produced through the coupling of recurrent neuronal networks are temporally locked to the spiking of other neurons participating in the ensemble (Fries, 2009), and display little temporal locking to the stimulus (Neuenschwander and Singer, 1996; Pauluis et al., 2001). The strength of intra-laminar spike correlations following flash and grating stimuli between simultaneously compared to non-simultaneously recorded trials was almost equal, indicating neuronal synchrony and oscillations are temporally locked to the offset of stimuli. Therefore, synchronous gamma oscillations observed following flash and grating stimulus offset are likely generated by the recruitment of light-offset activated neuronal ensembles that entrain widely distributed SC neurons in a laminar specific fashion.

#### *Possible sources of oscillatory activity*

*Retina.* During periods of oscillatory activity, the timing of spikes in retinorecipient SC layers is locked to the phase of LFP oscillations in the gamma frequency range. Since the LFP partially represents the summation of post-synaptic potentials in the region directly surrounding recorded spiking activity, phase-locking of spiking activity could represent the

entrainment of neurons by massively coherent oscillatory synaptic inputs. Given that evoked gamma oscillatory activity is spatially restricted to retinorecipient layers of the SC, retinal afferents may provide a source of coherent oscillatory inputs that drive oscillations in SC neurons under anesthesia. Indeed, Neuenschwander and coworkers (Neuenschwander and Singer, 1996; Neuenschwander et al., 1999) reported high frequency synchronous gamma oscillations coordinated between groups of RGCs to light onset ( $90 \pm 11$  Hz) and light offset ( $80 \pm 20$  Hz) in the anesthetized cat. In response to stationary flash stimuli, lateral geniculate nucleus (LGN) and cortical neurons reliably followed such retinal oscillations, indicating the feedforward entrainment capacity of retinal and LGN inputs (Castelo-Branco et al., 1998). Other studies in the cat have also shown that RGCs target neurons in the lateral geniculate nucleus (LGN) follow the temporal precision of RGC responses in the retina (Reich et al., 1997; Kara et al., 2000). Superficial SC neurons, like LGN neurons, receive direct RGC afferents, suggesting SC neurons might be similarly entrained by these inputs in the anesthetized preparation. The projection of retinal inputs to the SC in the cat consists of slow conducting W-type fibers and fast conducting Y-type fibers. Y-type inputs are characterized by large axon fibers, allowing the fast propagation of signals and temporal precision of post-synaptic currents, and terminate in the lower SGS, SO and upper SGI. In contrast, slow conducting W-type fibers terminate in the upper SGS and *stratum zonale* (SZ) regions. Fast conducting Y-type fibers therefore represent a likely source of oscillatory retinal inputs to the SC given that they terminate specifically in oscillating layers. Since we observed the strongest oscillations following flash stimuli and the offset of grating stimuli, oscillatory responses may be produced by light-offset sensitive mechanisms in the retina. Within the retina, *in vitro* studies in the frog showed that coherent oscillatory activity was induced by light offset in dimming detector RGCs and was dependent on GABA<sub>A</sub> synaptic transmission (Ishikane et al., 1999; Arai et al., 2004). Therefore, laminar specific synchronous gamma oscillations in the SC may be produced by the feedforward propagation of coordinated Y-type RGC activity

caused by light offset following flash and grating stimulation. However, to test this hypothesis, further studies should record activity simultaneously from the retina.

*Intrinsic SC networks.* Although synchronous gamma oscillations are generally discussed as fundamental mechanism for cortical communication and computation, they have also been observed in several subcortical structures such as the hippocampus (Montgomery and Buzsáki, 2007) and subthalamic nucleus (Trottenberg et al., 2006). Indeed, computational models have shown that neuronal networks consisting of excitatory and inhibitory interneurons produce reliable oscillations in the gamma frequency range when GABA<sub>A</sub> mediated synapses produce shunting effects (Vida et al., 2006; Bartos et al., 2007). Rather than hyperpolarizing the membrane potential, inhibitory shunting synapses lead initially to the intracellular accumulation of chloride ions and attenuation of excitatory post-synaptic potentials (EPSP) for a short period of time. Since the reversal potential of GABA<sub>A</sub> receptor mediated synaptic currents is slightly greater than resting membrane potential for shunting synapses, following the decay of synaptic Cl<sup>-</sup> conductance is a short period of excitability produced by the persistent membrane depolarization. In an *in vitro* study using rat SC slices, Lo and coworkers (1998) showed that inhibitory post-synaptic currents in SO neurons do not markedly hyperpolarize the cell soma and shorten the duration of EPSPs, suggesting these neurons receive inhibitory shunting synapses. Supporting this conclusion some SO neurons also engaged in rhythmic gamma oscillations in response to membrane depolarizations and electrical optic tract stimulation. These data support our finding of synchronous gamma oscillations spatially restricted to lower SGS, SO and upper SGI layers. In the anesthetized rat, Fortin and coworkers (1997) also reported similar depth-dependent oscillatory activity in spikes and fields limited to the SO region. Recent *in vitro* voltage imaging studies in rat SC (Vokoun et al., 2010) and chicken optic tectum (Weigel and Luksch, 2012) slices showed that brief electrical stimulation in superficial retinorecipient layers resulted in sustained activation of neural populations that extended laterally from the stimulation site up to several hundred

micrometers. The prolonged time course of electrically evoked activity described in these studies is similar to time course of flash and grating-offset evoked gamma oscillatory activity in the ferret SC. These studies illustrate that the network mechanisms necessary for generating sustained horizontally distributed neuronal activation are indeed intrinsic to the superior colliculus (or optic tectum). Therefore, electrical stimulation (in slices), flashes and the offset of drifting gratings may represent sufficiently large transient stimuli to trigger reverberations within horizontally distributed recurrent neuronal networks in the SC.

*Cortex.* An alternative source of coherent oscillatory inputs is the visual cortex. Indeed, previous studies have shown flash evoked oscillatory potentials in the visual cortex of anesthetized and awake cats and monkeys (Doty and Kimura, 1963). Thus, corticotectal projections from early visual areas, which terminate in SGS and SO layers of the SC (Harting et al., 1992) may also supply stimulus-locked oscillatory inputs to the SC. The late onset of evoked SC oscillations would certainly allow sufficient time for the formation of corticotectal neuronal assemblies and subsequent entrainment of SC neurons. Some SC oscillatory responses displayed different oscillatory frequencies over the time course of the response (e.g. Fig 5E). It is unclear whether different oscillatory components reflect a decay of the resonant frequency over time or a switch between two sources of inputs with varying oscillatory frequencies. Since RGCs and cortex tend to oscillate at high and low gamma frequencies respectively (Castelo-Branco et al., 1998), the change in oscillating frequency over time may reflect a switch in the dominance of retinal inputs early in the response, to cortical inputs later in the response. To definitively confirm the source of evoked gamma oscillations in SC neurons, further studies should record neural activity simultaneously from the SC, retina and visual cortex.

*Effects of isoflurane anesthesia on evoked SC oscillations*

In some experiments, oscillatory and non-oscillatory responses were recorded in close-by consecutive penetrations in the same animal, suggesting the presence of visually evoked oscillations is non-stationary. Imas and coworkers (2005) showed that the level of isoflurane anesthesia could modulate the strength of flash evoked gamma oscillations in the visual cortex of the rat. In particular, the emergence of late gamma ( $>100$  ms) power was modulated in a concentration dependent manner, with medium isoflurane levels producing strongest oscillatory power. Despite showing a concentration dependent modulation in power, flash-evoked gamma oscillatory activity in the cortex was also present in the waking state, indicating it is not an artifact of isoflurane anesthesia. In the SC, Brecht and colleagues (2001) reported visually-evoked synchronous gamma oscillatory activity between distributed neurons in awake cats, demonstrating that oscillations in the SC are not an artifact of anesthesia. However, while we made an effort to maintain the level of anesthesia constant throughout the experiments, it is conceivable that non-stationarity in depth of anesthesia contributed to the variability with which flash evoked gamma oscillations were observed. In addition, the depth of anesthesia most likely affects the interplay between bottom-up and top-down visual afferent inputs, with retinal afferents presumably being less affected by depth of anesthesia than cortical efferent pathways. The level of anesthesia may also provide an explanation for the tendency for SC neurons to respond strongly to transient changes in stimuli, rather than sustained visual stimulation. For example, neurons in both superficial and deep SC layers in awake cats respond strongly to sustained natural and computer generated visual stimuli (Brecht et al., 2001). Taken together, these results suggest that anesthesia may exert little effects on bottom-up driven evoked oscillations to transient stimuli, whereas induced oscillations, which typically display no temporal locking to the stimulus and may be cortically driven, are dampened in the anesthetized preparation.

*Functional significance of entrained gamma oscillations*

Phase-locked gamma oscillatory responses in the SC were readily evoked by visual stimulus offset, suggesting oscillations may be produced by highly transient changes in the illumination of the retina. Indeed, transient decreases in light may be similarly relevant to animal's behavior as transient increases in light. In a natural setting, such salient stimuli are likely produced by external events that are sufficiently large to trigger orienting or evasive behavior, suggesting visually evoked SC oscillations may play a role in the production of reactive motor behavior. In the frog retina, it has been proposed that the concerted activity of dimming-detector RGCs, or light offset sensitive cells is essential for the initiation of escape behavior. For example, the shadow of an approaching predator may result in a loss of luminance on the animal's retina, triggering an escape response. A previous behavioral and electrophysiological study in frogs by Ishikane and coworkers (2005) showed that synchronous oscillatory activity coordinated between dimming-detector RGCs was highly correlated with escape behavior. Since retinorecipient SC neurons can be reliably entrained by such oscillatory inputs, their downstream targets presumably take advantage of the temporal structure of coherent oscillatory responses in the presumptive generation of escape or orienting behaviors. Coherent oscillations in superficial SC neurons may therefore improve coincidence detection in deep layer premotor neurons (Salinas and Sejnowski, 2000) controlling the rapid generation of motor commands. Alternatively, synchronous oscillatory activity of inhibitory SO neurons may lead to rhythmic inhibition of downstream target neurons, which would result in a rhythmic gain modulation of excitatory inputs to target neurons, with inputs arriving at the correct oscillatory phase being amplified over out of phase inputs (Fries, 2009). Deep layer premotor neurons may utilize either of the two aforementioned mechanisms to initiate motor behavior. Since we recorded neural activity in the anesthetized ferret, circuits controlling motor behavior were silent. Therefore, further studies in wake behaving animals are required to definitively unearth firstly the source of coherent oscillatory activity, and secondly the influence oscillatory activity has on motor

behavior.

## References

- Altman J, Malis Li (1962) An electrophysiological study of the superior colliculus and visual cortex. *Exp. Neurol.* 5: 233–249
- Arai I, Yamada Y, Asaka T, Tachibana M (2004) Light-evoked oscillatory discharges in retinal ganglion cells are generated by rhythmic synaptic inputs. *J. Neurophysiol.* 92: 715–725
- Bartos M, Vida I, Jonas P (2007) Synaptic mechanisms of synchronized gamma oscillations in inhibitory interneuron networks. *Nat. Rev. Neurosci.* 8: 45–56
- Bell AH, Meredith MA, Van Opstal AJ, Munoz DP (2006) Stimulus intensity modifies saccadic reaction time and visual response latency in the superior colliculus. *Exp. Brain Res.* 174: 53–59
- Bereshpolova Y, Stoelzel CR, Gusev AG, Bezdudnaya T, Swadlow HA (2006) The impact of a corticotectal impulse on the awake superior colliculus. *J. Neurosci.* 26: 2250–2259
- Berman N, Cynader M (1975) Receptive fields in cat superior colliculus after visual cortex lesions. *J. Physiol. (Lond.)* 245: 261–270,
- Berson DM, Stein JJ (1995) Retinotopic organization of the superior colliculus in relation to the retinal distribution of afferent ganglion cells. *Vis. Neurosci.* 12: 671–686
- Berson DM (1988a) Retinal and cortical inputs to cat superior colliculus: composition, convergence and laminar specificity. *Prog. Brain Res.* 75: 17–26
- Berson DM (1988b) Convergence of retinal W-cell and corticotectal input to cells of the cat superior colliculus. *J. Neurophysiol.* 60: 1861–1873
- Brainard DH (1997) The Psychophysics Toolbox. *Spat. Vis.* 10: 433–436
- Brecht M, Goebel R, Singer W, Engel AK (2001) Synchronization of visual responses in the superior colliculus of awake cats. *Neuroreport* 12: 43–47
- Brecht M, Singer W, Engel AK (1999) Patterns of synchronization in the superior colliculus of anesthetized cats. *J. Neurosci.* 19: 3567–3579
- Castelo-Branco M, Neuenschwander S, Singer W (1998) Synchronization of visual responses between the cortex, lateral geniculate nucleus, and retina in the anesthetized cat. *J. Neurosci.* 18: 6395–6410
- Cynader M, Berman N (1972) Receptive-field organization of monkey superior colliculus. *J. Neurophysiol.* 35: 187–201
- Dommett E, Coizet V, Blaha CD, Martindale J, Lefebvre V, Walton N, Mayhew JEW, Overton PG, Redgrave P (2005) How visual stimuli activate dopaminergic neurons at short latency. *Science* 307: 1476–1479
- Doty RW, Kimura DS (1963) Oscillatory potentials in the visual system of cats and monkey. *J. Physiol. (Lond.)* 168: 205–218

- Engel AK, Fries P, Singer W (2001) Dynamic predictions: oscillations and synchrony in top-down processing. *Nat. Rev. Neurosci.* 2: 704–716
- Engel AK, König P, Kreiter AK, Singer W (1991) Interhemispheric synchronization of oscillatory neuronal responses in cat visual cortex. *Science* 252: 1177–1179
- Feldon P, Kruger L (1970) Topography of the retinal projection upon the superior colliculus of the cat. *Vision Res.* 10: 135–143
- Fortin S, Itaya SK, Chemtob S, Molotchnikoff S (1997) ON and OFF field potentials in the rat superior colliculus during development. *Vision Res.* 37: 3079–3087
- Freeman B, Singer W (1983) Direct and indirect visual inputs to superficial layers of cat superior colliculus: a current source-density analysis of electrically evoked potentials. *J. Neurophysiol.* 49: 1075–1091
- Fries P (2009) Neuronal gamma-band synchronization as a fundamental process in cortical computation. *Annu. Rev. Neurosci.* 32: 209–224
- Goddard CA, Sridharan D, Huguenard JR, Knudsen EI (2012) Gamma oscillations are generated locally in an attention-related midbrain network. *Neuron* 73: 567–580
- Grantyn R, Ludwig R, Eberhardt W (1984) Neurons of the superficial tectal gray. An intracellular HRP-study on the kitten superior colliculus in vitro. *Exp. Brain Res.* 55: 172–176
- Gray CM, König P, Engel AK, Singer W (1989) Oscillatory responses in cat visual cortex exhibit inter-columnar synchronization which reflects global stimulus properties. *Nature* 338: 334–337
- Hall WC, Lee P (1993) Interlaminar connections of the superior colliculus in the tree shrew. I. The superficial gray layer. *J. Comp. Neurol.* 332: 213–223
- Hall WC, Lee P (1997) Interlaminar connections of the superior colliculus in the tree shrew. III: The optic layer. *Vis. Neurosci.* 14: 647–661
- Harting JK, Updyke BV, Van Lieshout DP (1992) Corticotectal projections in the cat: anterograde transport studies of twenty-five cortical areas. *J. Comp. Neurol.* 324: 379–414
- Hilbig H, Merbach M, Krause J, Gärtner U, Stubbe A (2000) Dendritic organization of neurons of the superior colliculus in animals with different visual capability. *Brain Res. Bull.* 51: 255–265
- Humphrey NK (1968) Responses to visual stimuli of units in the superior colliculus of rats and monkeys. *Exp. Neurol.* 20: 312–340
- Imas OA, Ropella KM, Ward BD, Wood JD, Hudetz AG (2005) Volatile anesthetics enhance flash-induced gamma oscillations in rat visual cortex. *Anesthesiology* 102: 937–947
- Isa T, Endo T, Saito Y (1998) The visuo-motor pathway in the local circuit of the rat superior colliculus. *J. Neurosci.* 18: 8496–8504

- Isa T, Hall WC (2009) Exploring the superior colliculus in vitro. *J. Neurophysiol.* 102: 2581–2593
- Ishikane H, Gangi M, Honda S, Tachibana M (2005) Synchronized retinal oscillations encode essential information for escape behavior in frogs. *Nat. Neurosci.* 8: 1087–1095
- Ishikane H, Kawana A, Tachibana M (1999) Short- and long-range synchronous activities in dimming detectors of the frog retina. *Vis. Neurosci.* 16: 1001–1014
- Kara P, Reinagel P, Reid RC (2000) Low response variability in simultaneously recorded retinal, thalamic, and cortical neurons. *Neuron* 27: 635–646
- Lachaux JP, Rodriguez E, Martinerie J, Varela FJ (1999) Measuring phase synchrony in brain signals. *Hum. Brain Mapp.* 8: 194–208
- Lee P, Hall WC (2006) An in vitro study of horizontal connections in the intermediate layer of the superior colliculus. *J. Neurosci.* 26: 4763–4768
- Li X, Basso MA (2008) Preparing to move increases the sensitivity of superior colliculus neurons. *J. Neurosci.* 28: 4561–4577
- Lo FS, Cork RJ, Mize RR (1998) Physiological properties of neurons in the optic layer of the rat's superior colliculus. *J. Neurophysiol.* 80: 331–343
- Manger PR, Restrepo CE, Innocenti GM (2010) The superior colliculus of the ferret: cortical afferents and efferent connections to dorsal thalamus. *Brain Res.* 1353: 74–85
- May PJ (2006) The mammalian superior colliculus: laminar structure and connections. *Prog. Brain Res.* 151: 321–378
- Meredith MA, Ramoa AS (1998) Intrinsic circuitry of the superior colliculus: pharmacophysiological identification of horizontally oriented inhibitory interneurons. *J. Neurophysiol.* 79: 1597–1602
- Montgomery SM, Buzsáki G (2007) Gamma oscillations dynamically couple hippocampal CA3 and CA1 regions during memory task performance. *Proc. Natl. Acad. Sci. U.S.A.* 104: 14495–14500
- Mureşan RC, Jurjuţ OF, Moca VV, Singer W, Nikolić D (2008) The oscillation score: an efficient method for estimating oscillation strength in neuronal activity. *J. Neurophysiol.* 99: 1333–1353
- Neuenschwander S, Castelo-Branco M, Singer W (1999) Synchronous oscillations in the cat retina. *Vision Res.* 39: 2485–2497
- Neuenschwander S, Engel AK, König P, Singer W, Varela FJ (1996) Synchronization of neuronal responses in the optic tectum of awake pigeons. *Vis. Neurosci.* 13: 575–584
- Neuenschwander S, Singer W (1996) Long-range synchronization of oscillatory light responses in the cat retina and lateral geniculate nucleus. *Nature* 379: 728–732
- Nicholson C, Freeman JA (1975) Theory of current source-density analysis and determination of conductivity tensor for anuran cerebellum. *J. Neurophysiol.* 38: 356–368

- Oostenveld R, Fries P, Maris E, Schoffelen J-M (2011) FieldTrip: Open source software for advanced analysis of MEG, EEG, and invasive electrophysiological data. *Comput. Intell. Neurosci.* 2011: 156869
- Van Opstal AJ, Van Gisbergen JA (1989) A nonlinear model for collicular spatial interactions underlying the metrical properties of electrically elicited saccades. *Biol. Cybern.* 60: 171–183
- Pauluis Q, Baker SN, Olivier E (2001) Precise burst synchrony in the superior colliculus of the awake cat during moving stimulus presentation. *J. Neurosci.* 21: 615–627
- Pistorio AL, Hendry SH, Wang X (2006) A modified technique for high-resolution staining of myelin. *J. Neurosci. Meth.* 153: 135–146
- Quevedo C, Hoffmann KP, Husemann R, Distler C (1996) Overrepresentation of the central visual field in the superior colliculus of the pigmented and albino ferret. *Vis. Neurosci.* 13: 627–638
- Quiroga RQ, Nadasdy Z, Ben-Shaul Y (2004) Unsupervised spike detection and sorting with wavelets and superparamagnetic clustering. *Neural Comput.* 16: 1661–1687
- Reich DS, Victor JD, Knight BW, Ozaki T, Kaplan E (1997) Response variability and timing precision of neuronal spike trains in vivo. *J. Neurophysiol.* 77: 2836–2841
- Rizzolatti G, Camarda R, Grupp LA, Pisa M (1974) Inhibitory effect of remote visual stimuli on visual responses of cat superior colliculus: spatial and temporal factors. *J. Neurophysiol.* 37: 1262–1275
- Salinas E, Sejnowski TJ (2000) Impact of correlated synaptic input on output firing rate and variability in simple neuronal models. *J. Neurosci.* 20: 6193–6209
- Sridharan D, Boahen K, Knudsen EI (2011) Space coding by gamma oscillations in the barn owl optic tectum. *J. Neurophysiol.* 105: 2005–2017
- Stein B, Meredith A (1993) *The merging of the senses.* The MIT Press
- Stein BE, Wallace MT, Stanford TR (1999) Development of multisensory integration: Transforming sensory input into motor output. *Ment. Retard. Dev. Disabil. Res. Rev.* 5: 72–85
- Thomas BB, Seiler MJ, Satta SR, Aramant RB (2004) Superior colliculus responses to light - preserved by transplantation in a slow degeneration rat model. *Exp. Eye Res.* 79: 29–39
- Trottenberg T, Fogelson N, Kühn AA, Kivi A, Kupsch A, Schneider G-H, Brown P (2006) Subthalamic gamma activity in patients with Parkinson's disease. *Exp. Neurol.* 200: 56–65
- Vida I, Bartos M, Jonas P (2006) Shunting inhibition improves robustness of gamma oscillations in hippocampal interneuron networks by homogenizing firing rates. *Neuron* 49: 107–117

- Vokoun CR, Jackson MB, Basso MA (2010) Intralaminar and interlaminar activity within the rodent superior colliculus visualized with voltage imaging. *J. Neurosci.* 30: 10667–10682
- Waleszczyk WJ, Wang C, Benedek G, Burke W, Dreher B (2004) Motion sensitivity in cat's superior colliculus: contribution of different visual processing channels to response properties of collicular neurons. *Acta Neurobiol. Exp. (Wars)* 64: 209–228
- Weigel S, Luksch H (2012) Spatiotemporal analysis of electrically evoked activity in the chicken optic tectum: a VSDI study. *J. Neurophysiol.* 107: 640–648
- Wurtz RH, Goldberg ME (1972) Activity of superior colliculus in behaving monkey. 3. Cells discharging before eye movements. *J. Neurophysiol.* 35: 575–586
- Zhang HY, Hoffmann KP (1993) Retinal projections to the pretectum, accessory optic system and superior colliculus in pigmented and albino ferrets. *Eur. J. Neurosci.* 5: 486–500

## **Chapter 3**

---

**The physiological correlates of early  
multisensory interactions in the ferret midbrain**

## **Abstract**

The inferior colliculus (IC) is situated relatively early in the auditory pathway and sends both ascending projections to the thalamus and descending projections to the auditory brainstem. Although originally thought to be a primary auditory structure, visual and eye position signals have been detected within the IC. Anatomical studies have shown that the IC is reciprocally connected with the neighboring superior colliculus (SC), which is a multisensory structure. Here, we investigate the physiological correlates of such reciprocal connectivity by recording neural signals from the IC and SC simultaneously in the anesthetized ferret. While visual stimuli did not evoke spiking activity in the IC, they reliably produced band-limited modulations in the phase of IC local field potentials (LFP) in two distinct frequency bands: 6-10Hz and 15-30Hz. Visual LFP responses were recorded from the same probe contacts as robust auditory spiking responses. Imaginary coherence analysis confirmed that visual responses in the IC were not volume conducted signals from the neighboring SC. Visual LFP responses in the IC occurred 5.1ms after the retinally driven superficial SC, and 5.3ms before the cortically driven deep SC, suggesting that neither retinal nor cortical inputs drive flash evoked responses in the IC. Auditory responses in the IC preceded deep SC responses by 1.6ms. SC and IC recording sites with similar visual spatial receptive fields displayed stronger spontaneous functional connectivity, suggesting that the SC provides a visuotopic input to the IC. We conclude that reciprocal coupling between the IC and SC serves the dynamic coregistration of retinal centric and head centric visual and auditory space.

## Introduction

External events usually give rise to inputs across a number of sensory modalities, providing the brain with a stream of information that encompasses the collective physical representation of the event. However, the underlying mechanisms by which the brain integrates parallel sensory streams to form a unified representation of the external world remains poorly understood. Recent studies have provided evidence that multiple sensory systems converge and interact not just in higher cortical areas, but also in primary sensory cortical and sub-cortical structures (Stein and Meredith, 1993; Musacchia and Schroeder, 2009; King and Walker, 2012). Indeed, compiling evidence is leading to a model of multisensory integration where virtually all ‘unisensory’ signals are to a certain extent influenced by other sensory modalities, even at the earliest stages of sensory processing. One striking example of such multimodal sensory interaction is the presence of visual and eye-position signals at various stages along the auditory pathway (Bizley et al., 2007; Porter et al., 2007; Bizley and King, 2009). This effect was most prominently studied in the inferior colliculus (IC), an integral node in the ascending auditory pathway located in the midbrain (Bergan and Knudsen, 2009; Bulkin and Groh, 2012; Gruters and Groh, 2012). In contrast to the neighboring superior colliculus, which is inherently a multisensory structure (Stein and Meredith, 1993), the IC is a primary auditory structure that appears to be modulated by other sensory modalities. Therefore, due to its centralized position in the auditory pathway, the IC is an ideal structure to investigate the mechanisms by which a classically unisensory pathway is influenced by other sensory modalities.

Anatomical tracing studies have shown that the IC receives direct visual inputs from the retina (Cooper and Cowey, 1990), the superior colliculus (Adams, 1980; Doubell et al., 2000), and the visual cortex (Cooper and Young, 1976). In addition, the IC provides a dense auditory projection to the deeper layers of the SC (Jiang et al., 1997). Therefore, the visual projection from SC to IC, and the auditory projection from IC to SC collectively represent the

anatomical substrate for early audiovisual interactions in the brain. However, the physiological correlate of this reciprocal anatomical connectivity remains unclear. In the present study, our aim was to identify the physiological signatures of functional interaction between the IC and SC, with primary focus on identifying the source of visual inputs to the IC, and elucidating the mechanism by which these inputs modulate IC neural activity. To address these questions, we recorded both stimulus evoked and spontaneous neural activity from the IC and SC in the anesthetized ferret. In the IC, we found that visual stimuli modulate the phase of LFPs in two distinct frequency bands (6-10Hz and 15-30Hz) and that the timing of visual responses across the midbrain suggests the SC as a source of visual input. Functional connectivity analysis additionally indicates that the SC to IC visual projection is visuotopic. As the first such demonstration of functional connectivity between the IC and SC, these findings provide a physiological context for previously identified anatomical pathways, and underscore the importance of early multisensory interactions in the brain.

## Materials and Methods

Data presented in this study were collected from 20 simultaneous penetrations of the SC and IC in six adult female ferrets (*Mustela putorius*). All experiments were approved by the independent Hamburg state authority for animal welfare (BUG-Hamburg) and were performed in accordance with the guidelines of the German Animal Protection Law.

### *Surgery*

Animals were initially anesthetized with an injection of ketamine (15mg/kg). A glass tube was then placed in the trachea to allow artificial ventilation of the animal and supply isoflurane anesthesia (0.5-1%, 1:1 NO - O<sub>2</sub> mix). To prevent dehydration throughout experiments, a cannula was inserted into the femoral vein to deliver a continuous infusion of 0.9% NaCl, 0.5% NaHCO<sub>2</sub> and pancuronium bromide (6µg/kg/h). Body temperature was maintained at 38°C with a heating blanket controlled in a custom-made feedback loop by the animal's rectal temperature. The temporalis muscle was reflected, and a rectangular-shaped craniotomy was performed over the left posterior cortex. After careful removal of the dura, the cortex was covered with saline solution. To ensure monocular stimulation, the left eye was occluded with a contact lens placed on the right eye.

### *Electrophysiology*

Neural activity in the SC and IC was recorded simultaneously with 2x16 channel dual-shank (100µm electrode spacing, 500µm inter-shank distance) and 1x32 channel single-shank (50µm or 100µm electrode spacing) silicon probes respectively (NeuroNexus Technologies). All silicon probe contacts had a surface area of 413µm<sup>2</sup>, providing optimal impedance for measuring multi-neuronal spiking activity and the local field potential. Probes were advanced simultaneously towards the midbrain along stereotactic coordinates. Desirable recording configurations were obtained when robust spiking activity was evoked by visual stimuli on

the SC probe and auditory stimuli on the IC probe. Broadband signals from silicon probes were digitized at 22321.4 Hz and sampled with an AlphaLab SnR<sup>TM</sup> recording system (Alpha Omega Engineering). All subsequent analysis of neural data was done offline after the completion of experiments.

### *Sensory Stimulation*

To ensure controlled conditions for sensory stimulation, all experiments were carried out in a dark sound attenuated chamber. Auditory stimuli were generated digitally with a sample rate of 96kHz and delivered through a Beyerdynamic speaker located 15cm from the animals right ear. Visual stimuli were generated by Psychophysics Toolbox (Brainard, 1997) and presented on an LCD monitor (Samsung SyncMaster 2233) placed 28.5cm in front of the animal. Auditory stimuli consisted of clicks and pure tones of 2 and 100ms duration respectively. 38 different pure tone frequencies were selected ranging from 500 to 32000Hz. Visual stimuli consisted of very large (40°) flashes for probing visual responses, and smaller flashes (8°) for quantifying visual spatial receptive fields. Multisensory stimuli consisted of flashes and clicks presented with stimulus-offset asynchronies (SOA) ranging from 0-200ms in 10ms steps (with flashes preceding clicks).

### *Data Analysis*

All offline data analysis of broadband neural signals was performed using custom scripts in Matlab (The Mathworks Inc, MA). To assess both stimulus-evoked neuronal output and postsynaptic input in the SC and IC, we examined both the high frequency component (>500 Hz, MUA) and low frequency component (< 200 Hz, LFP) of extracellular fields, which reflect local neuronal activation and the net sum of local post-synaptic potentials respectively (Buzsáki et al., 2012). Multi-neuron spiking activity was detected with a positive and negative threshold using methods outline by Quiroga and coworkers (2004). LFPs were obtained by

firstly low-pass filtering broadband signals at 300 Hz and downsampling to 1395.1 Hz. We used a butterworth filter in both the forward and reverse direction to ensure no phase shift in resultant LFPs. To deconstruct event related fields into their spectral components in a time-resolved manner, LFPs were convolved with a series of Morlet wavelets. To replicate the natural 1/f distribution of extracellular fields and ensure optimal spectral resolution, 30 logarithmically spaced wavelet frequencies were chosen between 4 – 200Hz (wavelet width of 3 standard deviations). On a trial-by-trial basis, wavelets were convolved with LFP signals from 1.5 seconds pre-stimulus to 1.5 seconds post-stimulus in 5ms steps. To compute stimulus related changes in spectral power, spectra were corrected for pre-stimulus baseline activity. The standard deviation of stimulus related spectra were estimated by jackknife random sampling, and significant power changes were defined as time-frequency data points where the mean total power exceeded the prestimulus mean plus two times the estimated standard deviation. To quantify stimulus locked LFP phase modulations, inter-trial phase coherence (IPC) was computed across all trials. Briefly, for each time and frequency, the instantaneous LFP phase in each trial was projected onto a unit circle. The resultant length of the mean unit vector is a quantitative measure of phase consistency over trials, with values close to 0 and 1 indicating very low and very high phase correlation respectively. The statistical significance of IPC values was determined by the Rayleigh statistic at a significance level of  $p < 0.01$  (Fisher, 1993).

Since we recorded neural activity from directly adjacent midbrain structures, we had to ensure that LFP responses observed in one structure were not the result of volume conducted signals propagating from the neighboring structure. Spectral coherence is a measure of the consistency of phase coupling between simultaneously recorded signals and is comprised of components both in the real and imaginary planes. The imaginary part of coherence was chosen instead of conventional coherence because it quantifies exclusively non-zero phase lagged components, thereby eliminating volume conducted signals which propagate with zero phase lag (Nolte et al., 2004). The sign of the imaginary part of

coherence is bound between -1 and 1, and is determined by the relative phase shift between signals. However, for greater simplicity the absolute value of imaginary coherence was used for plotting and population analysis. The statistical significance of imaginary coherence values was determined by methods outlined by Nolte and coworkers (2004). The phase-slope index (PSI) was used as a quantitative measure of the relative latencies of phase-locked signals between the SC and IC (Nolte et al., 2008). Unlike coherence, which is measured for each time point and frequency, PSI measures the relative phase-lag of signals across frequency bands, with the sign of the 'phase slope' indicating the directionality of interaction. PSI values were subsequently transformed into units of standard deviation, as estimated by jackknife random sampling.

## Results

### *Physiological reconstruction of recording position in the SC and IC*

Since both the SC and the IC can be further divided into anatomically and functionally distinct subregions, we analyzed sensory responses with respect to the intrinsic organization of each structure. For this we first identified physiological markers of the placement electrodes relative to the main landmarks of the SC and IC in each penetration. In a previous study, we identified a flash-evoked physiological marker in the SC (Stitt et al., 2013), termed the current source density inflection depth (ID), that corresponds approximately to the anatomical border between the *stratum griseum superficiale* (SGS) and the *stratum opticum* (SO) (Figure 1B). The inflection depth was consistent across recording sessions and animals and was therefore used to align all SC penetrations post-hoc to enable depth wise analysis of neural responses.

In contrast to the SC, which is composed of several lamina, the most relevant landmark in the IC is the border between the external nucleus, and the tonotopically organized central nucleus. Reflecting the tonotopy of the central nucleus, we consistently observed spiking responses that were tuned to the frequency of pure tone stimuli, with the strong tendency for the best frequency to increase with recording depth (Figure 1C). Since the external capsule of the IC displays little or no frequency preference (Aitkin et al., 1975), we selected the most superficial frequency tuned recording contact as a physiological marker to approximate the anatomical border between the external capsule and central nucleus of the IC. All subsequent depth-wise analysis of neural activity in the IC is presented with respect to this marker. Penetrations where no frequency tuning was detected on any recording contact were omitted from depth analysis.

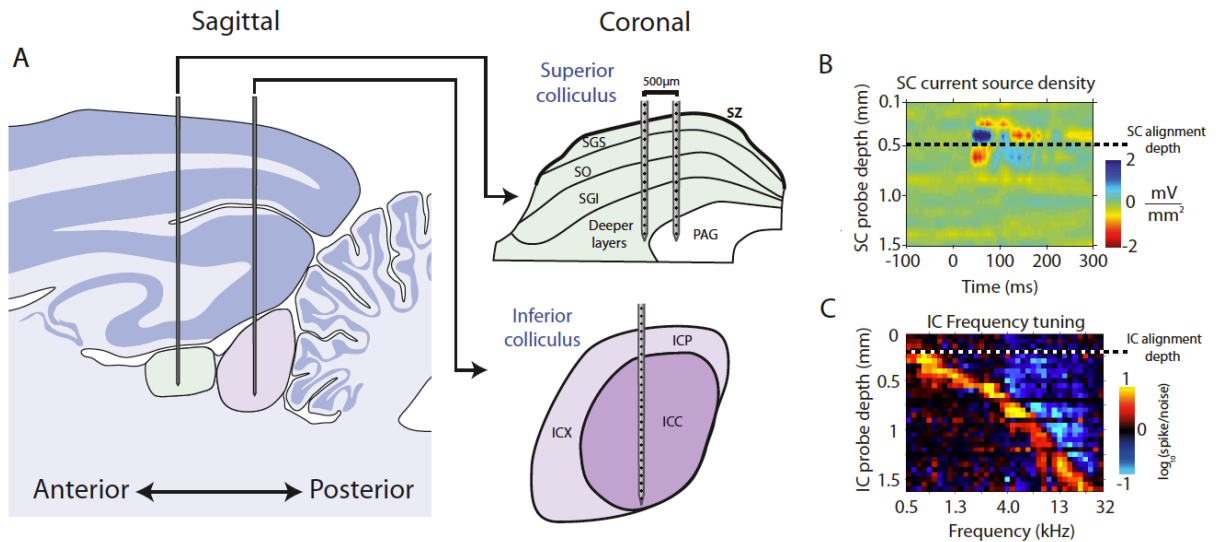


**Figure 1.** Electrode placement and penetration reconstruction. **A:** A dual-shank (16x2) multichannel linear probe was placed in the SC such that electrodes spanned as many layers as possible. Similarly, a single-shank (1x32) multichannel linear probe was placed in the IC such that electrodes spanned both the central nucleus and external capsule. **B:** In the SC, the inflection depth of flash ERPs, or border between current source and sink, reflects the anatomical border between the two superficial SC layers, the SGS and SO. The inflection depth was used to align all penetrations for depth-wise population analysis. **C:** Frequency tuning profile of an example IC penetration. Note that best frequency increases gradually with recording depth in the IC. The most superficial frequency tuned recording site was presumed to reflect the approximate anatomical border between the external capsule and central nucleus in the IC, and was used to align all penetrations for depth-wise analysis.

### *Flash and click evoked responses in the SC*

We detected flash evoked responses in LFPs across the entire dorsoventral extent of the SC, with the largest amplitude responses occurring around the inflection depth, in the superficial SC (Figure 2A). Reflecting this activation pattern, flash stimuli typically evoked robust spiking activity in the superficial and intermediate layers of the SC (Figure 4A). In contrast, click ERPs were lower in amplitude and focused in the deep layers of the SC. Whenever spiking responses were detected following click stimuli, they originated from deep SC recording contacts (Figure 4B).

To investigate flash and click responses in more detail, we broke LFPs down into their spectral components and looked at the stimulus related changes in LFP power, and phase

locking of LFPs to stimuli. Spectral responses to flashes in the SC were typically characterized by large increases in signal power and phase locking in frequencies above 10Hz (Figure 2), and were strongest in superficial layers (Figure 4A). In deep layers, click evoked spectra were characterized by increases in power in high frequencies and significant phase locking across a broader range of LFP frequencies (Figure 4B). Population analysis of flash and click responses across all SC penetrations is shown in Figure 4A & B.

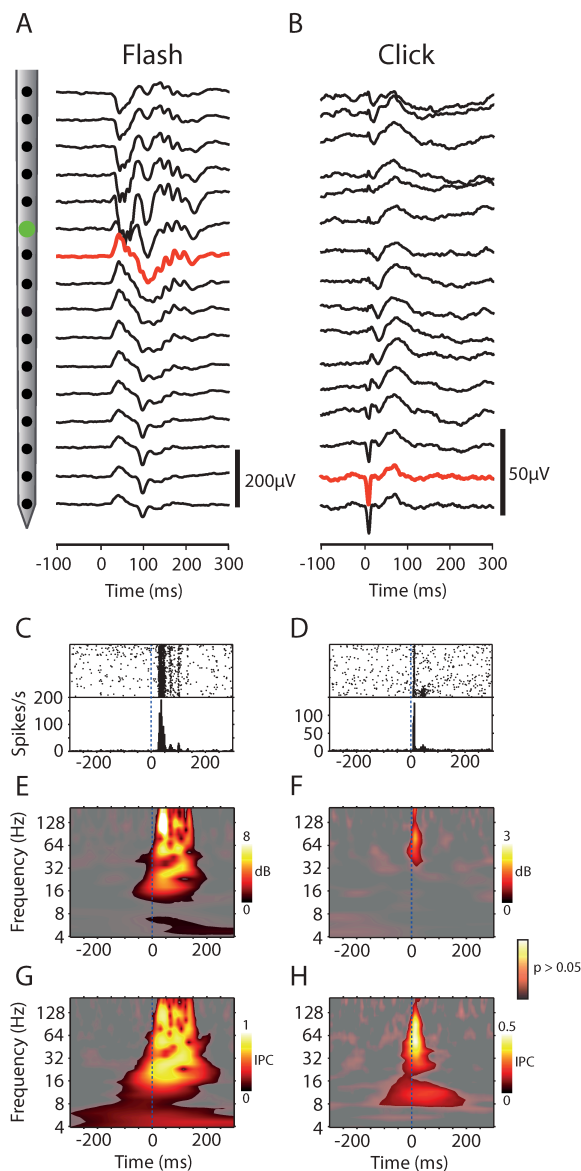


**Figure 2.** Flash and click evoked responses in the SC.

**A & B:** Flash and click ERPs for all 16 probe contacts from one example SC penetration. The inflection depth is marked in green. The responses shown in plots C-H are taken from the recording contacts plotted in red. **C & D:** Raster and PSTH display flash and click evoked spiking activity. **E & F:** Total power spectrograms following flashes and clicks. **G & H:** Intertrial phase coherence spectrograms quantify LFP phase locking to flash and click stimuli. The level of significance for power and intertrial phase coherence spectrograms is displayed by a transparency mask ( $p < 0.05$ ).

### *Flash and click evoked responses in the IC*

IC penetrations were characterized by a noticeable increase in the spike signal to noise ratio, and robust responses to clicks and pure tones usually detected on distributed probe contacts

spanning up to 2.5mm dorsoventrally in the IC (Figure 4D). Following click stimuli, IC neurons displayed sharp increases in firing rate (Figure 3C), with the largest amplitude spiking responses originating from tonotopic regions (Figure 4D). Click ERPs displayed brief positive and negative deflecting components (Figure 3A), with the positive deflecting component more pronounced in superficial regions, and negative deflecting component in deeper regions (Figure 4D). Click evoked LFP latencies displayed a bow-like shape across IC depth, with shortest latencies in central tonotopic regions and slower latencies in the presumed external nucleus (Figure 4C). Spectral responses to clicks in the IC were characterized by very large and significant increases in total power and phase locking across all measured LFP frequencies (Figure 3E & G).

In contrast to auditory stimuli, we did not observe a single case in which visual flash stimuli evoked spiking activity in the IC (Figure 4C). However, closer inspection of flash ERPs revealed a clear stimulus related modulation of LFPs on numerous probe contacts (Figure 3B). Flash responses were characterized by low amplitude periodic deflections in ERPs. We consistently observed similar flash ERPs in nearly all IC penetrations (Figure 4C). Spectral analysis of LFPs from the example recording site in Figure 3 revealed little change in LFP power following flash stimuli. However, LFP spectra displayed strong and highly significant phase locking in two distinct frequency bands: 6-10Hz and 15-30Hz (Figure 3H). To determine if visual modulations of IC neural activity modify subsequent auditory responses, we presented flashes and clicks together with stimulus offset asynchronies varying from 0 to 200ms. Multisensory responses did not deviate from unisensory auditory responses at any of the stimulus offset asynchronies measured (data not shown).

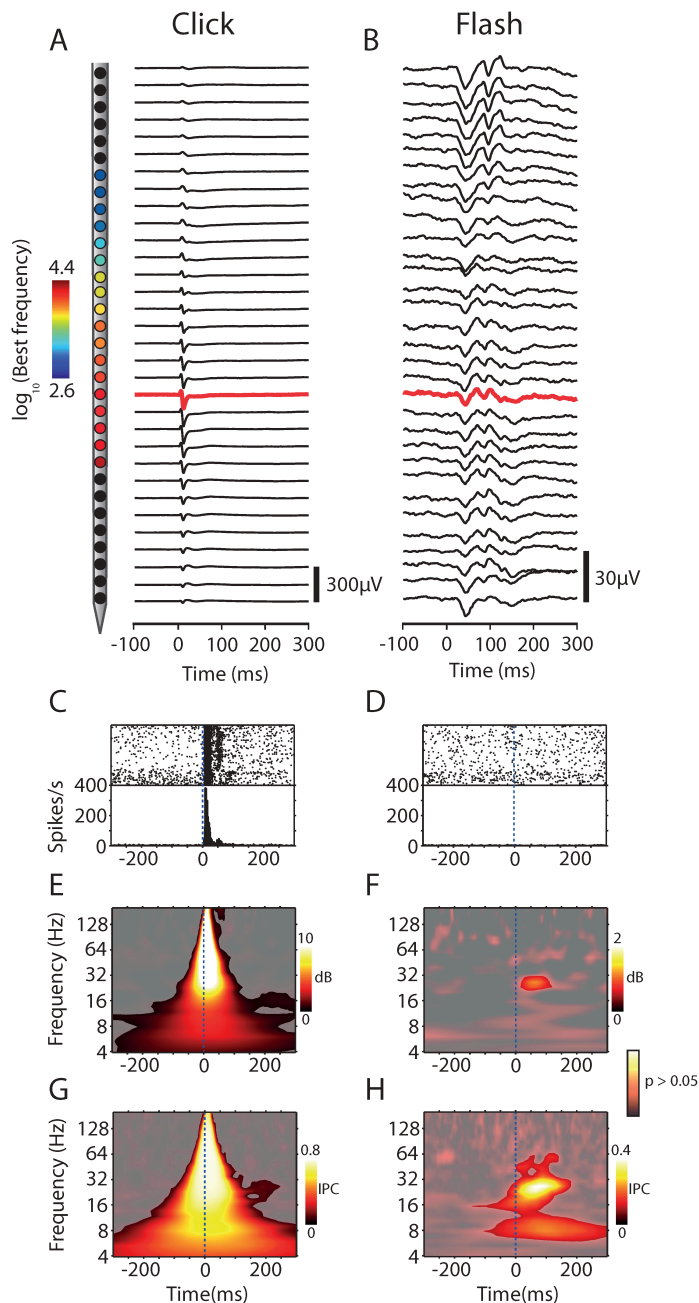


**Figure 3.** Click and Flash evoked responses in the IC. **A & B:** Click and flash ERPs for all 32 probe contacts on from one example IC penetration. The best frequency for tonotopic recording sites is displayed in A. The responses shown in plots C-H are taken from the recording contact plotted in red. **C & D:** Raster and PSTH display click and flash evoked spiking activity. **E & F:** Total power spectrograms following clicks and flashes. **G & H:** Intertrial phase coherence spectrograms quantify LFP phase locking to click and flash stimuli. Note the presence of significant phase locking to flash stimuli in the 6-10Hz and 15-30Hz frequency bands. The level of significance for power and intertrial phase coherence spectrograms is displayed by a transparency mask ( $p < 0.05$ ).

### *Flash stimuli preferentially modulate LFP phase and not power in the IC*

To see if the combination of insignificant power and significant phase locking was consistent for visual responses across all IC recording sites, we computed the stimulus evoked average increase in power and phase locking for all LFP frequencies (Figure 4). We found that 8% ( $0.13 \pm 0.02$  dB) and 16% ( $0.31 \pm 0.02$  dB) of IC recording sites displayed significant power changes in the phase locked 6-10Hz and 15-30Hz frequency bands respectively ( $p < 0.05$ ).

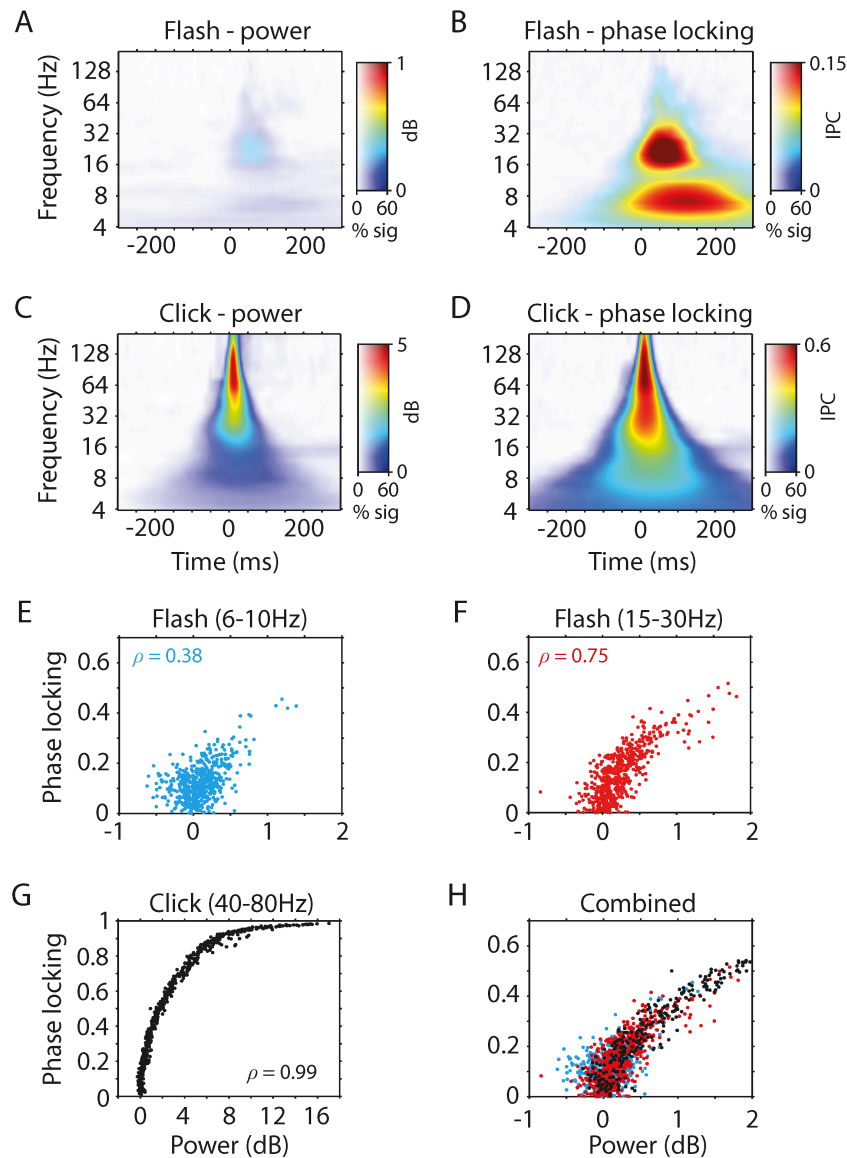


**Figure 4.** Flash and click population spectrograms in the IC. **A:** The population averaged power spectrogram for flash stimuli. Note the absence of any large or significant increases in power associated with flashes. **B:** The population averaged intertrial phase coherence spectrogram for flash stimuli. Note the large amplitude and highly significant phase locking in two distinct frequency bands: 6-10hz and 15-30Hz. **C:** Population averaged total power spectrogram for click stimuli. **D:** Population averaged intertrial phase coherence spectrogram for click stimuli. Note the large and highly significant power and phase locking in almost all LFP frequencies following click stimuli. In each spectrogram plot, average spectra are covered with a transparency mask denoting the percentage of recording sites with significant power or phase modulations ( $p < 0.05$ ). **E & F:** Flash evoked power plotted against the strength of phase locking for all IC recording sites in the 6-10Hz and 15-30Hz frequency bands. Note the strong positive correlation between power and phase locking for both phase locked frequency bands. **G:** Click evoked power plotted against the strength of phase locking. **H:** The data from E-G displayed together on the same plot. In each plot,  $\rho$  denotes the Spearman correlation coefficient, which was significant in all plots ( $p < 0.001$ ).

In contrast, 64% ( $0.14 \pm 0.004$  IPC) and 62% ( $0.18 \pm 0.005$  IPC) of IC recording sites displayed significant phase locking in the 6-10Hz and 15-30Hz frequency bands respectively, indicating that flash stimuli preferentially modulate the phase of LFPs and not power. In contrast to visual stimuli, click stimuli consistently evoked significant changes in power ( $76\%$  &  $4.74 \pm 0.20$  dB) and phase locking ( $91\%$  &  $0.91 \pm 0.01$  IPC) in the 40-80Hz frequency range (Figure 4). To compare visual responses between the central and external nuclei of the IC, we grouped recording sites into frequency tuned and untuned groups. Untuned recording sites displayed significantly stronger phase locking in both the 6-10Hz ( $0.12 \pm 0.006$  IPC tuned, vs  $0.15 \pm 0.005$  IPC untuned) and 15-30Hz ( $0.14 \pm 0.006$  tuned, vs  $0.18 \pm 0.006$  untuned) frequency bands ( $p < 0.001$ ).

To investigate the relationship between phase locking and changes in signal power in more detail, we plotted the strength of evoked power against IPC for all IC recording sites in the 6-10Hz and 15-30Hz bands for flashes, and the 40-80Hz band for clicks (Figure 5). Although IPC best characterized visual responses in the IC, visual evoked power and phase locking were positively correlated in both the 6-10Hz (Spearman correlation = 0.38,  $p < 0.001$ ) and 15-30Hz (Spearman correlation = 0.75,  $p < 0.001$ ) frequency bands. Similarly, click responses displayed a very tight correlation between evoked power and phase locking (Spearman correlation = 0.99,  $p < 0.001$ ). Despite flash stimuli displaying a much larger range of power values, when plotted together, the relationship between evoked power and phase locking is indistinguishable for flash and click responses in the IC (Figure 5H).

#### *Visually evoked LFP phase modulations are intrinsic to the IC*

For the most part, LFPs reflect the net sum of post-synaptic potentials of neurons in tissue immediately surrounding the recording electrode (Buzsáki et al., 2012). However, large and highly synchronous events can be recorded at greater distances from recording electrodes due to the effects of volume conduction. Therefore, to confirm the local origin of visually evoked activity in the IC, we had to ensure that responses were not spuriously produced by volume

conducted signals originating from the directly adjacent, and highly visual sensitive SC.

Volume conducted signals travel through tissue instantaneously, so if visual responses in

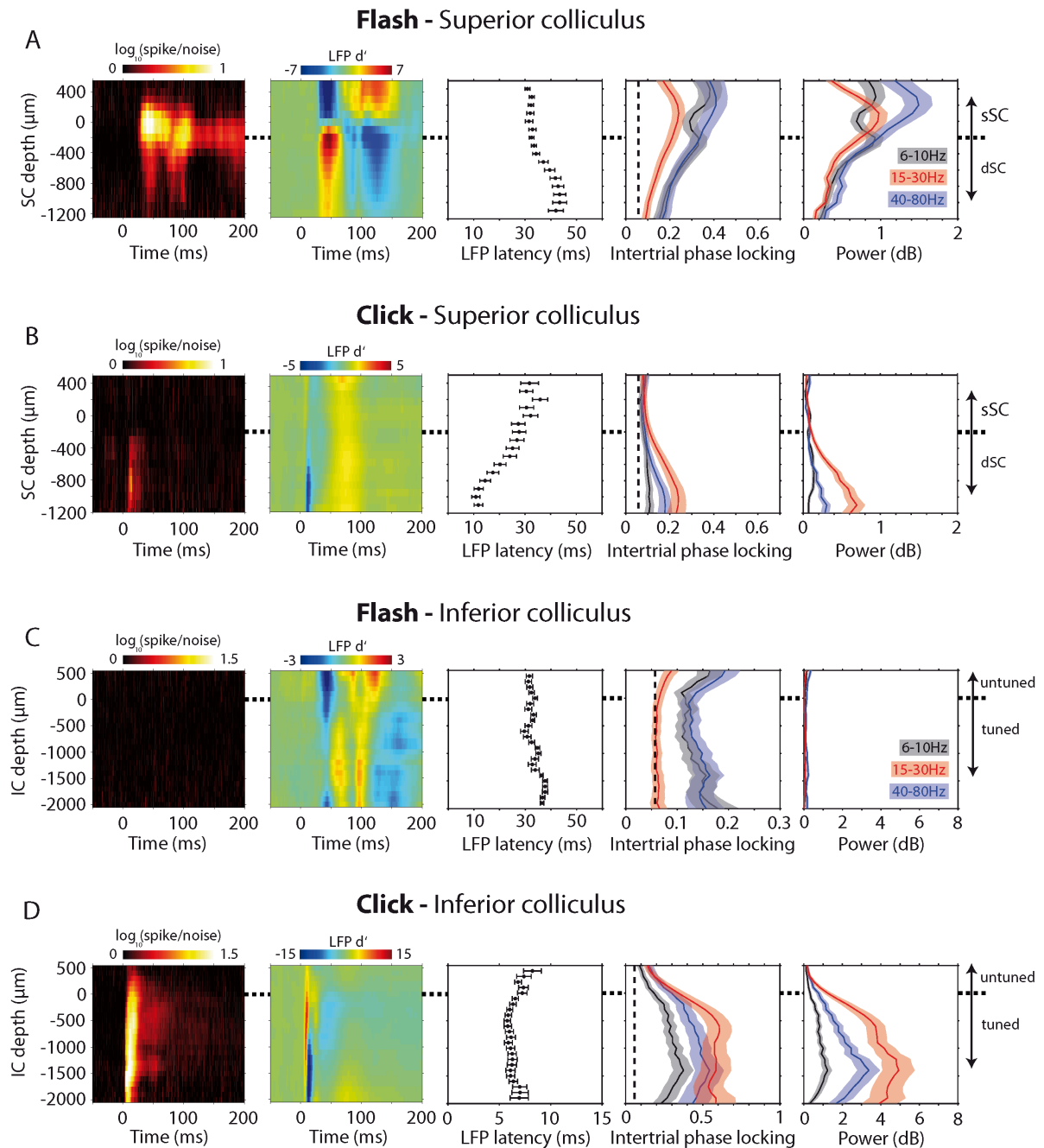


**Figure 5.** Depth resolved measures of sensory responses in the SC and IC. From top to bottom, each row displays depth-resolved population average responses to flashes (A) and clicks (B) in the SC, and flashes (C) and clicks (D) in the IC. From left to right, each column displays the population averaged spike to noise ratio, event related potentials, LFP response latency, intertrial phase locking, and stimulus evoked power. LFP latencies are plotted as the mean  $\pm$  SEM. Spectral analysis was performed in three distinct frequency bands: 6-10Hz, 15-30Hz and 40-80Hz. The level of significant phase locking is plotted as a dotted line for intertrial phase coherence plots ( $p < 0.05$ ).

the IC were a product of volume conduction, then LFPs recorded simultaneously in the SC and the IC will display phase locking with zero phase lag. Since we recorded neural activity from the SC and IC simultaneously, we were able to test this hypothesis by computing the imaginary part of coherence between SC and IC LFP responses (see methods). The flash-evoked imaginary coherence spectrogram computed between all pairs of superficial SC and IC recording contacts reveals non-zero phase correlation in the phase modulated 15-30 Hz frequency band ( $0.12 \pm 0.002$ , 65% significant channel pairs). Deep SC and IC channel pairs displayed a similar effect with slightly lower magnitude ( $0.09 \pm 0.001$ , 53% significant channel pairs). In contrast, the lower 6-10Hz phase modulated band showed weaker imaginary coherence computed for both superficial SC ( $0.05 \pm 0.001$ , 26%) and deep SC ( $0.07 \pm 0.001$ , 39%) recording contacts. For comparison, click stimuli produced strong imaginary coherence between the IC and deep SC for LFP frequencies above 20Hz (Figure 6,  $0.16 \pm 0.002$ , 61%) and comparatively weak coherence with superficial SC ( $0.07 \pm 0.001$ , 36%).

#### *The temporal order of flash and click evoked responses in the midbrain*

To gain a better understanding of the relative timing of sensory responses in the midbrain, we computed the stimulus evoked phase slope index (PSI) between SC and IC LFPs. In this context, the PSI returns a score that indicates the strength with which phase locked signals from each structure precede or follow each other, with positive values indicating the SC leads the IC, and negative values that the IC leads the SC. Visually evoked PSI values were computed across the phase-locked 15-30Hz frequency band. Visual responses in the superficial SC consistently preceded IC responses with an average phase lag of  $5.1 \pm 0.2$  ms (Figure 6C). However, transitioning from superficial to deep SC, the polarity of PSI values flips such that IC visual responses precede deep SC responses by  $5.3 \pm 0.4$  ms. Taken together, these data indicate that flash responses in the 15-30Hz frequency band occur first in

superficial SC, then in the IC, and finally in the deep SC. Since click evoked responses were generally much faster than visual responses, click evoked PSI values were computed in the 80-150Hz frequency band. IC responses were consistently faster than deep SC responses with an average phase lag of  $1.6 \pm 0.03$  ms (Figure 6F), with no effect in superficial SC layers.

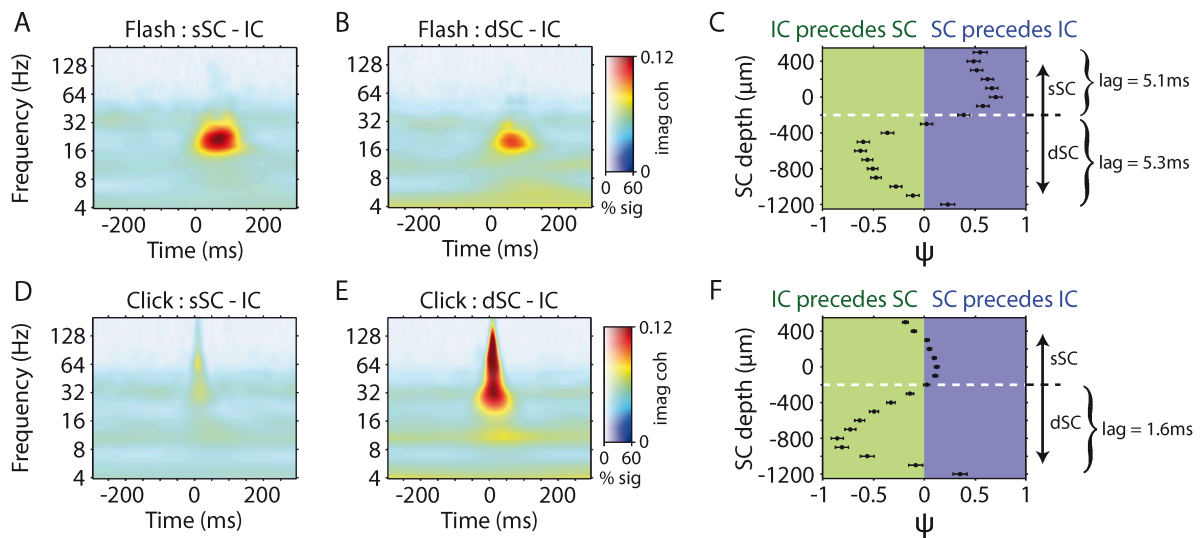


**Figure 6.** Imaginary coherence and temporal order of sensory responses in the midbrain. **A:** Population averaged flash evoked imaginary coherence spectrogram computed between superficial SC and IC recording contacts. **B:** Population averaged flash evoked imaginary coherence spectrogram computed between deep SC and IC recording contacts. Note the presence of significant non-zero phase lagged coherence in the 15-30Hz frequency band following flash stimuli for both superficial and deep SC recording sites. **C:** The average ( $\pm$ SEM) flash evoked phase slope index computed between SC channels at varying depths and IC channels. Positive PSI values indicate that the SC leads the IC, and negative values the IC leads the SC. Note the flip in temporal order of visual responses around the superficial/deep border in the SC. **D:** Population averaged click evoked imaginary coherence spectrogram computed between superficial SC and IC. **E:** Population averaged click evoked imaginary coherence spectrogram computed between deep SC and IC. Note the strength of click evoked coherence in higher LFP frequencies between deep SC and IC recording sites. **F:** The average ( $\pm$ SEM) click evoked phase slope index between SC and IC channels. Note that auditory responses in deep layers of the SC are consistently preceded by responses in the IC.

*Visual receptive field similarity predicts strength of functional connectivity between the SC and IC*

In 10 penetrations from 3 animals, we quantified visual spatial receptive fields in the SC and IC using the strength of phase locking in the 15-30Hz frequency band (Figure 7). IC receptive fields were often very large, encompassing the majority of the contralateral visual field (average RF width  $41 \pm 2.1^\circ$  and height  $28 \pm 1.3^\circ$ ). We reasoned that if the SC provided visual input to the IC, then corecorded SC and IC regions with similar visual receptive fields should display greater functional connectivity at rest compared to regions with dissimilar receptive fields. To quantify the similarity of SC and IC receptive fields, we computed the correlation coefficient of receptive field mapping matrices. For functional connectivity analysis between the SC and IC, we computed imaginary coherence in the 15-30Hz frequency band from spontaneously recorded LFPs. There was a highly significant positive correlation between RF similarity and spontaneous coherence ( $R = 0.26$ ,  $p < 0.0001$ , Figure 7C), indicating that retinotopically similar recording sites in the SC and IC display stronger functional connectivity in the absence of sensory stimuli.

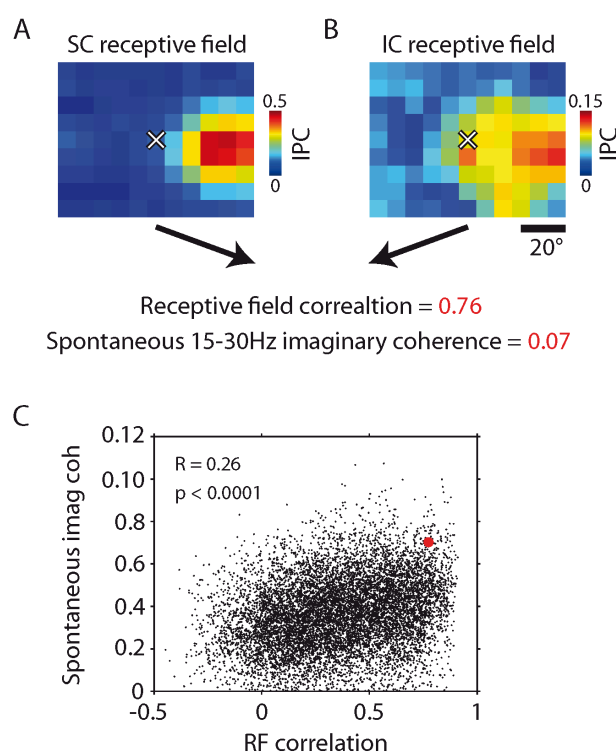


**Figure 7.** Correlation of receptive field similarity and spontaneous coherence. **A & B:** Display visual receptive fields in the SC (**A**) and IC (**B**) from one example recording. Receptive fields were quantified using the strength of intertrial phase coherence in the 15-30Hz frequency band. **C:** A scatter plot of all SC – IC channel pair combinations with receptive field similarity on the x-axis and the strength of spontaneous imaginary coherence in the 15-30Hz band on the y-axis. The data point representing the channel pair shown above is plotted in red. Note the highly significant positive correlation between RF similarity and spontaneous coherence.

## Discussion

To summarize, this study demonstrates that visual stimuli modulate IC neural activity in the anesthetized ferret. While visual responses were not characterized by changes in spiking activity, we consistently observed visually evoked phase locking of IC oscillations in the 6-10Hz and 15-30Hz frequency bands. Although responses were found throughout the IC, they were strongest for untuned recording sites that were located in the presumed external nucleus. IC visual responses occurred slightly later than responses in the superficial SC, but slightly earlier than responses in the deeper SC layers, suggesting that visual responses were neither the product of direct retinal or cortical inputs. Indeed, functional connectivity analysis performed on spontaneous LFPs strongly points to the SC as the source of visual inputs to the IC. By extension, the SC to IC projection may represent the point of entry for visual information into the both the ascending and descending auditory pathways.

### *Non-auditory activity in the inferior colliculus*

Previous studies have identified visually evoked activity from the IC in anaesthetized cats (Tawil et al., 1983; Mascetti and Strozzi, 1988), owls (Gutfreund et al., 2002; Bergan and Knudsen, 2009), and awake and behaving monkeys (Porter et al., 2007; Bulkin and Groh, 2012). In addition, Groh and colleagues found that IC neurons in monkeys also carry saccade (Porter et al., 2007) and eye position related signals (Groh et al., 2001; Porter et al., 2006). Similar to our results, Bulkin and Groh (2012) found that the prevalence of nonauditory activity in the IC was higher in the external nucleus than in the tonotopically organized central nucleus. However, in contrast to such previous studies, we did not detect visual responses in the spiking activity of IC neurons. The discrepancy between visually evoked spiking and LFP activity reported here indicates that while visual inputs produce postsynaptic potentials in IC neurons, these inputs are not sufficient to push neurons past spiking threshold (Buzsáki et al., 2012). This lack of visually evoked spiking may be due to the effects of

anesthesia, where behaviorally relevant inputs are absent. Supporting this view, previous studies reported that approximately 9% of IC cells are visually responsive in the anesthetized cat (Tawil et al., 1983; Mascetti and Strozzi, 1988), whereas 64% of IC cells were found to be visually or eye-position sensitive in awake behaving monkeys (Porter et al., 2007).

The functional relevance of visual activity at the level of the IC remains poorly understood. However, one prominent idea is that audiovisual interaction at the level of the midbrain acts as an interface for the coregistration of visual and auditory space (Gruters and Groh, 2012). Our finding that retinotopically similar recoding sites in the SC and IC display stronger functional connectivity is certainly consistent with the hypothesis that this projection carries visual spatial signals. In addition, Hyde and Knudsen (2002) showed that auditory spatial maps in the owl IC were displaced in animals that were raised wearing optical prisms over their eyes, suggesting that visual inputs ensure the alignment of sensory maps by informing auditory spatial plasticity in the IC. However unlike owls, ferrets and primates move their eyes relative to their heads, indicating that a different and highly adaptive mechanism is required for the alignment of visual and auditory space. Groh and colleagues (Groh et al., 2001) provided evidence for this mechanism by showing that eye-position signals modulate the amplitude of auditory responses in monkey IC neurons, with maximum amplitude responses occurring when the animal's gaze was in the contralateral visual hemifield. Aside from modulating auditory responses, eye opposition signals also modulate the gain of spontaneous spiking activity in the IC. Therefore, rather than representing a form of classic multisensory integration, as described by Stein and Meredith (1993), visual and eye-position signals act to modulate the gain of auditory signals in the IC. This form of activity is more appropriately labeled multisensory enhancement (Kayser et al., 2008), since unimodal activity is subtly modulated by inputs from another modality. We did not observe the visually driven enhancement or suppression of auditory responses in the IC, however such multisensory effects may be absent in anesthetized animals. Indeed, previous studies have shown nonauditory activity in the IC is highly context and behaviorally dependent (Groh et

al., 2001; Porter et al., 2007). An alternative explanation for the lack of multisensory enhancement may be that the temporal resolution of SOAs used (0-100ms in 10ms steps) was not sufficient to capture such multisensory effects, since IC neurons temporally integrate inputs in the range of milliseconds rather than tens of milliseconds (Ter-Mikaelian et al., 2007). Nevertheless, the fact that visual stimuli influence activity at such an early stage of auditory processing highlights how important the interaction of different sensory modalities is in the brain. This study provides strong evidence that even at the level of the IC, signals propagating along the ascending auditory pathway are already essentially multisensory in nature.

#### *Functional connectivity in the midbrain*

Anatomical tracing studies have identified a number of potential sources of visual input to the IC. Itaya and Van Hoesen (1982) showed in rats and monkeys that the IC receives direct innervation from the contralateral retina, with axons terminating in the pericentral nucleus. Several other groups subsequently reproduced this finding in rats (Yamauchi and Yamadori, 1982), cats (Cooper and Cowey, 1990), and mole-lemmings (Herbin et al., 1994). At the level of the midbrain, the IC receives inputs from both superficial and deep layers of the ipsilateral SC, with the highest density projection to the nucleus brachium and the external nucleus of the IC (cat: Adams, 1980; rat: Coleman and Clerici, 1987; bat: Covey et al., 1987; ferret: Doubell et al., 2000). Finally, descending projections from the visual cortex terminate in the external nucleus of the IC as well as the medial part of the central nucleus (Cooper and Young, 1976). Collectively, these bottom-up and top-down inputs presumably work in unison in behaving animals to modulate auditory spatial signals in the IC. However, physiological evidence reported here suggests the SC as the primary driver of visually evoked activity in the IC. Doubell and colleagues (2000) provided further evidence that the SC drives visual activity in the IC by showing that electrical stimulation of the superficial SC *in vitro* evokes excitatory postsynaptic potentials (EPSP) in IC neurons. The latencies of electrically evoked

monosynaptic EPSPs *in vitro* are slightly longer than the relative phase lag of SC and IC visual responses reported here (5ms *in vivo*; 7ms *in vitro*). However, when axon conductance is corrected for the lower recording temperature of *in vitro* preparations then electrically and stimulus evoked latencies are in strong agreement (Franz and Iggo, 1968). Since the SC is highly integral in the formation of saccadic eye movements (Gandhi and Katnani, 2011), it is likely that the same SC to IC anatomical pathways conveying visual information also mediate the transfer of eye-position information, however this remains to be confirmed in awake and behaving animals.

In the opposing direction, the nucleus brachium and external nucleus of the IC provide dense auditory inputs to deep layers of the SC (King et al., 1998a). In addition, the lateral lemniscus, sagulum, and periolivary nuclei of the brainstem provide sparse auditory inputs to the ferret SC. The slight delay of auditory response latencies (~1.6ms) between IC and SC is certainly consistent with an IC to SC auditory projection. Auditory inputs to the SC converge to form a map of auditory space that is aligned with the retinotopic visual map in superficial SC layers (Stein and Meredith, 1993; King et al., 1998b). Similar to the hypothesized function of audiovisual interaction in the IC, the alignment of visual and auditory maps between deep and superficial SC layers is highly dynamic, with the representation of auditory space constantly readjusted to account for eye movements (Populin and Yin, 2002).

#### *Sensory evoked LFP phase modulation as a mechanism for multisensory interaction*

Previous studies have interpreted the coexistence of insignificant changes in signal power and significant phase locking as evidence for the stimulus evoked reorganization of the phase of ongoing LFP oscillations (Makeig et al., 2002). Visually evoked LFP responses in the IC certainly match these criteria, nicely mirroring previous findings from the auditory cortex in monkeys, where somatosensory (Lakatos et al., 2007) and visual stimuli (Kayser et al., 2008; Lakatos et al., 2009) have been shown to modulate the phase of ongoing LFPs. Similar phase resetting has also been observed in the somatosensory cortex in mice (Sieben et al., 2013) and

the visual cortex in humans (Naue et al., 2011). Although the mechanism of oscillatory phase reset has often been claimed, few studies have thoroughly investigated this phenomenon from a biophysical perspective. As we have shown here, it is very difficult to disentangle phase modulations from changes in power since these two variables are so tightly interdependent for responses to transient stimuli. We believe that rather than signifying a reset in oscillatory phase, the presence of phase locking in the apparent absence of power change simply reflects the greater sensitivity of phase locking measures for quantifying weak LFP responses. Conceptually, any barrage of sensory evoked inputs will produce synchronous postsynaptic potentials in target neurons that would be detectable as amplitude fluctuations in electrical fields (Buzsáki et al., 2012). That is to say, even if inputs act to reset the phase of ongoing oscillations, changes in the power of LFPs are unavoidable. Perhaps a more adept measure should be developed that encompasses both stimulus evoked power and phase locking, to avoid further confusion surrounding the underlying biophysical processes that govern stimulus evoked responses in the brain.

## References

- Adams J (1980) Crossed and descending projections to the inferior colliculus. *Neurosci Lett* 19:1–5.
- Bergan JF, Knudsen EI (2009) Visual modulation of auditory responses in the owl inferior colliculus. *J Neurophysiol* 101:2924–2933.
- Bizley JK, King AJ (2009) Visual influences on ferret auditory cortex. *Hear Res* 258:55–63.
- Bizley JK, Nodal FR, Bajo VM, Nelken I, King AJ (2007) Physiological and anatomical evidence for multisensory interactions in auditory cortex. *Cereb Cortex* 17:2172–2189.
- Brainard D (1997) The psychophysics toolbox. *Spat Vis* 10:433–436.
- Bulkin D a, Groh JM (2012) Distribution of visual and saccade related information in the monkey inferior colliculus. *Front Neural Circuits* 6:61.
- Buzsáki G, Anastassiou C a, Koch C (2012) The origin of extracellular fields and currents--EEG, ECoG, LFP and spikes. *Nat Rev Neurosci* 13:407–420.
- Coleman JR, Clerici WJ (1987) Sources of projections to subdivisions of the inferior colliculus in the rat. *J Comp Neurol* 262:215–226.
- Cooper a M, Cowey a (1990) Development and retraction of a crossed retinal projection to the inferior colliculus in neonatal pigmented rats. *Neuroscience* 35:335–344.
- Cooper MH, Young P a (1976) Cortical projections to the inferior colliculus of the cat. *Exp Neurol* 51:488–502.
- Covey E, Hall WC, Kobler JB (1987) Subcortical connections of the superior colliculus in the mustache bat, *Pteronotus parnellii*. *J Comp Neurol* 263:179–197.
- Doubell TP, Baron J, Skalióra I, King a J (2000) Topographical projection from the superior colliculus to the nucleus of the brachium of the inferior colliculus in the ferret: convergence of visual and auditory information. *Eur J Neurosci* 12:4290–4308.
- Fisher NI (1993) *Statistical analysis of circular data*. Cambridge University Press.
- Franz D, Iggo A (1968) Conduction failure in myelinated and non-myelinated axons at low temperatures. *J Physiol*:319–345.
- Gandhi NJ, Katnani H a (2011) Motor functions of the superior colliculus. *Annu Rev Neurosci* 34:205–231.
- Groh JM, Trause a S, Underhill a M, Clark KR, Inati S (2001) Eye position influences auditory responses in primate inferior colliculus. *Neuron* 29:509–518.
- Gruters KG, Groh JM (2012) Sounds and beyond: multisensory and other non-auditory signals in the inferior colliculus. *Front Neural Circuits* 6:96.

- Gutfreund Y, Zheng W, Knudsen EI (2002) Gated visual input to the central auditory system. *Science* 297:1556–1559.
- Herbin M, Repérant J, Cooper HM (1994) Visual system of the fossorial mole-lemmings, *Ellobius talpinus* and *Ellobius lutescens*. *J Comp Neurol* 346:253–275.
- Hyde P, Knudsen E (2002) The optic tectum controls visually guided adaptive plasticity in the owl's auditory space map. *Nature* 415:73–76.
- Itaya S, Hoesen G Van (1982) Retinal innervation of the inferior colliculus in rat and monkey. *Brain Res* 233:45–52.
- Kayser C, Petkov CI, Logothetis NK (2008) Visual Modulation of Neurons in Auditory Cortex. *Cereb Cortex* 18:1560–1574.
- King a J, Jiang ZD, Moore DR (1998a) Auditory brainstem projections to the ferret superior colliculus: anatomical contribution to the neural coding of sound azimuth. *J Comp Neurol* 390:342–365.
- King a J, Schnupp JW, Thompson ID (1998b) Signals from the superficial layers of the superior colliculus enable the development of the auditory space map in the deeper layers. *J Neurosci* 18:9394–9408.
- King AJ, Walker KMM (2012) Integrating information from different senses in the auditory cortex. *Biol Cybern* 106:617–625.
- Lakatos P, Chen C-M, O'Connell MN, Mills A, Schroeder CE (2007) Neuronal oscillations and multisensory interaction in primary auditory cortex. *Neuron* 53:279–292.
- Lakatos P, O'Connell MN, Barczak A, Mills A, Javitt DC, Schroeder CE (2009) The leading sense: supramodal control of neurophysiological context by attention. *Neuron* 64:419–430.
- Makeig S, Westerfield M, Jung TP, Enghoff S, Townsend J, Courchesne E, Sejnowski TJ (2002) Dynamic brain sources of visual evoked responses. *Science* 295:690–694.
- Mascetti GG, Strozzi L (1988) Visual cells in the inferior colliculus of the cat. *Brain Res* 442:387–390.
- Musacchia G, Schroeder CE (2009) Neuronal mechanisms, response dynamics and perceptual functions of multisensory interactions in auditory cortex. *Hear Res* 258:72–79.
- Naue N, Rach S, Strüber D, Huster RJ, Zaehle T, Körner U, Herrmann CS (2011) Auditory event-related response in visual cortex modulates subsequent visual responses in humans. *J Neurosci* 31:7729–7736.
- Nolte G, Bai O, Wheaton L, Mari Z, Vorbach S, Hallett M (2004) Identifying true brain interaction from EEG data using the imaginary part of coherency. *Clin Neurophysiol* 115:2292–2307.
- Nolte G, Ziehe A, Nikulin V, Schlögl A, Krämer N, Brismar T, Müller K-R (2008) Robustly Estimating the Flow Direction of Information in Complex Physical Systems. *Phys Rev Lett* 100:234101.

- Populin LC, Yin TCT (2002) Bimodal interactions in the superior colliculus of the behaving cat. *J Neurosci* 22(7):2826-34
- Porter K, Metzger R, Groh J (2007) Visual- and saccade-related signals in the primate inferior colliculus. *PNAS* 104(45):1826–1842.
- Porter KK, Metzger RR, Groh JM (2006) Representation of eye position in primate inferior colliculus. *J Neurophysiol* 95:1826–1842.
- Quiroga RQ, Nadasdy Z, Ben-Shaul Y (2004) Unsupervised spike detection and sorting with wavelets and superparamagnetic clustering. *Neural Comput* 16:1661–1687.
- Sieben K, Röder B, Hanganu-Opatz IL (2013) Oscillatory entrainment of primary somatosensory cortex encodes visual control of tactile processing. *J Neurosci* 33:5736–5749.
- Stein BE, Meredith MA (1993) *The merging of the senses*. The MIT Press.
- Stitt I, Galindo-Leon E, Pieper F, Engler G, Engel AK (2013) Laminar profile of visual response properties in ferret superior colliculus. *J Neurophysiol* 110:1333–1345.
- Tawil RN, Saadé NE, Bitar M, Jabbur SJ (1983) Polysensory interactions on single neurons of cat inferior colliculus. *Brain Res* 269:149–152.
- Ter-Mikaelian M, Sanes DH, Semple MN (2007) Transformation of temporal properties between auditory midbrain and cortex in the awake Mongolian gerbil. *J Neurosci* 27:6091–6102.
- Yamauchi K, Yamadori T (1982) Retinal projection to the inferior colliculus in the rat. *Acta Anat (Basel)* 114:355–360.

## **Chapter 4**

---

**The dynamics of spontaneously generated neural  
activity between superior colliculus and cortex  
in the anesthetized ferret**

## **Abstract**

In the absence of sensory stimulation or motor output, the brain exhibits complex spatiotemporal patterns of intrinsically generated neural activity. This form of activity is thought to reflect the underlying functional architecture of large-scale neuronal networks in the brain. Here, we investigate the spontaneous interaction between the superior colliculus (SC) of the midbrain and the posterior cortex in the anesthetized ferret. Spontaneous corticotectal interaction was characterized by correlated fluctuations in the amplitude of extracellular fields in the 120-300Hz frequency band. Correlated corticotectal activity typically occurred between recording sites located in superficial and intermediate SC layers, and  $\mu$ ECoG recording sites spanning visual and suprasylvian cortical areas. Brief fluctuations in the power of high frequency oscillations in the cortex were highly correlated to spiking activity in the SC, suggesting that coincident corticotectal power fluctuations reflect correlated spiking activity. Correlated SC and cortical activity was strongly locked to the phase of the cortical slow oscillation ( $\sim 0.7$ Hz). This was also reflected in spiking activity, where SC and cortical spiking activity was strongly locked to the phase of the cortical slow oscillation. SC spikes were additionally locked to the phase of spindle oscillations in the cortex ( $\sim 10$ Hz). Finally, ketamine anesthesia enhanced the slow cortical oscillation, and indirectly increased the intensity of correlated high frequency corticotectal activity. Collectively, our findings reveal that spontaneous activity in the SC is tightly coupled to the state of cortex under anesthesia.

## Introduction

Rather than remaining entirely inactive in the absence of sensory stimuli or motor output, the brain displays complex spatiotemporal activation patterns that are more generally described as ‘ongoing activity’ (Engel et al., 2013). For a long time ongoing activity was thought of as a form of neural noise, that was the net product of random fluctuations in large neural networks. Due to this point of view it became standard practice in neurophysiological experiments to quantify sensory responses by averaging activity over many repetitions of stimuli, thereby eliminating the apparently random fluctuations present on a trial-by-trial basis. However, a seminal study conducted by Arieli and colleagues (1996) showed that the large scale spatiotemporal structure of spontaneously generated brain activity is indeed informative, and shapes the context in which sensory stimuli are processed. Since this pioneering study there has been an explosion in the interest of ongoing activity. Ensuing studies have accumulated evidence that ongoing activity across multiple spatial and temporal scales reflects several inherent properties of functional neural networks (Engel et al., 2013; Hutchison et al., 2013). For example, a recent electrophysiological study in primates showed that spontaneous fluctuations in high frequency cortical potentials reflect the tonotopic organization of the auditory cortex in the absence of auditory stimulation (Fukushima et al., 2012). However, the vast majority of studies on ongoing activity have either focused solely on the cortex (Tsodyks et al., 1999; Mohajerani et al., 2013), the relationship between the cortex and thalamus (Timofeev and Steriade, 1996; Minlebaev et al., 2011), or the relationship between cortex and hippocampus (Sirota et al., 2003; Ji and Wilson, 2007). Therefore, little is known about how other subcortical structures outside of the thalamus and hippocampus spontaneously interact with the cortex.

The superior colliculus (SC) presents itself an interesting model to study such spontaneously generated subcortical-cortical communication because it is highly interconnected with a wide range of sensory and motor cortical areas (Manger et al., 2010). Apart from

receiving numerous “top-down” inputs from the cortex, the SC receives direct visual input from the retina (Berson, 1988a, 1988b), auditory input from the inferior colliculus (Jiang et al., 1997; King et al., 1998), and somatosensory input from the spinal cord and cuneate nucleus (Edwards et al., 1979). Although the SC is highly responsive to sensory stimuli spanning several modalities, it remains unclear how the combination of “bottom-up” sensory inputs, “top-down” cortical inputs, and intrinsic SC network properties collectively shape neural activity in the absence of sensory stimulation. Here, we study the dynamics of spontaneous activity between the SC and cortex by recording neural activity simultaneously from all SC layers with multisite silicon probes, and cortical activity with a custom designed micro electrocorticogram ( $\mu$ ECoG). Under anesthesia, the spontaneous interaction between SC and cortex is characterized by coincident fluctuations in the power of high frequency oscillations. Such briefly correlated corticotectal activity likely reflects correlated spiking activity between the SC and cortex, and is temporally governed by cortical slow ( $\sim 0.7$ Hz) and spindle oscillations ( $\sim 10$ Hz). Together, these data suggest that spontaneous activity in the SC is tightly coupled to the state of cortical networks under anesthesia.

## Materials and Methods

Data presented in this study were collected from four adult female ferrets (*Mustela putorius*). All experiments were approved by the independent Hamburg state authority for animal welfare (BUG-Hamburg) and were performed in accordance with the guidelines of the German Animal Protection Law.

### *Surgery*

Animals were initially anesthetized with an injection of ketamine (15mg/kg). A glass tube was then placed in the trachea to allow artificial ventilation of the animal and supply isoflurane anesthesia (0.5-1%, 1:1 NO - O<sub>2</sub> mix). To prevent dehydration of the animal throughout experiments, a cannula was inserted into the femoral vein to deliver a continuous infusion of 0.9% NaCl, 0.5% NaHCO<sub>2</sub> and pancuronium bromide (6μg/kg/h). Body temperature was maintained at 38°C with a heating blanket controlled in a custom-made feedback loop by the animals rectal temperature. A large craniotomy was then performed over the entire left posterior cortex. After carefully removing the dura, an electrocorticogram was gently placed on the surface of the cortex. A small hole was drilled in the removed piece of skull over the area corresponding to the visual cortex, and the piece of bone was put fixed back in place with silicone elastomer (World Precision Instruments). In one experiment, ketamine anesthesia was maintained for electrophysiological recordings by the continuous infusion of a mixture of medetomidine (0.022mg/kg/h) and ketamine (10mg/kg/h). Following ketamine recordings, anesthesia was switched to the isoflurane regimen. All experiments were carried out in a dark sound attenuated chamber.

### *Custom μECoG design*

For large-scale recordings of cortical potentials, we used a novel polyimide based micro electrocorticogram (μECoG), which was developed to optimally fit to the posterior cortex of

the ferret. The custom  $\mu$ ECoG consisted of three ‘fingers’, each containing three rows of electrodes such that the polyimide foil can bend and conform to the curved surface of the ferret brain. Using microelectromechanical systems technology, it was possible to arrange 64 electrodes and electrode paths in a relatively small area. Electrodes had a diameter of  $250\mu\text{m}$  and were constructed from platinum. Figure 1A displays a schematic diagram of the  $\mu$ ECoG layout. To allow for simultaneous recording of  $\mu$ ECoG signals and intracortical spiking and LFP activity, small holes of  $500\mu\text{m}$  diameter were cut into the polyimide foil in the space between electrodes to allow for the placement of multichannel linear probes (Figure 1).

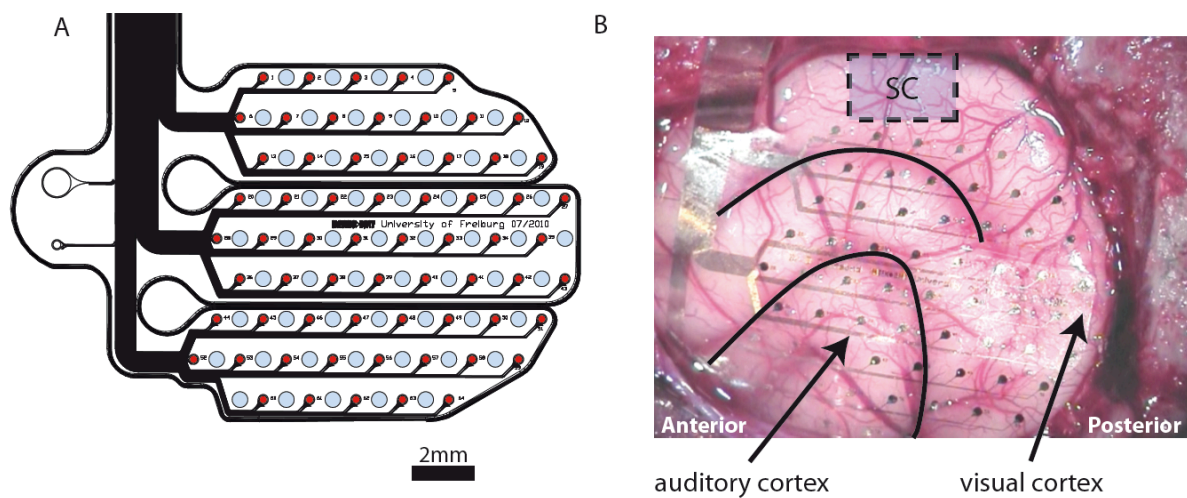


**Figure 1.**  $\mu$ ECoG design and placement. **A:** Displays a schematic diagram of the  $\mu$ ECoG probe that was custom designed for the posterior ferret cortex. Recording contacts of  $250\mu\text{m}$  diameter are shown in red, while holes in the polyimide foil are shown in blue. **B:** A photo of the placement of the  $\mu$ ECoG on the ferret cortex. Note the extensive coverage of both visual and auditory cortical areas. The space between the  $\mu$ ECoG and the midline was sufficiently large to place linear silicon probes to target recordings in the SC.

### *Electrophysiology*

Neural activity in the SC was recorded with  $2 \times 16$  channel dual-shank silicon probes (NeuroNexus Technologies,  $100\mu\text{m}$  electrode spacing,  $500\mu\text{m}$  inter-shank distance). In some experiments, linear  $1 \times 32$  channel ( $100\mu\text{m}$  electrode spacing) probes were inserted into the visual cortex through the small holes in the  $\mu$ ECoG. All silicon probe contacts had a surface area of  $413\mu\text{m}^2$ . Broadband signals from silicon probes were digitized at  $22321.4\text{Hz}$ , while

$\mu$ ECoG signals were digitized at 1395.1Hz. Broadband data from silicon probes and  $\mu$ ECoG signals were both sampled with a 128 channel AlphaLab SnR<sup>TM</sup> recording system (Alpha Omega Engineering).

### *Data Analysis*

All offline data analysis of neural signals was performed using custom software in Matlab (The Mathworks Inc, MA). To extract multiunit spiking activity (MUA) from broadband extracellular recordings, we highpass filtered signals at 500Hz and detected spikes with a positive and negative threshold. LFPs were obtained by low-pass filtering broadband signals at 300Hz. To ensure zero phase shift in resultant LFPs signals were filtered in both the forward and reverse direction. Finally, LFPs were downsampled to a sample rate of 1395.1Hz.  $\mu$ ECoG signals were similarly low-pass filtered below 300Hz. We computed spectral estimates of LFP and  $\mu$ ECoG signals using a series of 80 Morlet wavelets that were logarithmically spaced from 0.1 – 300Hz. Since we wanted to track changes in spectra with high temporal resolution, spectral estimates were computed in a sliding window with steps of 5ms.

*Power correlation:* To quantify the strength with which modulations in the power of SC LFP and  $\mu$ ECoG signals were comodulated, we computed the correlation of spectral power estimates over ~10 minutes of spontaneous recordings. Spectral power was computed by taking the absolute value of the square of complex Fourier spectra. The strength of power correlation between two channels was then defined as the linear correlation coefficient of raw power time series at each frequency. Significant power correlation coefficients were defined as values that exceeded the mean plus two times the standard deviation of the global power correlation matrix ( $p < 0.05$ ). To analyze the slower temporal structure of power correlation, power envelopes were convolved with a series of 30 Morlet wavelets logarithmically spaced from 0.05 – 10Hz. Carrier frequencies of power correlation were then identified by computing the coherence of power envelope spectra.

*Spike-phase locking:* To estimate the dependence of SC spiking activity on the phase of cortical oscillations, we calculated spike phase-locking values (PLV) using spikes recorded from the SC and the phase of intracranial EEG signals (Lachaux et al., 1999). The instantaneous phase of the  $\mu$ ECoG signals at each frequency was defined as the phase angle between the complex and the real component of Fourier spectra. Spike phase angles were projected onto a unit circle as vectors. Spike PLVs were then defined as the magnitude of the mean vector of all spike-phase unit vectors, with the preferred phase of SC spikes being the angle of the resultant mean vector. To avoid bias for population analysis of spike phase locking, we had to ensure that all estimates were computed with the same number of spikes. Therefore, spike PLVs were calculated from 1000 randomly drawn spikes for each channel pair. This process was repeated 100 times to get an estimate of the mean spike PLV. Channels where less than 1000 spikes were detected throughout the entire recording were eliminated from spike phase locking analysis.

*Spike triggered average spectrograms:* We computed time-frequency spectrograms of  $\mu$ ECoG signals locked to the timing of spikes in the SC. Firstly, cortical signals were cut into segments of 3 seconds surrounding the occurrence of spikes in the SC. Time-frequency representations were computed to allow for the estimate of signal power for each spike-cortex 'trial'. Then the spike triggered average power was computed. This process was repeated with randomly generated spike times. Finally mean spike triggered average spectra were subtracted by randomly generated spectra and normalized by standard deviation. This yielded spike triggered average spectra expressed in units of estimated baseline standard deviation.

## Results

We performed simultaneous recordings of cortical potentials from  $\mu$ ECoG and SC neural activity from multichannel probes in 13 penetrations from 4 animals. In one experiment, one additional multichannel linear probe was inserted into the cortex for intracortical recordings.

### *High frequency fluctuations in extracellular fields are correlated between SC and cortex*

LFP and  $\mu$ ECoG signals from the SC and cortex generally reflect the synchronicity of postsynaptic potentials in populations of neurons (Buzsáki et al., 2012). Since these signals generally follow the  $1/f$  power law (Miller et al., 2009), with increasing frequency, LFP oscillations reflect the collective activity of smaller and smaller subpopulations of neurons. Because we were interested in the dynamics of small populations of neurons between the SC and cortex, we focused our analysis on high frequency components of LFP and  $\mu$ ECoG signals. To quantitatively track the waxing and waning of high frequency oscillations over time, we computed time resolved power estimates of LFP and  $\mu$ ECoG signals in 120-300Hz frequency band. Figure 2 displays LFP power timeseries for SC and  $\mu$ ECoG recording contacts from one example recording session. Both SC and  $\mu$ ECoG signals were characterized by the presence of brief increases in signal power in high frequencies. When examined closely, these transient bursts in high frequency activity sometimes occurred coincidentally at SC and cortical recording contacts (Figure 2). We computed the linear correlation coefficient of raw power time series to quantify the degree with which spontaneous power modulations in SC and cortex followed each other. To view power correlation values more intuitively, we selected seed SC channels and generated cortical topographic plots using the strength of power correlation between the SC seed channel and all  $\mu$ ECoG channels. The topographic plot from Figure 2 shows that power correlation was strongest in a cluster of  $\mu$ ECoG channels over the posterior visual cortex. Although there was certainly a focal point where power

correlation was the strongest, moderate power correlation values were also detected for a larger number of recording sites spanning the entire visual cortex (Figure 2).

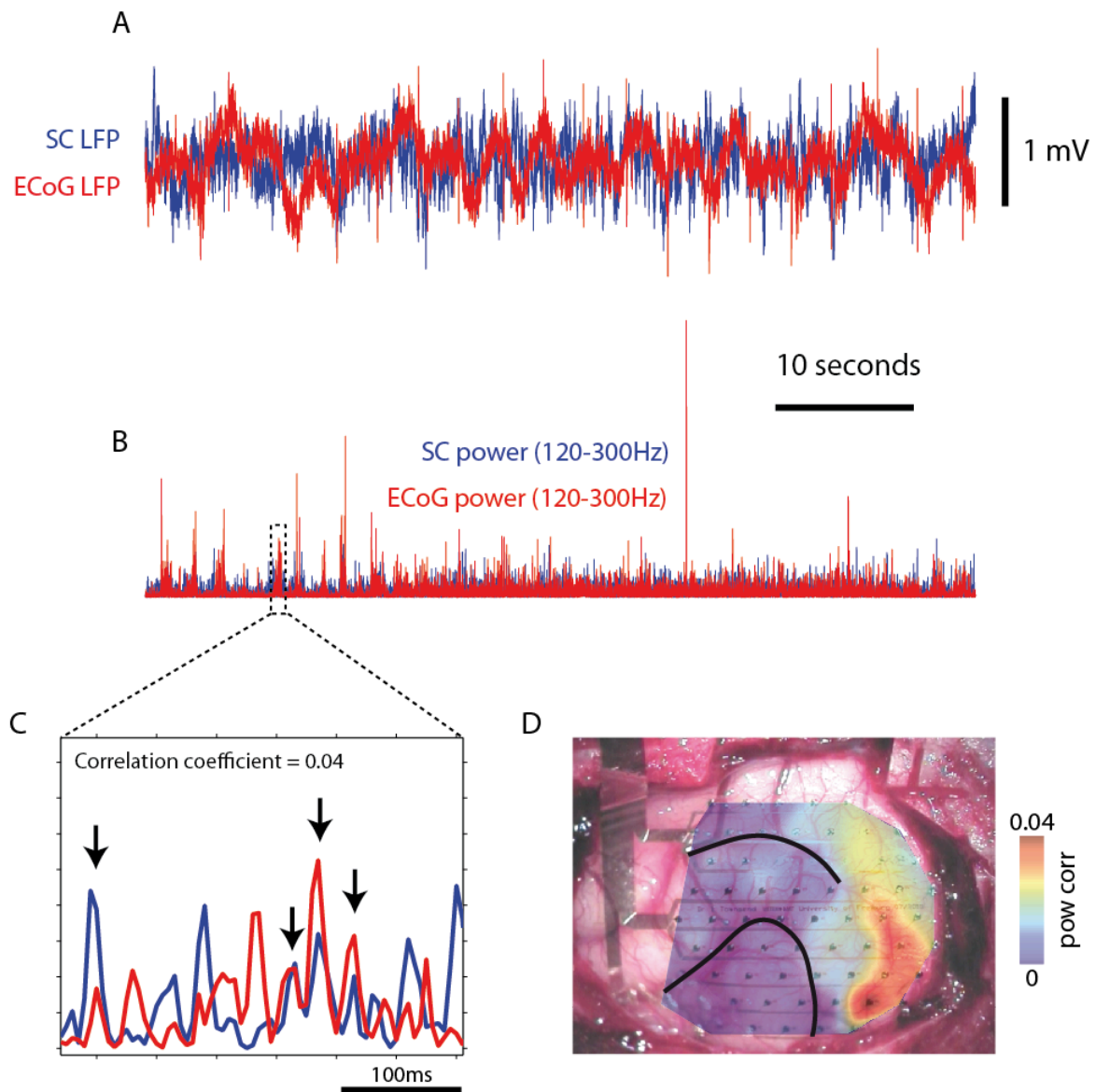


**Figure 2.** The amplitude of high frequency oscillations transiently comodulate between the SC and cortex. **A:** Simultaneously recorded LFP and  $\mu$ ECoG signals from one example recording session. **B:** The high frequency (120-300Hz) power envelope of SC and  $\mu$ ECoG signals plotted in **A**. **C:** Displays a magnified time window from **B**. Note that transient changes in high frequency amplitude in the SC and cortex occasionally track each other. **D:** Displays the cortical topography of the correlation of power envelopes for the seed SC channel displayed in **A**. Note the stronger power correlation values for  $\mu$ ECoG recording contacts over the occipital cortex.

For all significantly correlated SC recording sites, we computed the average cortical topography of power correlation (Figure 3A). Reflecting the example from Figure 2, the average SC-cortical power correlation topography showed that SC recording sites are mostly correlated to  $\mu$ ECoG contacts over visual cortex. In addition, SC power correlation effects also extend along multisensory suprasylvian areas in the cortex. To determine the laminar distribution of power correlation within the SC, we computed the number of channels at each SC depth that displayed significant power correlation ( $p < 0.05$ ). Recording depth in the SC was determined by flash evoked current source density analysis (Stitt et al., 2013). Despite significant power correlation being detectable across most SC layers, the largest number of cases were found in the region approximately 200 $\mu$ m below the inflection depth, at the presumed border between superficial and deep SC layers (Figure 3B).

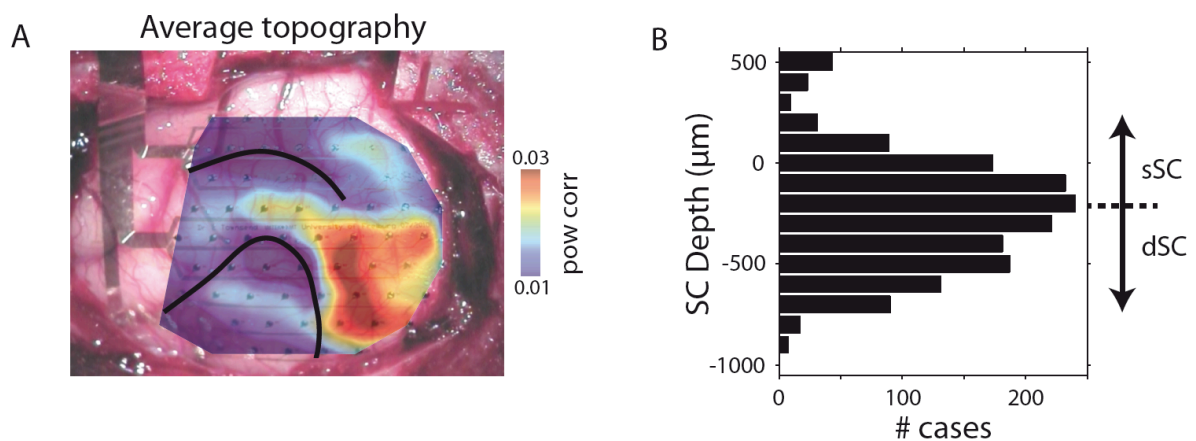


**Figure 3.** Spatial distribution of high frequency power correlations. **A:** The average cortical topography of SC- $\mu$ ECoG power correlation. Note the strongest power correlation values over the visual cortex, and extending across into suprasylvian cortical areas. **B:** The depth of significantly correlated recording sites across all SC penetrations. A depth of 0 $\mu$ m corresponds to the inflection depth. Note the greatest incidence of sites correlated to the cortex in the superficial and intermediate SC layers.

*Spiking activity in the SC is timelocked to the occurrence of high frequency activity in the  $\mu$ ECoG*

We reasoned that correlated fluctuations of high frequency extracellular fields between SC and cortex might to a large extent reflect the correlated spiking activity of neurons

participating in corticotectal networks. To test this hypothesis, we computed the SC spike triggered average (STA) spectra of  $\mu$ ECoG signals. Figure 5 displays an example recording, with STA spectra shown for cortical regions that displayed both strong and weak power

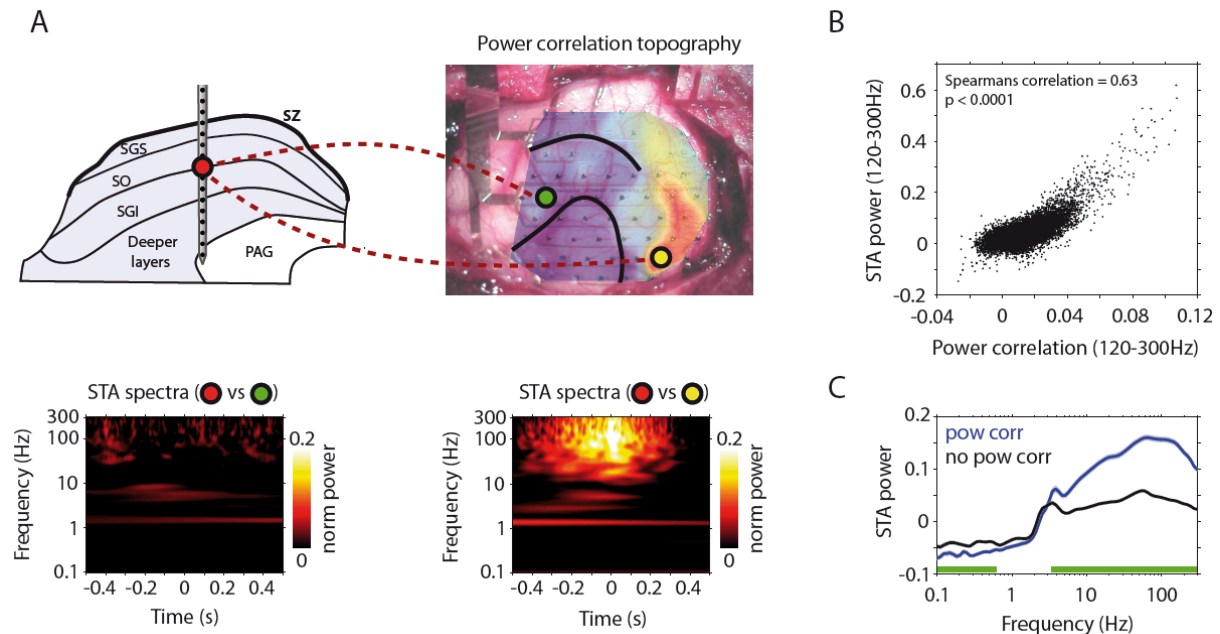


**Figure 4.** High frequency cortical activity is timelocked to SC spiking. **A:** Displays SC spike triggered average cortical spectrograms for two example  $\mu$ ECoG recording sites. Note that the  $\mu$ ECoG recording site displaying stronger power correlation also shows much stronger high frequency activity timelocked to SC spikes. **B:** A scatter plot of the strength of power correlation against STA high frequency power for all SC- $\mu$ ECoG channel pairs. Note the very strong correlation between spike locked power and the magnitude of power correlation. **C:** The average STA power spectrograms for significantly correlated and uncorrelated SC- $\mu$ ECoG channel pairs. The green line indicates where plots are significantly different ( $p < 0.01$ ).

Correlation with the SC seed contact. There was little observable change in signal power locked to the timing of SC spikes in the  $\mu$ ECoG recording contact that displayed weak power correlation. In contrast, the  $\mu$ ECoG recording contact that displayed strong power envelope correlation showed an increase in the power of frequencies above 10Hz around the time of SC spikes. The spike timelocked increase in cortical power was detectable from approximately 300ms before to 300ms after the occurrence of SC spikes (Figure 4A). Across all SC- $\mu$ ECoG channel pairs, the STA high frequency power was highly correlated with the strength of corticotectal power correlation (Figure 4B, Spearman correlation 0.63,  $p < 0.0001$ ), reflecting

the inherent relationship between power correlation and spiking activity. To examine STA cortical power changes for all other frequencies, we computed the population average STA spectra for power correlated and uncorrelated cortical recording sites (Figure 4C). In comparison to uncorrelated recording sites,  $\mu$ ECoG recording sites that displayed significant power correlation with the SC also showed significantly greater STA spectral power in frequencies above  $\sim 3$ Hz ( $p < 0.01$ ).

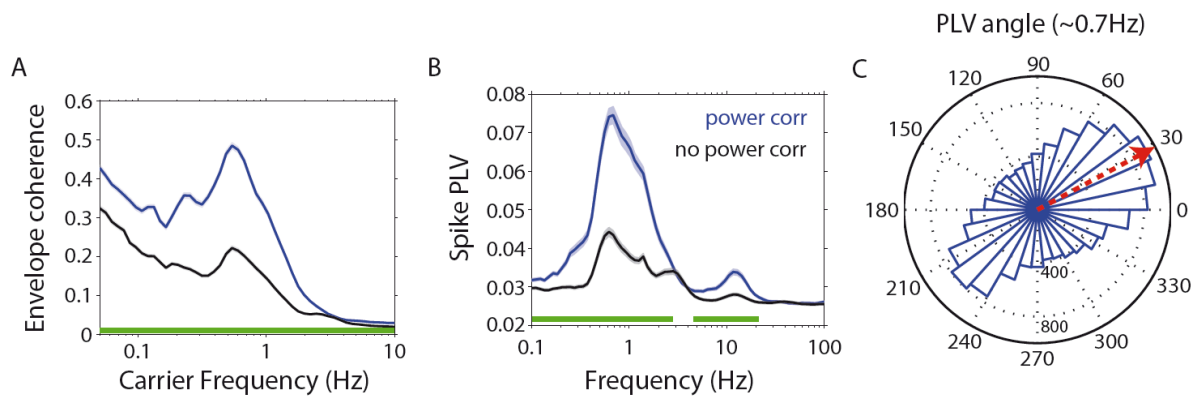


**Figure 5.** High frequency corticotectal power correlation rides on the slow cortical oscillation. **A:** Displays the coherence of high frequency power envelopes computed across carrier frequencies 0.05-10Hz. Power correlated and uncorrelated SC- $\mu$ ECoG channel pairs are plotted in blue and black respectively. Note the peak in carrier frequency coherence at 0.54Hz. **B:** Spike phase locking values calculated using spiking activity from the SC and phase of cortical oscillations. Note the stronger phase locking of SC spikes to slow cortical ( $\sim 0.7$ Hz) and spindle ( $\sim 10$ Hz) oscillations for power correlated recording sites. The green line in plots A and B indicate where power correlated and uncorrelated populations are significantly different ( $p < 0.01$ ). **C:** A circular histogram displaying the preferred phase of firing of all SC recording sites to the cortical slow oscillation (0.7Hz). Note the bimodal distribution separated by  $180^\circ$ . The red dotted line indicates the preferred phase calculated across all SC recording sites.

#### *Correlated corticotectal activity rides on top of the cortical slow oscillation*

To assess the slower temporal structure of correlated corticotectal activity, we computed two further measures: the coherence of power envelopes, and the phase locking value of SC spikes to the phase of cortical fields. The carrier frequency of correlated activity was estimated by computing the coherence of power envelopes for frequencies ranging from 0.05-10Hz. In this

context, coherence analysis of power envelopes reveals the temporal consistency of SC and cortical high frequency amplitude fluctuations. Coherence analysis of carrier frequencies revealed that correlated corticotectal channel pairs were comodulated at low frequencies, with a peak at 0.54Hz (Figure 5A). In contrast, uncorrelated channel pairs displayed significantly weaker carrier frequency coherence over all frequencies measured ( $p < 0.01$ ). For correlated SC and cortical channel pairs, SC spikes were significantly locked to the phase of a slow cortical oscillation at approximately 0.7Hz (Figure 5B). This phase locking was present for many SC recording sites, however SC channels that displayed power correlation with the cortex showed significantly stronger phase locking than uncorrelated channels ( $p < 0.01$ ). Power correlated SC sites also displayed significant phase locking to cortical rhythms at approximately 10Hz, the frequency of spindle oscillations (Möller and Born, 2011). To investigate if SC spiking activity reliably locked to the same phase of the cortical slow oscillation across penetrations and animals, we generated a circular histogram of the preferred cortical phase of SC spikes at 0.7Hz (Figure 5C). The preferred cortical phase of SC spikes displayed a bimodal distribution, with peaks separated by  $180^\circ$ . Rather than locking to different phases of the slow cortical oscillation, this bimodal distribution is most likely an artifact caused by the flip in polarity of cortical fields due to the curvature of the occipital cortex. Across all recording sites, SC spikes fired preferentially at a phase of  $29^\circ$  of the slow cortical oscillation (Figure 5C).

In one experiment, we recorded SC and cortical activity simultaneously with an additional linear silicon probe inserted through the small holes in the  $\mu$ ECoG into the visual cortex. To determine the relationship between intracortical activity and high frequency  $\mu$ ECoG activity, we repeated power correlation and spike phase locking analysis for data that was recorded on the linear probe. Figure 6 displays power correlation topographies computed for seed electrodes originating from the SC and cortex. Similar to SC recordings, high frequency power envelopes from intracortical recording sites were also correlated to  $\mu$ ECoG

sites spanning the visual cortex, with the highest correlation measured in the  $\mu$ ECoG contacts directly adjacent to the intracortical penetration. The cortical topography of SC and

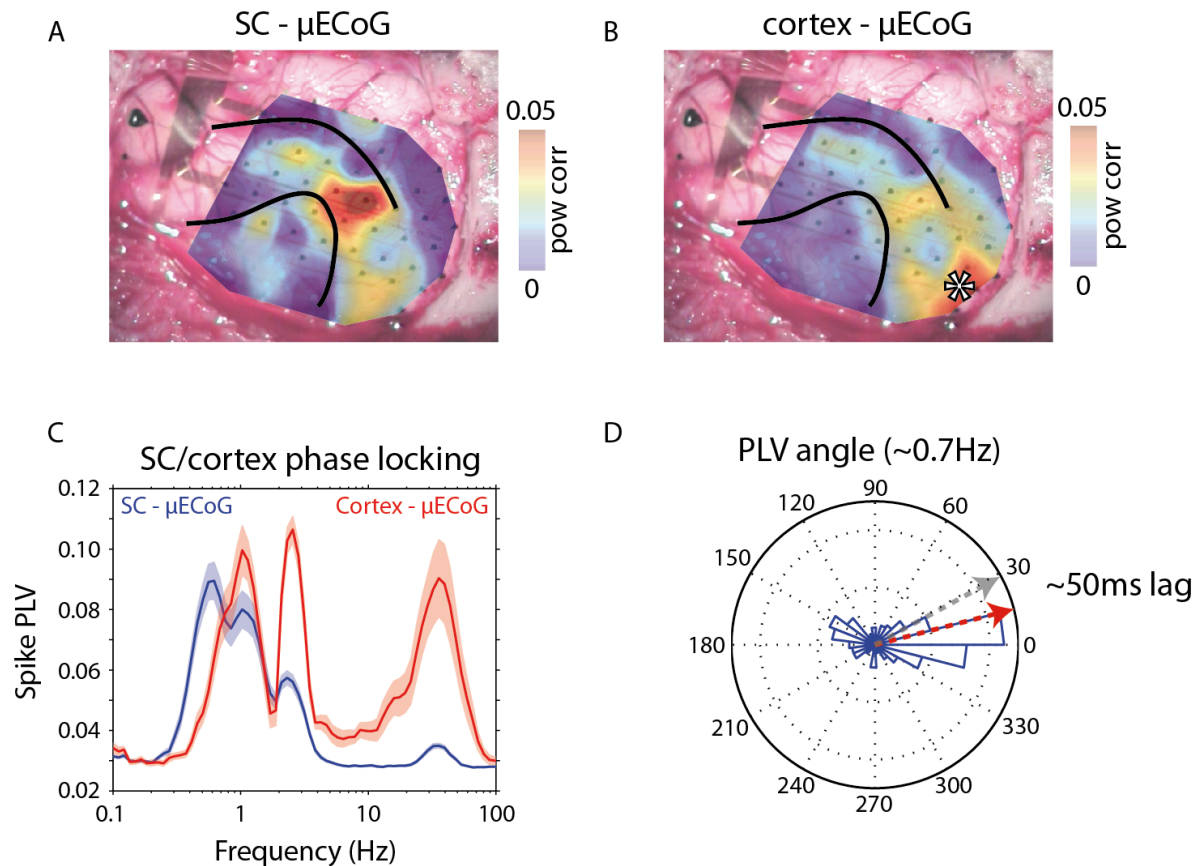


**Figure 6.** Intracortical spiking activity locks to the phase of  $\mu$ ECoG oscillations. Data in this figure is shown for one experiment where  $\mu$ ECoG, SC and intracortical data was collected simultaneously. **A:** The cortical topography of power correlation measured from one seed electrode in the SC. **B:** The cortical topography of power correlation from one seed electrode in the visual cortex. The star denotes the location of the intracortical electrode. **C:** The average SC- $\mu$ ECoG and intracortical- $\mu$ ECoG spike phase locking values  $\pm$  standard error mean. Note that both SC and cortical spikes lock to the slow  $\mu$ ECoG oscillation at approximately 1Hz. In addition, cortical spiking activity is strongly locked to the phase of  $\mu$ ECoG oscillations in the delta (2-3Hz) and gamma (25-60Hz) frequencies. **D:** A circular histogram displaying the preferred phase of intracortical spikes to the 0.7Hz  $\mu$ ECoG oscillations. The preferred phase calculated over all sites is shown as a red dotted line. The preferred phase of SC neurons is shown as a gray dotted line. Note that cortical spikes occur at a slightly earlier phase of the cortical slow oscillation than SC spikes.

intracortical power correlation displayed considerable overlap. Similar to SC spiking activity, cortical spiking activity was strongly locked to the phase of the slow cortical oscillation.

However in addition, cortical spikes displayed strong phase locking to delta (2-4Hz) and gamma (20-60Hz) cortical rhythms. At the slow oscillation frequency, cortical spikes occurred at a phase of  $15^\circ$  (Figure 7C). Taken together, the preferred phase of intracortical and SC spiking activity indicates that slow oscillation modulated spiking activity in the cortex precedes activity in the SC by approximately 50ms.

#### *Ketamine enhances correlated corticotectal activity*

In an attempt to perturb the complex spatiotemporal pattern of correlated corticotectal neural activity, we performed consecutive recordings under ketamine and isoflurane anesthesia in one experiment. We reasoned that since ketamine strongly enhances the slow cortical oscillation (Chauvette et al., 2011), we should observe an associated increase in corticotectal power correlation in comparison to isoflurane. Indeed, the power spectrum of spontaneously recorded  $\mu$ ECoG signals under ketamine was noticeably different from the spectrum under isoflurane, with stronger power detected in the slow oscillatory and gamma frequency bands (Figure 7A). To assess the effect different anesthetics had on corticotectal functional connectivity, we constructed power correlation histograms from all SC- $\mu$ ECoG channel pairs of data recorded under isoflurane and ketamine anesthesia. Accompanying the increase in slow oscillatory power under ketamine was a general shift towards higher power correlation coefficients across all SC- $\mu$ ECoG channel pair combinations (Figure 7B). To ascertain if this increase in corticotectal power correlation was caused by increased cortical entrainment of SC neurons to the slow cortical oscillation, we computed the average spike PLV for channel pairs that displayed significant power correlation under isoflurane and ketamine anesthesia. Indeed, SC spikes occurring under ketamine anesthesia were locked significantly stronger to the phase of the cortical slow oscillation than spikes recorded under isoflurane (ketamine:  $0.17 \pm 0.001$  PLV; isoflurane:  $0.08 \pm 0.001$  PLV;  $p < 0.001$ ).

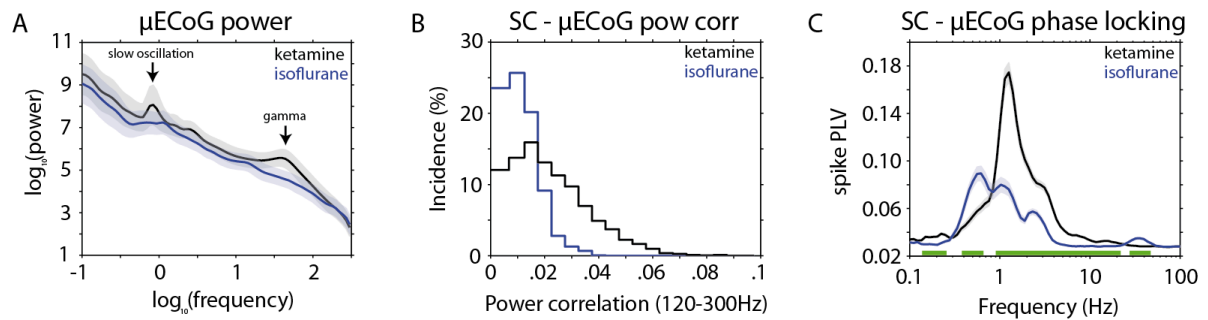


**Figure 8.** Ketamine amplifies corticotectal power correlation by enhancing the cortical slow oscillation. **A:** Displays the average ( $\pm$  standard deviation) power spectra of  $\mu$ ECoG channels under isoflurane (blue) and ketamine (black) anesthesia. Note the increase in slow oscillatory power under ketamine. In addition, ketamine increased the power of gamma oscillations. **B:** The distribution of SC- $\mu$ ECoG power correlation values under isoflurane and ketamine anesthesia. Note that the distribution flattens under ketamine, with more SC- $\mu$ ECoG channel pairs displaying stronger power correlation. **C:** SC spike phase locking to cortical oscillations under isoflurane and ketamine ( $\pm$  SEM). Note that SC spikes under ketamine lock much stronger to the slow oscillation. In addition, the frequency of the phase locking to slower frequencies is more unified under ketamine. The green line in indicates where isoflurane and ketamine PLV values are significantly different ( $p < 0.01$ ).

## Discussion

To summarize, this study reveals for the first time the complex spatiotemporal organization of spontaneously generated corticotectal activity. Functional connectivity was characterized by transient bursts of high frequency extracellular activity occurring simultaneously in both the SC and cortex. High frequency activity in the cortex was timelocked to the occurrence of spiking activity in the SC, with the strength of corticotectal power correlation strongly correlated with the magnitude of SC spike triggered average high frequency power in the cortex. High frequency corticotectal interaction was strongly timelocked to the phase of the cortical slow oscillation, with cortical neurons firing at a slightly earlier phase than SC neurons. In addition, SC spikes were also locked to the phase of cortical spindle oscillations. Finally, Ketamine anesthesia artificially enhances correlated corticotectal activity by strengthening the slow cortical oscillation.

### *The spatiotemporal dynamics of spontaneous high frequency activity reveal functional corticotectal connectivity*

Although the precise nature of intrinsically generated activity in the brain remains unclear, it has been hypothesized that the combination of the biophysical properties of neurons and anatomical connectivity produce correlated fluctuations in the activity of functional neural networks (Engel et al., 2013). Supporting the link between anatomical and functional connectivity, we found that the spatial topography of corticotectal functional connectivity is in strong agreement with previously identified corticotectal anatomical connectivity (Manger et al., 2010). Reflecting the cortical topography of SC power correlation, the SC receives input from widely distributed cortical areas, with visual areas 18 and 21 and medial suprasylvian areas providing the densest cortical input in the ferret (Harting et al., 1992). Similarly, cortical inputs to the SC originating outside of primary visual cortex terminate in both superficial and deep SC layers (Harting et al., 1992), matching the laminar distribution

of cortically correlated SC recording sites described here. To our knowledge, this study represents the first attempt at investigating the large-scale spatiotemporal structure of spontaneous corticotectal interaction, therefore to place our results into context we must look to previous studies investigating different brain areas. Our results are most similar to a study performed by Fukushima and colleagues (2012), which showed that high frequency  $\mu$ ECoG signals in awake monkey auditory cortex display spatial covariations in a manner that is reflective of the underlying tonotopic map of the auditory cortex. Revealing a similar functional organization of the primary visual cortex of the cat, Kenet and coworkers (2003) showed using voltage imaging that the spatiotemporal structure of neural activity was highly correlated to the underlying orientation map. Aside from reflecting the functional organization or brain regions, large-scale spatiotemporal fluctuations of spontaneous neural activity have also been shown to explain a large degree of trial-to-trial variability of sensory evoked responses in primary visual cortex (Arieli et al., 1996).

In another study, Nir and coworkers (2008) found strong correlation of firing rates of neurons and high frequency (40-100Hz) power modulations between interhemispheric recording sites in the human auditory cortex. In contrast to our results, whereby correlated corticotectal power modulations fluctuated at approximately 0.7Hz, interhemispheric power modulations in awake humans fluctuated at much lower frequencies below 0.1Hz (Nir et al., 2008). Indeed, this discrepancy is most likely due to the effects of anesthesia, which greatly enhances the cortical slow oscillation (Lewis et al., 2012). Other groups have investigated the corollary structure of intrinsically generated brain activity using functional magnetic resonance imaging (fMRI), which tracks the slow modulations of blood oxygen level dependent (BOLD) signals throughout the brain (Hutchison et al., 2013). Vincent and coworkers (2007) showed that spontaneous BOLD fluctuations in the anesthetized monkey brain are correlated between anatomically connected visual cortical regions. Since BOLD signals track slower hemodynamic responses of brain regions, this study reveals functional brain organization can be delineated at both very slow and very fast temporal scales. Indeed,

Schölvinck and colleagues (2010) showed that high frequency extracellular activity (40-80Hz) is highly correlated with the BOLD signal, with the hemodynamic response lagging LFPs by 6 to 8 seconds. Collectively, correlated neural activity measured electrophysiologically or through fMRI can be more generally described as envelope intrinsic coupling modes (Engel et al., 2013). Although demonstrated in corticotectal networks, we propose that the spontaneous correlation of high frequency power envelopes will become a useful tool for elucidating functional connectivity more generally in the brain.

#### *SC activity couples to cortical slow and spindle oscillations*

As we have shown here, the cortical slow oscillation governs correlated corticotectal activity under anesthesia. The slow oscillation is generated locally within the cortex and is characterized by periods of quiescence (“down” states), where neurons are hyperpolarized and presynaptic inputs are silent, and synchronous bursts of activity (“up” states) during which neurons are depolarized (Steriade et al., 1993a, 1993b; Sanchez-Vives and McCormick, 2000). In a human ECoG study, Lewis et al (2012) showed that the emergence of the slow cortical oscillation during the induction of propofol anesthesia was the strongest physiological correlate of the loss of consciousness. Apart from being present under anesthesia, the slow cortical oscillation characterizes the state of the brain during deep sleep, where it is proposed to facilitate the transfer of short-term memories stored in the hippocampus to long term memories encoded in neocortical networks (Möller and Born, 2011). The hypothesized mechanism by which memories are transferred from hippocampus to cortex is through the interplay of three separate brain oscillations: the cortically generated slow oscillation (~0.7Hz), hippocampal ripples (140-220Hz), and thalamic spindles (10-15Hz). Under this regimen, high frequency activity (‘ripples’) is transferred from the hippocampus to the cortex during the trough of thalamocortical spindles, and also during the down-to-up phase of slow cortical oscillations (Sirota et al., 2003; Isomura et al., 2006; Möller and Born, 2011). We observed a remarkably similar relationship for correlated corticotectal activity, where SC

spikes were significantly locked to the phase of cortical slow and spindle oscillations. Although the functional significance of such temporally ordered corticotectal activity remains unclear, the most likely scenarios are that either; 1) temporal fluctuations in cortical activity caused by the interaction of different oscillators across the thalamic-cortical-hippocampal axis are fed forward to downstream target neurons in the SC; 2) or that the SC potentially serves a role in the regulation of activity during slow wave sleep.

Since projection neurons in cortical layer 5 are strongly activated during up states of the slow oscillation (Cowan and Wilson, 1994; Contreras and Steriade, 1995; Sanchez-Vives and McCormick, 2000), it is perhaps unsurprising the downstream target neurons of these cells fire preferentially during cortical up states. Indeed, the fact that SC neurons are locked to a slightly later phase of the slow cortical oscillation than cortical neurons is evidence that the cortex is imposing temporally organized activity on SC neurons. Previous studies have also shown that neural activity in the basal ganglia (Magill et al., 2000), thalamus (Timofeev and Steriade, 1996), cerebellum (Ros et al., 2009), and brainstem (Mena-Segovia et al., 2008) are locked to the phase of the slow cortical oscillation during slow wave sleep and anesthesia. These results highlight the strong entrainment capacity of the up state during the slow cortical oscillation, and support the hypothesis that correlated corticotectal activity observed here is the result of the propagation of cortical up states to the SC.

Alternatively, the temporal coordination of corticotectal activity under anesthesia may represent more than the subcortical projection of cortical up states. Indeed, SC spikes additionally lock to the phase of cortical spindle oscillations, which together with slow oscillations characterize the temporal dynamics of cortical activity during non-rapid eye movement (REM) sleep (Möller and Born, 2011). Taken together, these data suggest that the SC may somehow be involved in the regulation of sleep. Miller and colleagues (1998) provided direct evidence supporting this hypothesis by showing that the surgical ablation of the SC and pretectum eliminates acute responses to light during sleep. Under normal circumstances, the transition from light-to-dark in nocturnal animals induces a shift from slow

wave sleep towards the more wake-like rapid eye movement sleep (REM) (Borbely, 1976), however after ablation of the SC this light induced shift in brain state is absent (Miller et al., 1998). A subsequent study by Lupi and colleagues (2008) showed that such acute effects of light on sleep are regulated by a genetically distinct subpopulation of intrinsically photosensitive retinal ganglion cells (pRGC) that send dense projections to the contralateral SC (Hattar et al., 2006). In diurnal animals, the hypothesized function of pRGCs is the opposite to nocturnal animals, where the acute presence of light (such as dusk) would bias the state of the brain away from slow wave sleep towards REM sleep, allowing animals to naturally wake and be alert during the most evolutionarily relevant time of day (Miller et al., 1998). However, further studies in naturally sleeping animals will be required to elucidate the precise function of slow oscillation and spindle coupled corticotectal activity.

## References

- Arieli a, Sterkin a, Grinvald a, Aertsen a (1996) Dynamics of ongoing activity: explanation of the large variability in evoked cortical responses. *Science* 273:1868–1871.
- Berson D (1988a) Retinal and cortical inputs to cat superior colliculus: convergence and laminar specificity. *Prog Brain Res* 75:17–26.
- Berson DM (1988b) Convergence of retinal W-cell and corticotectal input to cells of the cat superior colliculus. *J Neurophysiol* 60:1861–1873.
- Borbely A (1976) Sleep and motor activity of the rat during ultra-short light-dark cycles. *Brain Res* 114:305–317.
- Buzsáki G, Anastassiou C a, Koch C (2012) The origin of extracellular fields and currents-- EEG, ECoG, LFP and spikes. *Nat Rev Neurosci* 13:407–420.
- Chauvette S, Crochet S, Volgushev M, Timofeev I (2011) Properties of Slow Oscillation during Slow-Wave Sleep and Anesthesia in Cats. *J Neurosci* 31:14998–15008.
- Contreras D, Steriade M (1995) Cellular basis of EEG slow rhythms: a study of dynamic corticothalamic relationships. *J Neurosci* 15:604–622.
- Cowan RL, Wilson CJ (1994) Spontaneous firing patterns and axonal projections of single corticostriatal neurons in the rat medial agranular cortex. *J Neurophysiol* 71:17–32.
- Edwards SB, Ginsburgh CL, Henkel CK, Stein BE (1979) Sources of subcortical projections to the superior colliculus in the cat. *J Comp Neurol* 184:309–329.
- Engel AK, Gerloff C, Hilgetag CC, Nolte G (2013) Intrinsic coupling modes: multiscale interactions in ongoing brain activity. *Neuron* 80:867–886.
- Fukushima M, Saunders RC, Leopold D a, Mishkin M, Averbach BB (2012) Spontaneous high-gamma band activity reflects functional organization of auditory cortex in the awake macaque. *Neuron* 74:899–910.
- Harting JK, Updyke B V, Lieshout DPVAN (1992) Corticotectal projections in the cat: Anterograde transport studies of twenty-five cortical areas. *J Comp Neurol* 379:14:14998–15008.
- Hattar S, Kumar M, Park A, Tong P, Tung J, Yau K-W, Berson DM (2006) Central projections of melanopsin-expressing retinal ganglion cells in the mouse. *J Comp Neurol* 349:326–349.
- Hutchison RM, Womelsdorf T, Allen E a, Bandettini P a, Calhoun VD, Corbetta M, Della Penna S, Duyn JH, Glover GH, Gonzalez-Castillo J, Handwerker D a, Keilholz S, Kiviniemi V, Leopold D a, de Pasquale F, Sporns O, Walter M, Chang C (2013) Dynamic functional connectivity: promise, issues, and interpretations. *Neuroimage* 80:360–378.

- Isomura Y, Sirota A, Ozen S, Montgomery S, Mizuseki K, Henze D a, Buzsáki G (2006) Integration and segregation of activity in entorhinal-hippocampal subregions by neocortical slow oscillations. *Neuron* 52:871–882.
- Ji D, Wilson M a (2007) Coordinated memory replay in the visual cortex and hippocampus during sleep. *Nat Neurosci* 10:100–107.
- Jiang ZD, Moore DR, King a J (1997) Sources of subcortical projections to the superior colliculus in the ferret. *Brain Res* 755:279–292.
- Kenet T, Bibitchkov D, Tsodyks M, Grinvald A, Arieli A (2003) Spontaneously emerging cortical representations of visual attributes. *Nature* 425:954–956.
- King a J, Jiang ZD, Moore DR (1998) Auditory brainstem projections to the ferret superior colliculus: anatomical contribution to the neural coding of sound azimuth. *J Comp Neurol* 390:342–365.
- Lachaux JP, Rodriguez E, Martinerie J, Varela FJ (1999) Measuring phase synchrony in brain signals. *Hum Brain Mapp* 8:194–208.
- Lewis L, Weiner V, Mukamel E, Donoghue J, Eskandar E, Madsen J, Anderson W, Hochberg L, Cash S, Brown E, Purdon P (2012) Rapid fragmentation of neuronal networks at the onset of propofol-induced unconsciousness. *PNAS* 109(49):3377–3386.
- Lupi D, Oster H, Thompson S, Foster RG (2008) The acute light-induction of sleep is mediated by OPN4-based photoreception. *Nat Neurosci* 11:1068–1073.
- Magill PJ, Bolam JP, Bevan MD (2000) Relationship of activity in the subthalamic nucleus-globus pallidus network to cortical electroencephalogram. *J Neurosci* 20:820–833.
- Manger PR, Restrepo CE, Innocenti GM (2010) The superior colliculus of the ferret: cortical afferents and efferent connections to dorsal thalamus. *Brain Res* 1353:74–85.
- Mena-Segovia J, Sims HM, Magill PJ, Bolam JP (2008) Cholinergic brainstem neurons modulate cortical gamma activity during slow oscillations. *J Physiol* 586:2947–2960.
- Miller a M, Obermeyer WH, Behan M, Benca RM (1998) The superior colliculus-pretectum mediates the direct effects of light on sleep. *PNAS* 95:8957–8962.
- Miller K, Sorensen L, Ojemann JG, den Nijs M (2009) Power-Law Scaling in the Brain Surface Electric Potential Sporns O, ed. *PLoS Comput Biol* 5:e1000609.
- Minlebaev M, Colonnese M, Tsintsadze T, Sirota A, Khazipov R (2011) Early  $\gamma$  oscillations synchronize developing thalamus and cortex. *Science* 334:226–229.
- Mohajerani MH, Chan AW, Mohsenvand M, LeDue J, Liu R, McVea D a, Boyd JD, Wang YT, Reimers M, Murphy TH (2013) Spontaneous cortical activity alternates between motifs defined by regional axonal projections. *Nat Neurosci* 16:1426–1435.
- Mölle M, Born J (2011) Slow oscillations orchestrating fast oscillations and memory consolidation. *Prog Brain Res* 193:93–110.

- Nir Y, Mukamel R, Dinstein I, Privman E, Harel M, Fisch L, Gelbard-Sagiv H, Kipervasser S, Andelman F, Neufeld MY, Kramer U, Arieli A, Fried I, Malach R (2008) Interhemispheric correlations of slow spontaneous neuronal fluctuations revealed in human sensory cortex. *Nat Neurosci* 11:1100–1108.
- Ros H, Sachdev RNS, Yu Y, Sestan N, McCormick D a (2009) Neocortical networks entrain neuronal circuits in cerebellar cortex. *J Neurosci* 29:10309–10320.
- Sanchez-Vives M V, McCormick D a (2000) Cellular and network mechanisms of rhythmic recurrent activity in neocortex. *Nat Neurosci* 3:1027–1034.
- Schölvinck ML, Maier A, Ye FQ, Duyn JH, Leopold D a (2010) Neural basis of global resting-state fMRI activity. *PNAS* 107:10238–10243.
- Sirota A, Csicsvari J, Buhl D, Buzsáki G (2003) Communication between neocortex and hippocampus during sleep in rodents. *PNAS* 100:2065–2069.
- Steriade M, Nuñez A, Amzica F (1993a) A novel slow (< 1 Hz) oscillation depolarizing and hyperpolarizing of neocortical neurons in vivo: depolarizing and hyperpolarizing components. *J Neurosci* 13:3252–3265.
- Steriade M, Nuñez A, Amzica F (1993b) Intracellular Analysis Neocortical Oscillation Electroencephalogram of Relations between the Slow (< 1 and Other Sleep Rhythms of the Hz). *J Neurosci* 13:3266–3283.
- Stitt I, Galindo-Leon E, Pieper F, Engler G, Engel AK (2013) Laminar profile of visual response properties in ferret superior colliculus. *J Neurophysiol* 110:1333–1345.
- Timofeev I, Steriade M (1996) Low-frequency rhythms in the thalamus of intact-cortex and decorticated cats. *J Neurophysiol* 76:4152–4168.
- Tsodyks M, Kenet T, Grinvald, A. Arieli A (1999) Linking Spontaneous Activity of Single Cortical Neurons and the Underlying Functional Architecture. *Science* (80- ) 286:1943–1946.
- Vincent JL, Patel GH, Fox MD, Snyder a Z, Baker JT, Van Essen DC, Zempel JM, Snyder LH, Corbetta M, Raichle ME (2007) Intrinsic functional architecture in the anaesthetized monkey brain. *Nature* 447:83–86.

# Chapter 5

---

## Discussion

Here, we report for the first time the analysis of SC neural dynamics at intrinsic, local, and global scales. Within the SC, visual response properties varied systematically across different layers. The depth dependence of visually evoked activity was best characterized by the presence of temporally precise gamma oscillations specifically in retinorecipient superficial SC layers. Locally within the midbrain, visual stimuli also evoked responses in the neighboring IC, with responses characterized by phase locking of the LFP to the stimulus in the 6-10Hz and 15-30Hz frequency bands. Imaginary coherence analysis of simultaneously recorded SC and IC LFPs suggests that the SC drives visually evoked activity in IC. Finally, the state of visual and suprasylvian cortical networks dominate the temporal structure of spontaneous SC activity under anesthesia. SC spiking activity was typically characterized by brief bursts of activity locked to the phase of cortical slow ( $\sim 0.7\text{Hz}$ ) and spindle ( $\sim 10\text{Hz}$ ) oscillations, suggesting that cortical “up” states are propagated to the SC.

*The analysis of neural dynamics reveals functional properties of SC networks*

As discussed in each chapter, the dynamics of neural activity at both local and global levels of organization strongly reflect the known structural connectivity patterns of the

SC. Intrinsically in the SC, this was reflected most strongly by the laminar profile of CSD analysis and entrained gamma oscillations. The precise entrainment of oscillatory activity in retinorecipient layers reveals that the degree with which the SC can follow the temporal dynamics of bottom up sensory inputs. Locally within the midbrain, the physiological correlates of reciprocal connectivity with the neighboring IC are far less obvious. The consequences of inputs in both directions (ie: SC-to-IC, or IC-to-SC) are dramatically asymmetric, where auditory inputs to the deep SC drive spiking activity, and visual inputs to the IC provide merely subthreshold modulatory effects. However, this apparent asymmetry in audiovisual interaction is certainly consistent with the hypothesis that visual inputs inform spatial plasticity in the IC, ensuring the alignment of auditory and visual representations of space within the midbrain. In addition to following the dynamics of bottom-up inputs following sensory stimuli, the temporal structure of spontaneously generated activity in the SC is greatly dependent on the state of cortical areas that project to the SC. Indeed, corticotectal connectivity in the anesthetized ferret is reflected physiologically by the locking of SC activity to the phase of prominent cortical sleep oscillations. Apart from reflecting the propagation of cortical up states to the SC, this data could provide the first evidence suggesting that the SC plays a role in the regulation of slow wave sleep that was previously unknown. By uncovering such an unexpected relationship between SC and cortical activity, this finding highlights the importance of elucidating the physiological consequences of structural connectivity in the brain. Collectively, my results emphasize the role that the convergence of both bottom up sensory, and top down cortical inputs have on shaping neural activity in the SC. Although the analysis of both sensory evoked and spontaneous neural dynamics is very informative about functional neural networks in the SC, we can unfortunately not draw any meaningful conclusions on the role dynamics play in the sensorimotor

transformational capabilities of the SC. The reason for this is that we always recorded neural activity in the anesthetized and paralyzed ferret, where motor outputs are silent.

### *Concluding remarks*

The SC, due to its well described anatomy and function, is emerging as a promising alternative structure for the investigation of one of the fundamental goals of neuroscience – namely to understand the link between brain structure and function. Indeed, outside of the thalamus, hippocampus, and cortex, there is large gap in our understanding of the nature of dynamic neural networks in the rest of the brain. Until now, it remains far from clear if the fundamental principles of neural dynamics first discovered in these model brain networks are universally applicable to other brain areas that display vastly different structural makeup. The studies presented in this thesis indeed provide evidence that similar mechanisms are in play, however further studies will be required to address this question in more detail.

### *Future direction*

One of the largest caveats of the studies described here is that they were all performed in anesthetized and paralyzed animals. The primary role of the SC is the transformation of sensory input signals into output motor commands. Therefore, to gain a fuller understanding of the role neural dynamics plays in the sensorimotor function of the SC, we must perform similar recordings from awake and behaving animals. Below, I will describe three future experiments that will further elucidate the underlying role neural dynamics plays in SC function.

- 1) We were unable to distinguish between intrinsically generated or extrinsically entrained gamma oscillations following flash and grating visual stimuli in the SC.

Therefore, to uncover the source of such oscillations it would be ideal to record neural activity from both bottom up retinal inputs and top down cortical inputs simultaneously with SC activity. The cross correlation analysis of the spiking activity of retinal or cortical cells with superficial SC neurons will determine if these inputs entrain SC oscillations. These experiments would ideally be performed under isoflurane anesthesia to remain consistent with the results presented here. Apart from uncovering the source of gamma oscillations in the SC, it is also important to determine if such temporally structured activity is merely an artifact of anesthesia, or if it is indeed useful for SC function. Therefore, flash and grating evoked SC activity must also be recorded from awake animals.

2) Since it is virtually impossible to perform functional connectivity analysis on neural responses that display a large degree of phase locking to the stimulus, we were unable to definitively confirm if the superficial SC was indeed the source of visual evoked activity in the neighboring IC. To overcome this technical constraint, I propose to inject a viral vector containing the light activated excitatory ion channel - channelrhodopsin-2 - into the SC. After an incubation period, an optical fiber could be delivered to the SC where short light pulses could activate SC neurons while simultaneously recording from the IC. This approach would provide definitive evidence that the SC is driving IC visual activity through previously identified anatomical pathways.

3) We identified prominent patterns of slow wave sleep activity in the SC in isoflurane and ketamine anesthetized ferrets. However, it remains unclear if these patterns of activity are simply an artifact of anesthesia or if SC neurons are similarly entrained during natural slow wave sleep. Therefore, I propose to record SC spiking, and

cortical  $\mu$ ECoG activity simultaneously in chronically implanted ferrets. Not only would this approach enable to identification of slow wave sleep activity during natural sleep, but also the characterization of corticotectal dynamics in awake and behaving animals.